A HIGH RESOLUTION STUDY OF ISOBARIC ANALOGUE STATES IN ^{41}K AND ^{23}Na

by

George Albert Keyworth II

Department of Physics
Duke University

A dissertation submitted in partial fulfillment of the requirements for the degree of Doctor of Philosophy in the Department of Physics in the Graduate School of Arts and Sciences of Duke University

1968

A HIGH RESOLUTION STUDY OF ISOBARIC ANALOGUE STATES IN ^{41}K AND ^{23}Na

by

George Albert Keyworth II

Department of Physics
Duke University

Date: April 8, 1968

Approved:

E. G. Bilpuch, Supervisor

A dissertation submitted in partial fulfillment of the requirements for the degree of Doctor of Philosophy in the Department of Physics in the Graduate School of Arts and Sciences of Duke University

1968

ABSTRACT

(Physics)

A HIGH RESOLUTION STUDY OF ISOBARIC ANALOGUE STATES IN ^{41}K AND ^{23}Na

by

George Albert Keyworth II

Department of Physics
Duke University

Date: _____

Approved:

_____
E. G. Bilpuch, Supervisor

_____

_____

_____

_____

An abstract of a dissertation submitted in partial fulfillment of the requirements for the degree of Doctor of Philosophy in the Department of Physics in the Graduate School of Arts and Sciences of Duke University

1968

A HIGH RESOLUTION STUDY OF ISOBARIC ANALOGUE STATES IN ^{41}K AND ^{23}Na

by

George Albert Keyworth, II

Cross sections for the elastic scattering of protons by ^{40}A from 1.63 to 2.60 MeV and by ^{22}Ne from 0.80 to 3.13 MeV have been measured. In addition, reaction cross sections have been measured wherever obtainable. The ^{40}A data were taken at 135° whereas the ^{22}Ne data were measured at 90, 105, 120, 135, 150 and 160°. Utilizing a cryogenic target chamber developed for these experiments, permitting detection of charged reaction products, an energy resolution of about 250 eV was realized.

Two isobaric analogue states were seen in each of the compound systems, ^{41}K and ^{23}Na. In all cases, the analogue states were in evidence as a fragmentation of the broad $T_>$ analogue state into an enhancement of the background $T_<$ states. These individual fine-structure states have been analyzed within the framework of R-matrix theory, and spins, parities, partial and total widths have been determined. A total of approximately 200 resonances have been observed and analyzed in this manner.

Spectroscopic factors obtained from these measurements for the analogue states agree quite well with those previously measured for the parent states from (d,p) stripping on the same target nuclei. In addition, these definite spin and parity assignments resolve previous ambiquities regarding the J^{π} assignments to the parent states.

ACKNOWLEDGMENTS

I would like to express sincere gratitude to the members of the Duke University Instrument Shop, and in particular to Mr. A. W. Lovette, whose skill and experienced advice made the extensive developmental work involved in this endeavor fruitful. I would like to thank Dr. G. C. Kyker, Jr., whose collaboration throughout these experiments was essential to their success and to Mr. D. L. Sellin, who assisted in taking and analyzing much of the data and who wrote a computer program which was of significant value in the analysis. The contributions in taking and analyzing the data of Messrs. J. C. Browne and J. D. Moses are also appreciated. To Dr. P. Wilhjelm, for his encouragement, patience and overall assistance in the ^{22}Ne experiment, I am sincerely grateful.

Many hours have been contributed by Mrs. Joseph Bailey, Mrs. W. F. E. Pineo and Mrs. D. Ramm in preparation of the data and by Mr. Sidney Edwards and Mr. R. L. Rummel in maintaining the equipment used in these experiments.

To my advisor, Dr. E. G. Bilpuch, I would like to express heartfelt thanks for his continual support and untold hours of guidance. To

Dr. H. W. Newson, for his confidence and support, I owe a great debt.

Valuable discussions with Drs. L. C. Biedenharn and M. Danos have been a significant contribution.

I would like to express profound appreciation to Dr. H. L. Schultz of Yale University, without whose patience and encouragement I would not have pursued this profession. To my parents, who have encouraged and assisted me throughout my studies, I express belated thanks.

Finally, I owe my greatest debt to my wife, Polly, whose continual patience and encouragement has been sorely tried during my graduate studies.

This work was supported in part by the U. S. Atomic Energy Commission, and computations involved in this research were performed in the Duke University Digital Computing Laboratory and in the Triangle Universities Computing Center which are supported in part by the National Science Foundation.

G.A.K., II

CONTENTS

APPENDIX

LIST OF FIGURES

LIST OF TABLES

A HIGH RESOLUTION STUDY OF ISOBARIC ANALOGUE STATES IN ^{41}K AND ^{23}Na

Chapter I

INTRODUCTION

Isobaric analogue states may be generally defined as any two neighboring pairs of an isobaric multiplet. The addition of a proton to a nucleus, C, can lead to the formation of states (p + C) which are the analogue states of the low lying states of the system (n + C). These states are members of the same isobaric spin multiplet since they have the same total isobaric spin, T of the (n + C) system, but differ in the T_z component. The analogue state with $T \neq T_z$ is designated a $T_>$ state whereas the "normal" $T - 1 = T_z$ states are called the $T_<$ states. A characteristic feature of the isobaric analogue state in the "daughter" (p + C) nucleus is that it differs from the "parent" (n + C) state by essentially the Coulomb energy of the additional proton.

The occurence of isobaric analogue states was demonstrated by Anderson and Wong[1] in 1961, using the charge-exchange (p, n) reaction. Since that time, analogue states have been in evidence in such diverse reactions as elastic and inelastic scattering, pickup and stripping reactions, and proton capture. The study of isobaric analogue states as resonances in

the compound nucleus has been of particular interest. In 1964, an experiment at Florida State University[2] showed that an analogue state formed in ^{93}Tc by the elastic scattering of protons from ^{92}Mo was not a single broad resonance as previously thought, but was composed of many narrow anomalies. Although their proton beam energy resolution was not adequate to resolve the fine structure, the effect was evident. Reactions which result in formation of compound nuclear resonances are particularly suitable for studying fine structure because the resolution is determined only by the spread in the incident beam energy, the target thickness and its Doppler broadening, and is essentially independent of detector resolution. At this time, the energy spread in electrostatic accelerators is appreciably lower than the resolution available in a particle detector.

Since high resolution techniques had already been developed at Duke University for producing nearly monoenergetic neutrons from (p,n) reactions, it was decided to apply these techniques to the study of fine structure in isobaric analogue states. Accordingly, a windowless cryogenic target chamber for producing thin gas targets, and which would permit detection of charged reaction products, was developed.

The large majority of experiments performed in the study of analogue states have involved heavy nuclei, due partly to the large neutron excess in these nuclei. Lane[3] has suggested that this neutron excess will tend to "dilute" the Coulomb field, thereby implying purity of isobaric spin. However, since the energy required to excite the isobaric analogue

resonances increases with mass, the availability of only a 3 MeV accelerator imposed some restrictions. Energy limitations also restrict measurements to states of low ℓ-value, due to penetration effects. It was first decided to investigate the elastic scattering of protons by ^{40}A. This nucleus had previously been investigated by Parks et al.,[4] through the (p,n) reaction, and was found to have many closely spaced levels which were resolvable with existing equipment. This target nucleus had several other advantages: it is essentially monoisotopic in its natural form (99.6% ^{40}A), has desirable thermodynamic properties, is one of the heaviest elements suitable with a 3 MeV accelerator, and has a fairly high (p,n) threshold.

In this experiment, cross sections for ^{40}A(p,p)^{40}A and ^{40}A(p,α)^{37}Cl have been measured from 1.63 to 2.60 MeV at a lab angle of 135° and with an energy resolution of about 250 eV. In addition, the ^{40}A(p,n)^{40}K cross section has been measured from threshold (2.344 MeV) to 2.60 MeV. Isobaric analogues of low lying states of ^{41}A have been observed primarily as an enhancement of the normal ($T = T_z$) states in the compound nucleus.

Upon completion of the ^{40}A experiment, it was decided to study the region of analogue states in another nucleus, which was lighter and whose compound nuclear states could also decay through the inelastic proton channel. For this purpose, a target of ^{22}Ne was selected. Because the natural abundance of this gaseous isotope is only 8.8%, a sample enriched to 99% ^{22}Ne was obtained and a gas handling system capable of

regulating and recovering a relatively small volume of this gas was developed. The choice of this target nucleus was dictated by four major properties: (1) it is a stable gas whose thermodynamic properties make it particularly suitable for use in the cryogenic target chamber, (2) the excitation energy in the compound nucleus, ^{23}Na, is particularly high for light nuclei (proton separation energy of 8.79 MeV, thus increasing the likelihood of a high density of T states, (3) it has an exceptionally high inelastic proton cross section, above E_p = 2 MeV, with all other decay channels essentially closed in the region of interest and (4) it has an isobaric spin projection of $T_z = 3/2$ for the parent nucleus, which is relatively high for a light nucleus. Of these four desirable properties, perhaps the most significant is that only proton decay channels are open. When other decay modes are available, particularly the (p,n) channel, the widths become larger. Preliminary calculations indicated that several analogue states were to be expected in the proton energy range of 1 to 3 MeV.

In the ^{22}Ne experiment, the elastic proton scattering cross section was measured from 0.8 to 3.13 MeV. In addition, the proton inelastic scattering cross section to the first excited state of ^{22}Ne was measured from 1.8 to 3.13 MeV. Using a cryogenic target chamber developed for this experiment, reaction products were observed at 90, 105, 120, 135, 150 and 160° with an energy resolution of from 110 to 300 eV. As in the ^{40}A experiment, the analogue states are seen primarily as an enhancement of the T states in the compound system. However, the

situation here is more complex since the background $T_<$ states are much more pronounced because of the lower Coulomb barrier.

The significance of such detailed studies of fine structure of isobaric analogue states lies primarily in the information learned regarding the "goodness" of isobaric spin as a quantum number and in aiding the understanding of the nature of intermediate structure. Such experiments offer a severe test, both quantitative and qualitative, to current theories of nuclear structure.

Chapter II

THEORY

Two somewhat overlapping facets of nuclear reaction theory are involved in the work described in this dissertation; one, the well established R-matrix theory of nuclear reactions and the other, the less well resolved theory of isobaric analogue states. The former is commonly used to extract information concerning the formation and decay of compound nuclear states; that is, their spins, parities and partial and total widths. This information is then examined within the framework of current theories of analogue states. In this chapter, a brief synopsis of the relevant resonance theory is given as well as a discussion of the theory of analogue states.

A. Resonance Theory

Modern theories of nuclear reactions begin perhaps with the introduction by Bohr and others[5] of the concept of the compound nucleus. In this picture, the bombarding particle loses its independent identity and

the total energy of the system is shared by all the nucleons present. The dissociation of the compound nucleus can take place in many ways, called exit channels. It is the large number of these reaction alternatives that contributes to the formidability of the various reaction theories relying on the compound nucleus picture.

The essential feature of R-matrix theory, initially introduced by Wigner et al.,[6] is the existence of a complete set of states of all particles defined in a volume of nuclear size. These formal states can then be identified with states of the compound nucleus and the cross sections involved expressed in terms of these states. The relations connecting the cross section and these states are, however, very complicated. Wigner et al.[6] found it convenient to express the cross section in terms of the collision matrix and this, in turn, in terms of the R, L, and Ω -matrices. The R-matrix includes the internal interactions and depends upon the energy, the interaction radii, a_c, and a set of boundary condition parameters B_c. The L and Ω matrices describe the external interaction and depend on E and a_c. None of these quantities are themselves independent of the size of the internal region, although their combination to form the collision matrix is.

Two fundamental assumptions are at the basis of R-matrix theory. The first is the assumption of the usual Hamiltonian defined in all space

$$H\psi = E\psi \qquad (2.1$$

and the subsequent applicability of nonrelativistic quantum mechanics. The other, more restrictive, assumption is the limitation to two-body channels only. This restriction implies the existence of some finite separation distance, a_c, beyond which neither nucleus experiences any polarizing potential field from the other.

Whereas little knowledge about the nuclear potential or residual interaction is included in the application of R-matrix theory, its remarkable success at fitting observed resonances with unique parameters, for a given radius, is the basis for its use.

The actual formulae derived from this theory and applied to experimentally determined cross sections are discussed in Appendix A.

B. Theory of Analogue States

In 1937 Wigner and others observed that charge independence of the nuclear interaction implies the existence of a quantum number for nuclear states, the isobaric spin. From the validity of this quantum number there follows the existence of multiplets of corresponding states in isobaric nuclei, the analogue states. In recent years, these analogue states have been the subject of intensive study, both experimental and theoretical.

In attempting to understand the basic concept of analogue states, it is useful to first consider the two systems proton + target, $|pC\rangle$, and

neutron + target, $|nC\rangle$. We assume that the target has pure isobaric spin $T_o = T_{oz}$. If we expand the states $|nC\rangle$, $|pC\rangle$ in terms of total isobaric spin T we find[7]

$$|nC\rangle = |T_o T_o;\ 1/2\ 1/2\rangle = |T_o\ 1/2\ T_o + 1/2;\ T_o + 1/2\rangle \qquad (2.2)$$

$$|pC\rangle = |T_o T_o;\ 1/2\ -\ 1/2\rangle = (2T_o+1)^{-1/2}\,|T_o\ 1/2\ T_o + 1/2;\ T_o - 1/2\rangle$$

$$+ (2T_o)^{1/2}\,|T_o\ 1/2\ T_o - 1/2;\ T_o - 1/2\rangle \qquad (2.2')$$

where the notation $|T_o T_{oz};\ tt_z\rangle$ and $|T_o\ 1/2\ T;\ T_z\rangle$ is used to represent the uncoupled and vector coupled states respectively. We see that the states $|nC\rangle$ have pure isobaric spin, but that the $|pC\rangle$ system involves two components $T = T_o \pm 1/2$. The states with $T = T_o + 1/2$ are the isobaric analogues of the $|nC\rangle$ states and those with $T = T_o - 1/2$ have the same isobaric spin as the ground state of the system (p + C).

In other words, if we operate on a low lying state $\psi_{N,z}$ in the system $|nC\rangle$ with the isobaric spin lowering operator $T_- = T_x - iT_y$, there results the analogue state $\psi_{N-1,z+1}$ resulting from changing a neutron into a proton. The analogue state differs from the "parent" state by essentially the Coulomb energy of the additional proton.

This concept is perhaps best illustrated by considering a particular experiment. We consider the reaction $^{40}A(p,p)^{40}A$ resulting in the formation of the compound nucleus ^{41}K. The pertinent level structure of ^{41}A and of ^{41}K is shown in Fig. 1. Two resonances are seen in the gross structure measurements[8] of compound states in ^{41}K which have

Figure 1. Level Diagram of ^{41}A and ^{41}K. The analogues of the fourth and sixth excited states of ^{41}A are indicated.

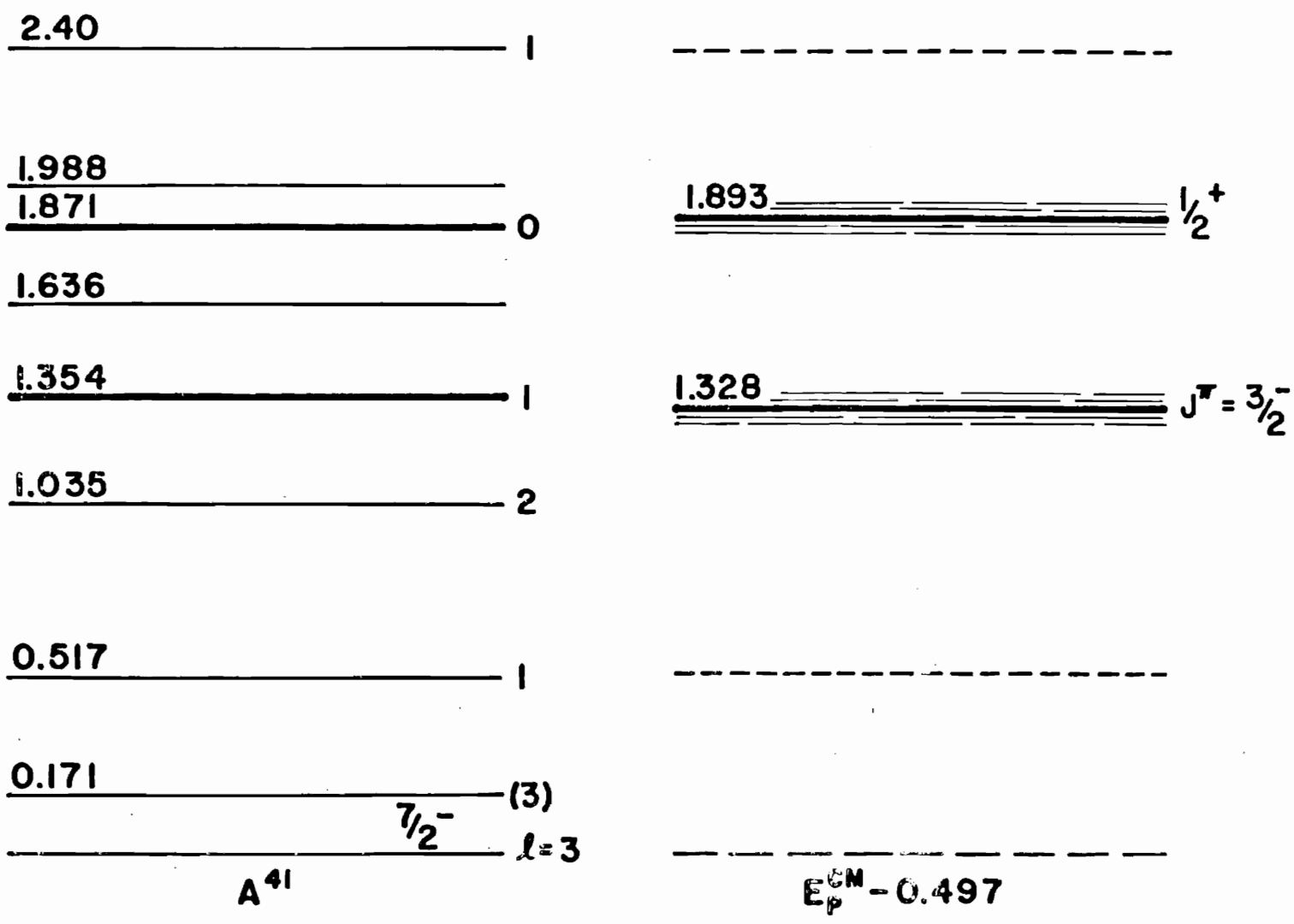
2.40
1
1.988
1.871
0
1.636
1.354
1
1.035
2
0.517
1
0.171
(3)
7/2⁻
l=3
A41
1.893
1/2+
1.328
Jπ = 3/2⁻
Ep CM - 0.497
A40 + P
K41

the same spin and parity as the fourth and sixth excited states of ^{41}A. The configuration of these corresponding states is essentially the same in both nuclei except for the interchange of a proton and neutron. The separation between corresponding states is $\Delta E_c - \delta$, where ΔE_c is the Coulomb displacement energy and δ the neutron-proton mass difference. The two observed resonances are the isobaric analogues of the corresponding "parent" states in ^{41}A.

It has been previously mentioned that there exist two components of the total isobaric spin of the $|p\,C\rangle$ system, $T_>$ and $T_<$. Since Coulomb forces mix these two components, T is not a good quantum in the system $|p\,C\rangle$. Robson,[7] however, has developed a theory of isobaric analogue resonances in the framework of R-matrix theory wherein the configuration space is divided into an internal and external region. He argues that T-spin may be relatively pure within the internal region defined by $r < a_c$, where a_c is the radius of the charge distribution. The set of states defined within this region is the set of compound nucleus states. Since such a set of states involves only the internal region, T may be relatively pure for them. The effects of external mixing show up when the internal and external solutions of the Schrödinger equation are smoothly joined in order to calculate the collision matrix.

Of particular interest is the case of a state with isobaric spin $T_>$ (the analogue state) imbedded in a background of states with different isobaric spin $T_<$. Robson[7] has investigated the effects of external mixing in

such a system for the case of elastic scattering. The result is an enhancement in the excitation of the $T_<$ states.

A characteristic feature of analogue resonances which was observed in the earliest fine-structure work was an asymmetry of this fine-structure enhancement; considerably stronger fluctuations were observed at energies below the analogue resonance than above. Robson[7] predicted this phenomenon as a natural consequence of coherent interference between the two contributions to the width of each fine-structure resonance; i.e., the width it would have in the absence of mixing with the analogue state and the portion of the analogue that mixes with it. In the simple case of the analogue of a single-particle state, Robson[7] derives the enhancement factor

$$|f_\lambda|^2 = \frac{(E_\lambda - E - \Delta_\lambda)^2}{(E_\lambda - E)^2 + \left(\frac{\Gamma_\lambda}{2}\right)^2} \qquad (2.3)$$

where E_λ is the energy of the analogue state, Γ_λ its decay width and Δ_λ the energy shift. Only $T_<$ states of the same spin and parity as the analogue are affected.

Thus, out of external mixing considerations, one expects to find an enhancement of the suitable $T_<$ states in the region of the $T_>$ analogue state. In compound nucleus formation, high excitation energies are usual and the density of these background levels is high. If the energy resolution available in an experiment is not sufficient to separate these background components, then a single gross-structure resonance may be seen with

the asymmetry described by eq. (2.3).

Although Robson's[7] R-matrix approach to analogue states has met with striking success, it has not fully satisfied the desire for a physical description of analogue states. In recent years, a number of approaches[9-19] within the framework of the shell model have been developed. Whereas the formalisms of the R-matrix and shell model approaches differ less than might be expected, the terminologies are quite different.

The basis for the R-matrix approach of Robson and others[7, 20] is, as discussed above, the division of the configuration space into an internal and an external region. The shell model approaches attempt to dispense with this formal concept and examine the analogue state in a more microscopic manner.

In the particle-hole picture of Block and Feshbach,[12] the virtual state of the incident particle and target nucleus may mix with a 2 particle-1 hole (2p-1h) "doorway" state via the nucleon-nucleon interaction. This doorway is interpreted as a $T_>$ state and the background $T_<$ states are composed of more complex configurations, such as 3 particle-2 hole (3p-2h). Whereas the incident particle cannot mix directly with these background 3p-2h states, the doorway can, thus serving as an intermediary between the incident particle and 3p-2h states. The doorway can thus decay via the Coulomb interaction into the more complicated background of $T_<$ states. In an experiment with sufficiently high resolution, such as the

work described in this dissertation, these individual decay modes are studied in the fine structure, while, in a poorer resolution experiment, the effect is to average over the coupling of the doorway to the 3p-2h states. In this latter case, the total width of an observed compound nucleus resonance is made up of two components:[13]

$$\Gamma = \Gamma^{\uparrow} + \Gamma^{\downarrow} \qquad (2.4)$$

where $\Gamma^{\uparrow}$, the escape width, is the usual width for single particle decay to the continuum and $\Gamma^{\downarrow}$, the damping width, is the width for decay into more complicated configurations. The escape width is a well known concept, but the damping width, a concept well substantiated in the ^{40}A (p, p) ^{40}A experiment described herein, is difficult to calculate since the entire density of complicated states must be considered. In several theories[14, 15] the value of $\Gamma^{\downarrow}$ is obtained as a parameter by comparing to experiment. Assuming that the nucleon-nucleon interaction provides the coupling between the 2p-1h and 3p-2h states and taking into account the Coulomb interaction, without assuming isobaric spin as a good symmetry, Beres et al.[19] have calculated the damping width $\Gamma^{\downarrow}$. However, their work is restricted to even-even nuclei with closed neutron and proton subshells.

In the particle-hole picture the concept of the analogue state is schematically represented in Fig. 2. It is evident from this figure that there are $2T_0 + 1$ possible particle combinations which produce the analogue state configuration. This would imply a simple relation between the energy independent reduced width of the parent single particle state and

Figure 2. A Particle-Hole Picture of the Analogue State. The $2T_o$ particle configurations of the 2p-1h doorway state are shown.

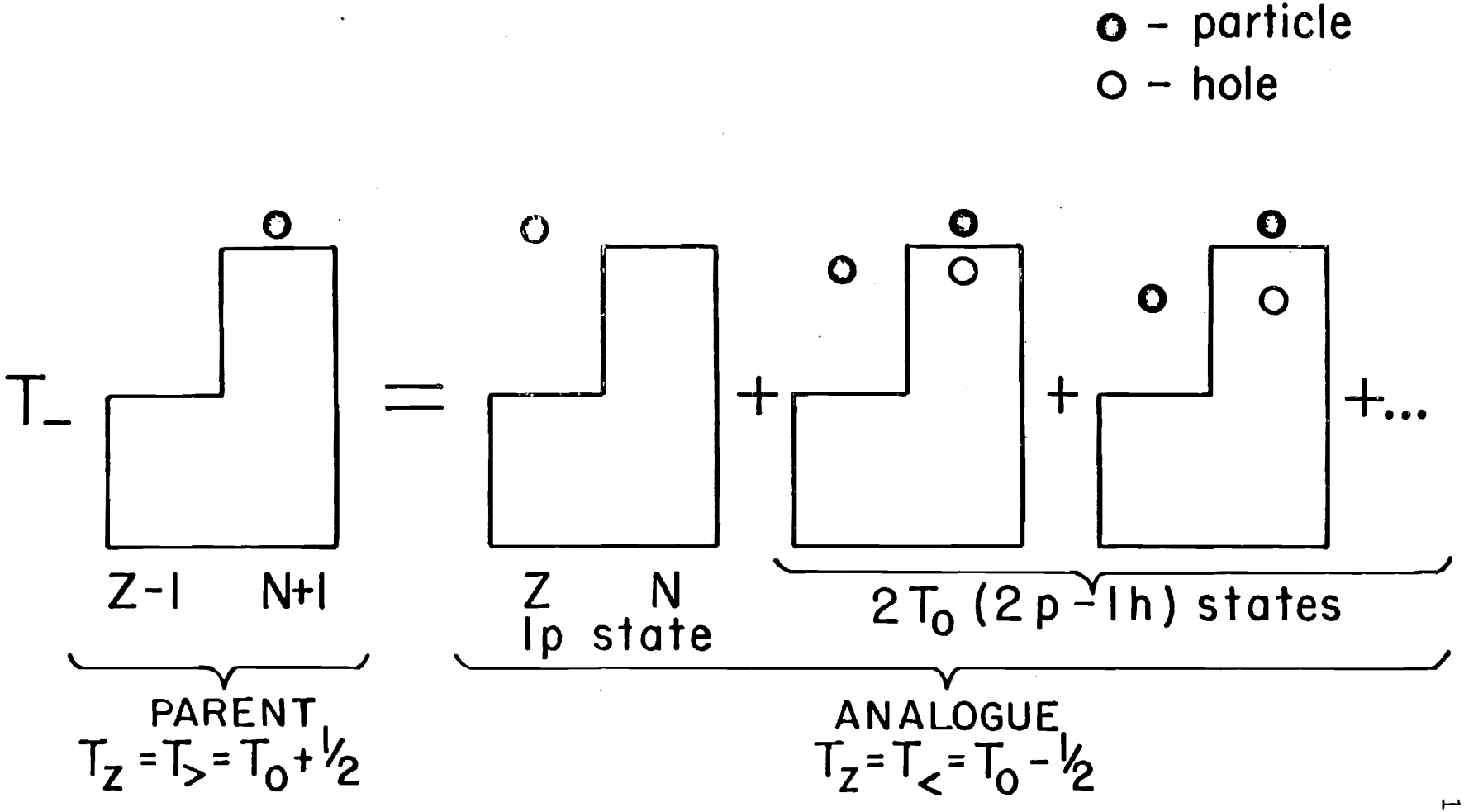
● – particle
○ – hole
T–
=
+
+
+...
Z-1 N+1
Z N
1p state
2 T0 (2p–1h) states
PARENT
Tz = T> = T0 + ½
ANALOGUE
Tz = T< = T0 – ½

the width of the analogue state observed in elastic proton scattering:

$$\gamma_p^2 = \frac{1}{2T_o + 1} \gamma_n^2 \qquad (2.5)$$

where γ_p^2 is the proton reduced width of the analogue, T_o is the isobaric spin of the target and γ_n^2 is the reduced width of the parent state, normally deduced from a (d, p) experiment.

In order to obtain the width of the analogue state, Γ_p, from a high resolution measurement of the fine-structure, a sum rule can be applied to the reduced widths of the individual narrow resonances. The form of this rule is essentially the same in either the R-matrix or shell model formalisms, and is given by [21]

$$\gamma_p^2 = \sum_\nu \gamma_{\nu p}^2 - \sum_\mu \gamma_{\mu p}^2 (T_<) \qquad (2.6)$$

which relates the proton reduced width before isobaric spin mixing is introduced to the sum of the reduced widths for all levels nearby after the mixing is introduced. The proton widths Γ_{ν_p} are the directly observed fine-structure widths and the Γ_{μ_p} may be estimated from the average value of the proton widths away from the region of enhancement. Robson[21] has pointed out that averaging the fine structure resonances over energy and using a single-level formula to extract a width for the resultant gross-structure resonance does not directly determine Γ_p necessarily, since this quantity is actually only defined in a theoretical system.

Several factors will determine the size of the observed proton

widths of the analogue state. The most obvious is that the spectroscopic factor for the parent state must be sufficiently large to make an observable increased strength in the compound system. Similarly, the penetration factors, dependent upon the angular momentum of the projectile and upon the magnitude of the Coulomb barrier, must not be too small, in absolute magnitude or relative to the penetrabilities for decay through other channels.

Chapter III

EXPERIMENTAL APPARATUS AND PROCEDURE

In the process of attempting to develop a monoenergetic neutron source at Duke University, two major problems were encountered and, to a large degree, overcome. The first is the inherent limitation on Van de Graaff accelerators in producing monoenergetic proton beams, and the second is the beam spread normally resultant from the target.

An electronic system which largely overcomes the first difficulty was developed by Parks et al.[22] and will be only briefly described here. Concern with the second problem led to the development of a cryogenic system for the production of very thin targets[4] in which the $^{3}T(p,n)^{3}He$ or other reactions might be utilized as a neutron source. Further development in conjunction with the work described in this dissertation resulted in a cryogenic target chamber employing solid state detectors to measure charged reaction products.

The general floor plan of the laboratory for this work is shown in Fig. 3. The two most pertinent features in high resolution experiments are the electrostatic analyzer and the homogenizer systems. The

Figure 3. Floor Plan of the Laboratory. The neutron collimator and matrix, used in the ^{40}A experiment, detects neutrons at an angle of 20°.

FLOOR PLAN

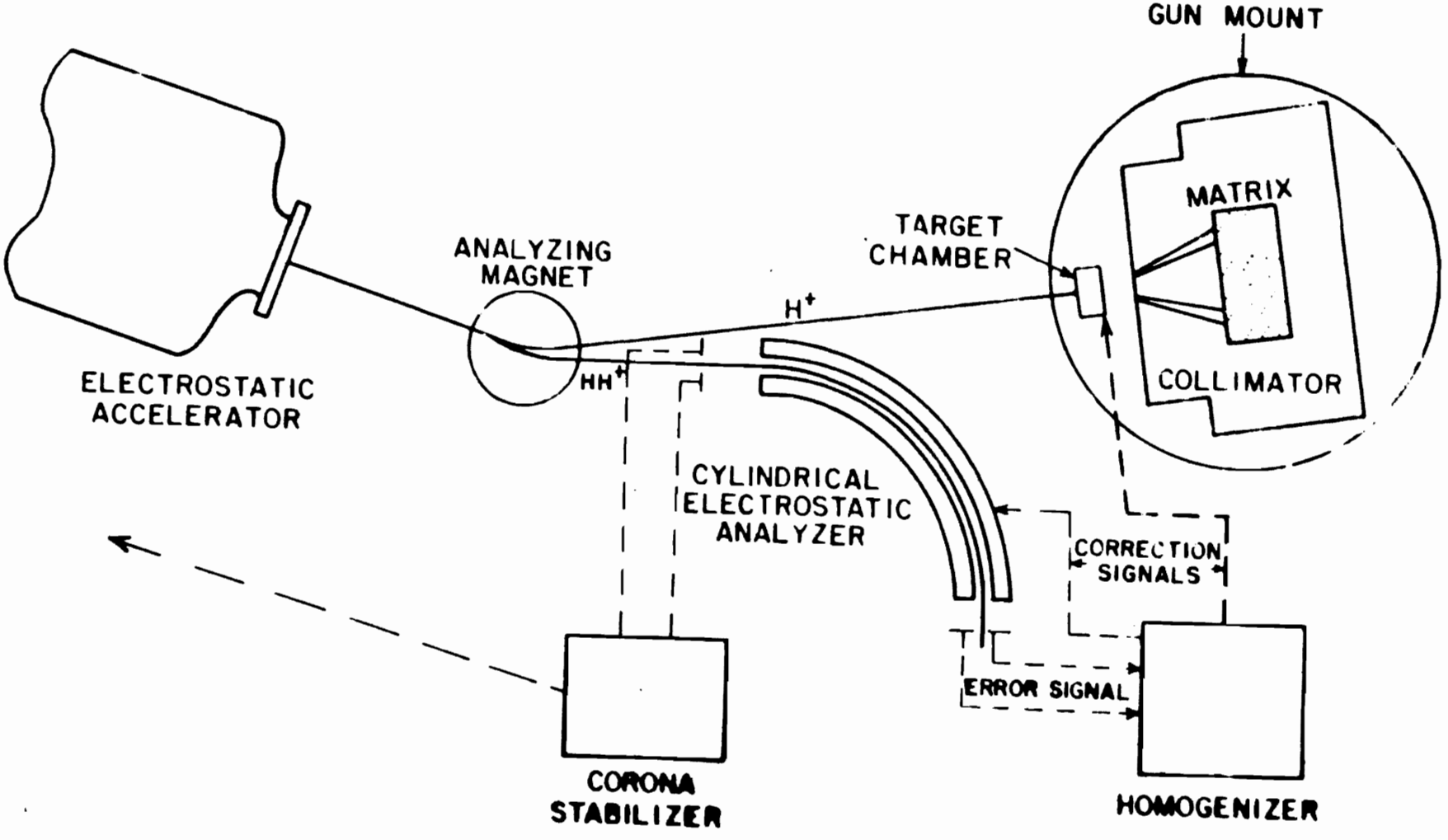
GUN MOUNT
MATRIX
TARGET CHAMBER
ANALYZING MAGNET
H+
HH+
ELECTROSTATIC ACCELERATOR
COLLIMATOR
CYLINDRICAL ELECTROSTATIC ANALYZER
CORRECTION SIGNALS
ERROR SIGNAL
CORONA STABILIZER
HOMOGENIZER

1-meter radius electrostatic analyzer[23] is used to permit precise and continuous knowledge of the beam energy. Specifically, the HH^+ beam from the accelerator is passed through the analyzer and is used for energy control and calibration. In addition, the homogenizer system derives an energy correction signal from the analyzer image slits. The target chamber is normally operated at a positive potential of 3500 volts and is modulated with the homogenizer correction signal. In this manner the slow time-dependent energy variations in the beam are effectively cancelled resulting in a total energy spread of as low as 110 eV. Perhaps the most significant feature of this technique is that the resolution is obtained by a feedback correction technique, thereby permitting use of the full H^+ beam, rather than by merely selecting a narrow fraction of the emitted beam. The great advantage of this technique is evident in the fact that we have utilized beam currents through the target chamber of as high intensity as 100 μa. This is a necessary feature since the target thickness has become extremely small.

A. The Cryogenic Target Chamber

The development of the cryogenic charged particle target chamber was essentially a two-step process. The first device utilized the liquid helium reservoir from the original neutron chamber and allowed detection of reaction products at only one angle. Although there were

many operational difficulties involved in its use, the ^{40}A data presented here were acquired with this prototype. Further development resulted in the present chamber in which six solid state detectors may simultaneously count reaction products at six different angles and in which the counting difficulties encountered in the prototype were overcome. In addition, a system, to be described later in this section, had to be developed which could feed and recover quantities of enriched isotopes in gaseous forms for use with the cryogenic target chamber.

The basic operation of the cryogenic target chamber is perhaps best understood by following the path of the gas. Utilizing a gas handling system which, for natural argon, is simply a gas cylinder and pressure regulator but which, for enriched isotopes, is more complex and is described in part B. of this section, a reservoir of the target gas is maintained at a constant pressure of about 1 atm. This reservoir serves as the input to a flow gauge which controls, by means of a manual needle valve, the rate of flow of gas into the target chamber. Except for a short insulating section of Tygon, a long copper tube delivers the gas to the cryostat from the console area, where the flow rate can constantly be monitored. Use of a ball-type flow meter resulted in flow rates easily reproducible to ±5%.

The cryostat (Fig. 4) is capable of containing all commonly used liquid refrigerants. In the work described here, liquid helium at 4.2° K was used. All the refrigerant containers and appendages are made of copper. Polished copper is particularly suitable because of its high

Figure 4. The Cryogenic System. Cryostat and Appended Target Chamber.

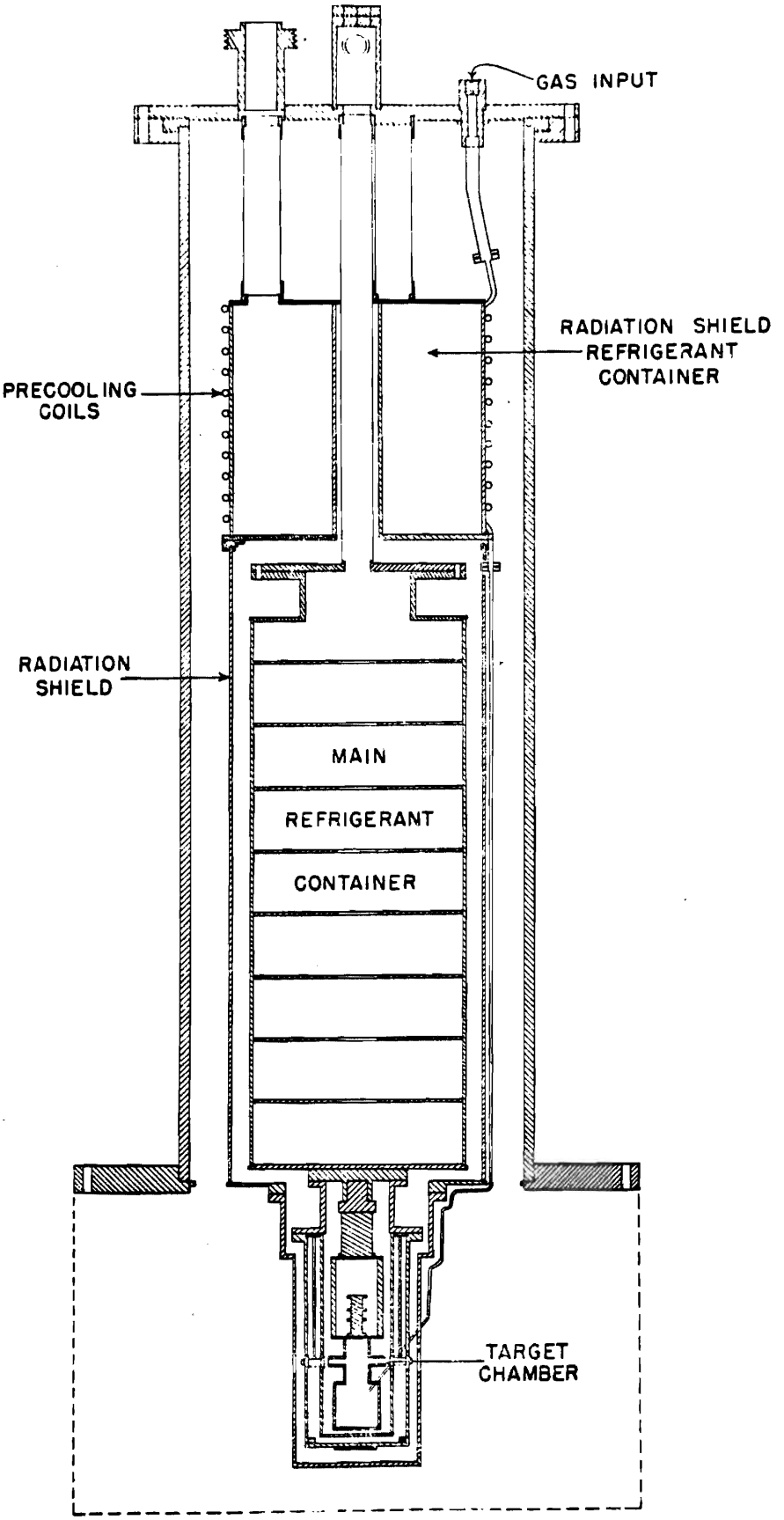

CRYOGENIC GAS TARGET

reflectivity in the infrared range. Due to the difficulty, however, of maintaining a polished surface, these surfaces were gold plated in the later version. It is also necessary to surround the main refrigerant container with a radiation shield, cooled with liquid nitrogen to 77°K. The main refrigerant container is supported by a long (10") stainless steel tube whose wall thickness is only 0.010", to minimize heat conduction. The fragility resulting from this tenuous support is such as to require external support when the cryostat is turned upside down for maintenance. However, with this precaution and, in particular, extreme care in fabrication, vertical alignment to within a few thousandths of an inch is maintained at the bottom of the target chamber.

To minimize heat input to the helium reservoir, the gas is precooled in a copper coil soldered to the radiation shield reservoir. Ideally, a refrigerant should be chosen for this purpose which has a boiling point close to or slightly below that of the target gas. For argon, whose atmospheric boiling point is 87.4°K, liquid nitrogen or oxygen are both suitable. However, for neon, which boils at 27.4°K, no practical refrigerant exists in the desired neighborhood. Here also liquid nitrogen was used.

The precooled target gas passes through a stainless steel capillary tube and enters the cooling cavity of the target chamber (Fig. 5) where it attains temperature equilibrium. Just before the capillary tube enters the target chamber, a 5W resistor is soldered to it and may be heated to prevent condensation of the gas inside the tube.

Figure 5. The Cryogenic Target Chamber. Gas enters the cooling cavity through a capillary tube and eventually condenses on the trapping cylinders. The reaction products reach each of the six detectors positioned at 90, 105, 120, 135, 150, and 160° by passing through rectangular slots in the wall of the reaction chamber.

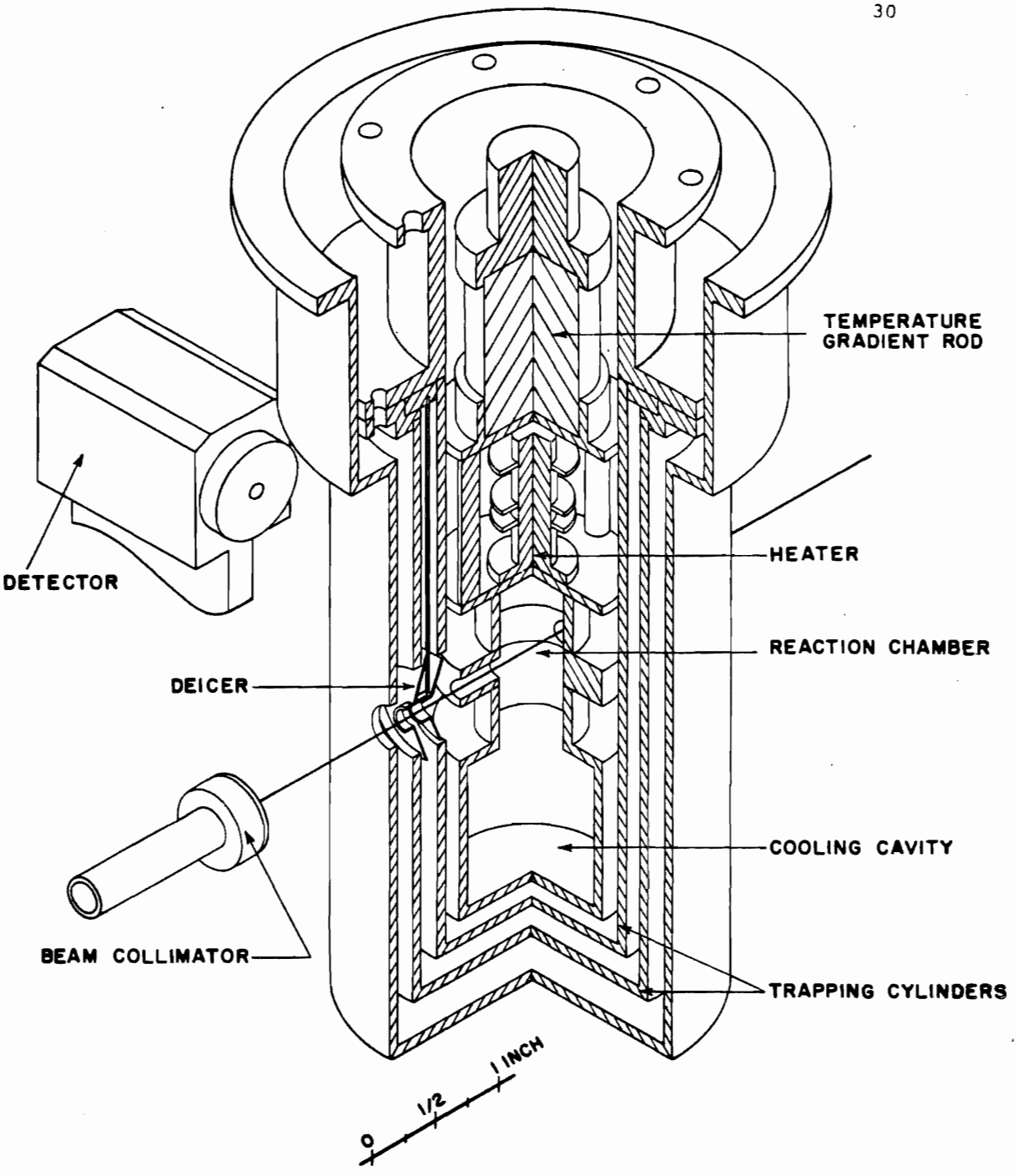

CHARGED PARTICLE CRYOGENIC TARGET CHAMBER

The temperature of the cooling cavity and reaction chamber must be maintained at a temperature well above the minimum temperature to prevent condensation. This temperature is attained by selecting a temperature gradient rod, which connects the reaction chamber assembly to the helium reservoir; so as to maintain a suitable balance between heat input from the target heater and the gas, and heat flow out through the gradient rod. In the cases of argon and neon, stainless steel rods were chosen, which conduct 5 and 12.5 mw/$^{\circ}$K respectively, to permit operating temperatures of 60 and 20°K.

After reaching temperature equilibrium, the gas diffuses into the reaction chamber where it is bombarded by a well collimated proton beam which passes through two "reaction tubes" in the wall of the reaction chamber. Since the target chamber is windowless, there is nothing to prevent the escape of the gas, but because of the constricting length of the reaction tubes, the effusion rate is decreased by about a factor of four over holes of the same diameter. After leaving the reaction tubes, most of the gas condenses on the trapping cylinders. The trapping efficiency is sufficiently high to allow gas flows as high as 500 cc/min., thereby increasing the pressure in the region of the target, before the vacuum in the beam pipe is significantly affected. However, in normal operation, gas flow rates of from 4 to 12 cc/min. were realized. These flow rates were chosen to maximize the total number of counts obtainable with a single charge of liquid helium.

Scattered particles were observed in solid state detectors after passing through holes in the wall of the reaction chamber. In the prototype device, only one exit hole, at 135°, was available. Presently, there are six holes at 90, 105, 120, 135, 150 and 160°. The entire device may also be rotated through 180° to give the same six angles in the forward quadrants. The solid angles subtended in this arrangement are variable, since the detector holders are movable, from a minimum determined by the detector collimator to a maximum of about 15 msr. The exit holes are sufficiently small in area to ensure that the gas loss from the reaction chamber takes place primarily through the reaction tubes. A serious difficulty arose in the prototype chamber as a result of the design of the exit hole. The diameter of the reaction tube through which the beam passes was, and is, 1/8" whereas that of the exit hole was 1 mm. As the beam moved up and down slightly, as a result of unavoidable changes in the focus or beam steering system, the effective target visible to the detector changed and resulted in drastic yield changes. In the present device, however, vertical slots were constructed which cover the entire vertical range of the beam. This change has resulted in a yield change of less than 1% during maximum manual deflection of the beam through the cryostat.

In the original cryogenic neutron target chamber, it was discovered that, as long as the chamber continued to operate, the condensed solid tended to grow inward from the edges of the beam holes in the trapping cylinders until it was struck by the beam. To eliminate this problem,

two "deicer" assemblies were installed along the beam path. In the charged particle chamber, not only the beam holes required deicers but also each of the exit passages. Not only are these devices required to prevent condensation in the beam path, but they are critical in determining the effective trapping. Each deicer assembly consists of baffles, a thin wire mesh and a resistance heater all mounted on a stainless steel capillary tube in contact with the main refrigerant reservoir. The baffles are important in directing the effusing gas toward the trapping surfaces. The deicers are operated at a temperature close to that of the target chamber, just high enough to prevent condensation.

During and particularly when beginning operation of the target chamber, it is essential to know the temperature of the reaction chamber and cooling cavity so as to introduce the correct amount of electrical heating to prevent condensation. In the early target chamber a 1/2 W carbon resistor whose resistance was calibrated against a series of known temperatures down to 4.2°K was used as a thermometer. The temperature was monitored with an ac Wheatstone bridge. Due to inaccuracies at temperatures below 40°K and reproducibility failures, we have substituted in the present chamber a commercial ("Cryo-Cal") thermistor which is monitored with a dc bridge. With this device it is relatively simple to obtain absolute measurements of $\pm 3^{\circ}$K and reproducibility of $\pm 0.5^{\circ}$K.

The material of the target heater and all electrical leads is manganin wire ($\lesssim$ 0.004" diam.). This material is commonly used in

cryogenic systems due to its low thermal conductivity.

The entire assembly including refrigerant reservoirs and cooled surfaces is insulated from ground to support the 3500 volt homogenizer potential. In addition, the control panel for controlling the resistance heaters is insulated. The source of power for the electrical heating is two 12 volt automobile batteries. Temperature readings may be taken only with the homogenizer potential removed.

In contrast to the neutron and prototype charged particle target chambers, the present system is self-contained. That is, its vacuum system, control panels, mounting system and collimator assembly are mounted on a rigid mobile table which can be fixed in position and attached to the beam pipe. The main vacuum pump is a 3" four-stage silicon oil diffusion pump whose pumping speed is 350 liters/sec. A 5 liter capacity "thimble" type liquid nitrogen trap is located over a water cooled chevron baffle. Two gate valves, one isolating the accelerator vacuum system, the other isolating the diffusion pump, are pneumatically operated and interlocked with a vacuum gauge so as to automatically close when the internal pressure exceeds 10^{-5} torr. This effectively prevents escape of an enriched isotope when the liquid helium supply is exhausted. All components of the cryogenic system are either vacuum type stainless steel or nickel or gold plated copper and brass to minimize outgassing. The entire system will pump down from atmospheric pressure to 10^{-5} torr in 5 minutes and will reach 5×10^{-7} torr in 3-4 hours. The foreline has two

ballast tanks in it so that one mechanical pump can be used both to pump a rough vacuum in the chamber and as a forepump for the diffusion pump.

Because the effective target thickness is very small (< 10 eV at the energies involved here), large beam intensities are required to produce reasonable counting rates. Associated with the use of intense beams are many handling difficulties. In actual practice, errant beam has vaporized components of the target chamber in addition to rapidly boiling off the liquid helium. A well-focussed stable beam from the accelerator is required which is further focussed with two quadrupole magnets on the beam pipe. Precise steering is obtained with an electrostatic deflector before the analyzing magnet and two pairs of deflecting magnets before and after the quadrupole magnets. The beam is collimated just before entering the target chamber to a beam diameter of 1/16" in a series of water cooled tantalum collimators. In addition, precise lateral and vertical adjustment of the cryogenic system is available with the present mounting system. With this arrangement beam currents through the chamber of as high as 100 μa have been realized. Collecting a beam this intense for current integration introduced a further difficulty. The power density of as high as 80 kW/ $in.^2$ in the form of heat is too great to remove by conventional air cooling. A Faraday cup was constructed which is slanted 30° to the beam direction in order to increase the size of the beam spot, and water cooling introduced through a 50' hose was employed. The long water line is used to reduce possibility of erroneous charge integration through charge loss

via the water line. With this device no deterioration of the molybdenum beam stopping surface was observed. Utilizing such intense beams, counting rates of 2000-5000 counts/20 sec. interval were obtained. Due to the collimation and the narrow acceptance angle of the detectors, background is totally removed except in the low energy portion of the spectrum.

Due to the geometry of the target and exit port system, the target thickness is proportional, for a given detector acceptance angle, to $(\sin\theta)^{-1}$, where θ is the scattering angle. This yield increase with angle tends to offset the decrease in the Rutherford scattering yield at back angles. However, the target thickness in these experiments was at all times so small that the total resolution function had no angular dependence.

B. The Rare Gas Handling System

There are two significant advantages to using a stable target gas in its natural abundance, such as argon which is 99.6% ^{40}A. These are that it does not have to be recovered for reuse and that a large enough supply may be used so that the pressure in the reservoir remains essentially constant during one entire run. This latter consideration allows us to use an ordinary diaphragm type pressure regulator to maintain a constant pressure in a reservoir before the flow gauge. In the case of elements whose liquids are readily obtainable, such as oxygen or nitrogen, the dif-

ficulty is minimized because the gas reservoir may be maintained in thermal equilibrium with its liquid by immersion in a flask containing the liquid, as demonstrated by Beard,[40] resulting in the desired internal pressure of 1 atm. However, in the case of neon as a target gas, this method was not feasible due to the cost of liquid neon. The same effect had to be obtained by mechanical means. A small (100 cc) reservoir was constructed to contain the initial volume of gas (4 liters of ^{22}Ne) at a high pressure ($\sim$ 600 psi). In order to feed this gas at a constant slow rate into the target chamber, two mechanical leaks (Fig. 6) were installed in series in the line connecting the high pressure reservoir to the low pressure reservoir at the input to the flow meter. The first leak serves simply as a throttle valve; the second, however, is servo-mechanically controlled. A capacitance manometer compares the pressure in a reference cell at 1 atm. to that inside the low pressure reservoir. When the pressure drops, the servo-valve is opened slightly; when the pressure rises, it is closed. A pressure of 1 atm. $\pm$ 2% may be maintained in the reservoir in this manner. This is well within the control range of the flow meter. The only adjustment required during operation before the gas supply is exhausted is to open the throttle valve as the pressure in the main reservoir drops below 50 psi.

The other difficulty associated with a rare gas is more readily overcome; that is, the necessity for recovering the condensed gas. With a naturally occurring gas, the condensate is allowed to boil off and is pumped

Figure 6. The Gas Handling System. The liquid helium dewar is raised to cool the recovery reservoir during recovery.

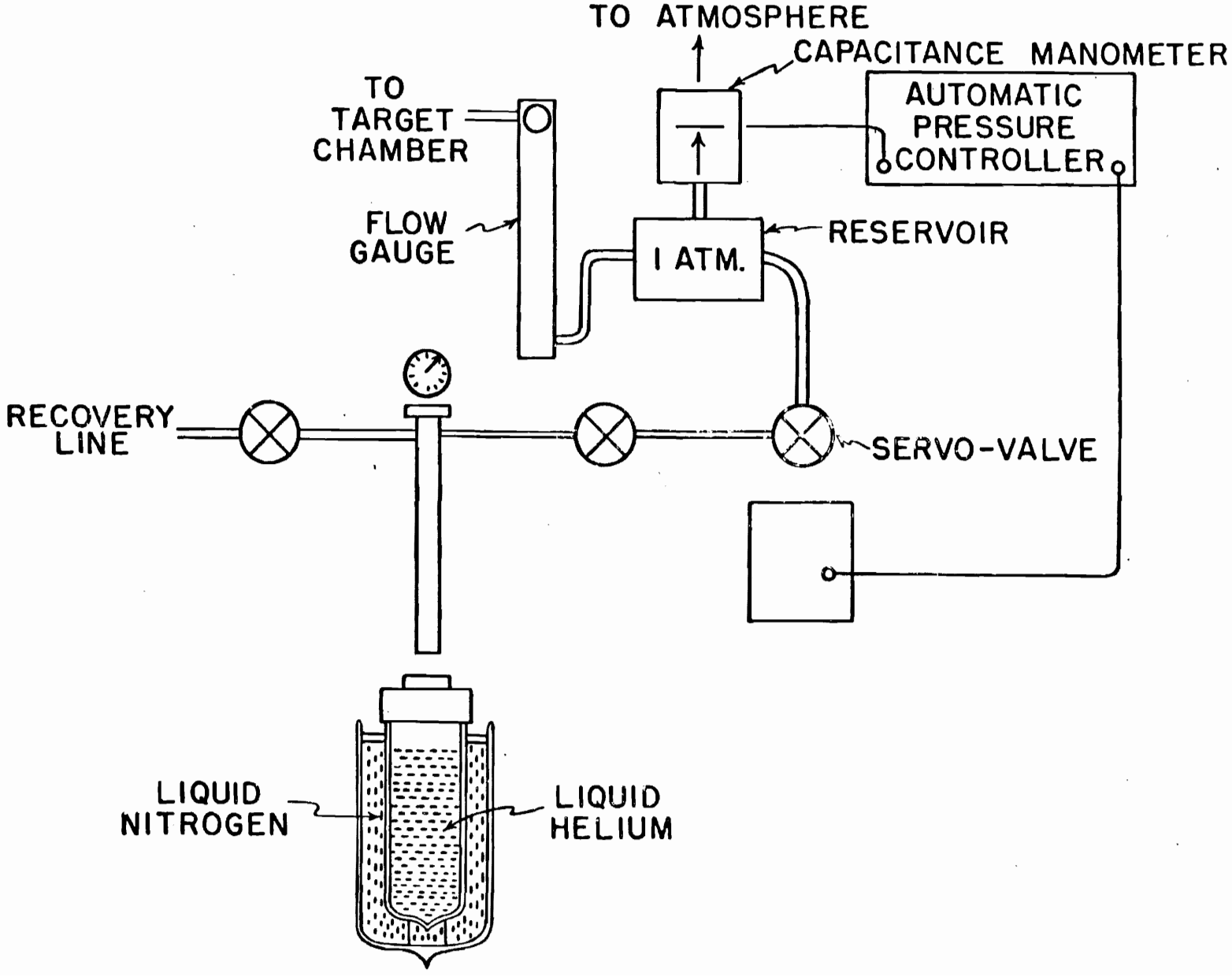
TO ATMOSPHERE
CAPACITANCE MANOMETER
TO TARGET CHAMBER
AUTOMATIC PRESSURE CONTROLLER
FLOW GAUGE
RESERVOIR
I ATM.
RECOVERY LINE
SERVO-VALVE
LIQUID NITROGEN
LIQUID HELIUM

out of the chamber into the atmosphere. The rare gas, however, is returned to the main storage reservoir by cryogenic pumping. A "trap dewar" containing liquid helium and itself immersed in liquid nitrogen is raised to cool the reservoir to liquid helium temperature. A valve is then opened on the recovery line and the gas is condensed in the desired reservoir. Approximately 30 minutes was sufficient time to reduce the pressure of ^{22}Ne in the chamber to below 0.1 torr. During recovery the main refrigerant container was filled with liquid nitrogen to keep most impurities condensed. Using this gas handling system, 4 liters of ^{22}Ne have been recycled more than 50 times with a total loss of 5% and no detectable contamination. In addition, the entire gas handling system fits into a standard electronic relay rack, as seen in Fig. 7.

C. Detectors and Associated Electronics

Standard commercial (ORTEC) surface barrier detectors with depletion depths of 300 μ were used throughout the experiments. At the outset of the argon experiment, rapid deterioration of the detectors took place when the homogenizer potential was applied. This effect was attributed to bombardment of the detector surface by argon ions and was prevented by introducing a 1μ nickel foil in front of the detector. Associated with each detector was a low-noise preamplifier whose signal was fed first to a linear amplifier, then to a biased amplifier. The resultant

Figure 7. The Entire Cryogenic System as in Operation. The cryogenic target chamber is mounted on a table containing the pumping system and water-cooled intense beam collimator. Behind the chamber is the neutron collimator. To the left, in the relay rack, is the gas handling system.

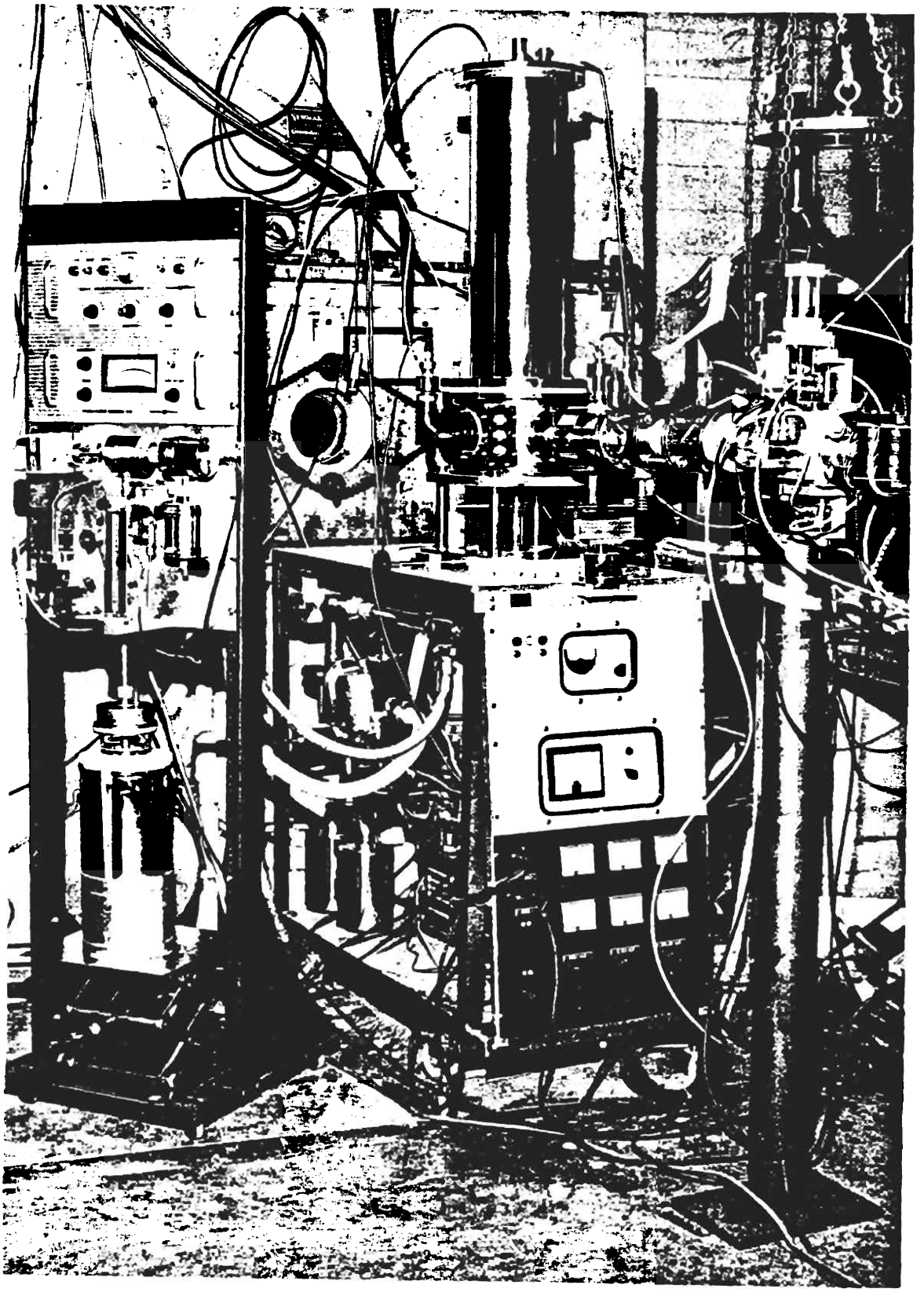

signal was analyzed in a number of single channel analyzers, one for each reaction product measured, and the output of each analyzer was counted in a scaler. A multichannel analyzer and pulser were used to accurately set "windows" in the single channel analyzers in order to discriminate all but the desired pulses. For elastic protons and higher energy particles these windows could be set quite wide (> 100 keV), due to lack of background, thereby minimizing window adjustments as a particular excitation function is taken. A beam current integrator was used to control the counting duration at each energy.

D. General Performance of the Cryogenic System

The actual procedure for operating the cryogenic system is to cool the target chamber to 77°K by filling the main refrigerant reservoir with liquid nitrogen. The time required for this initial precooling is a function of the size of the gradient rod used but was about two hours in the neon experiment. In normal operation, however, this time is greatly reduced because the device is not allowed to warm up appreciably during recycling. With the chamber and main reservoir precooled, the liquid nitrogen is removed by siphoning and liquid helium is transferred. Upon completion of this transfer, the temperature is monitored until the chamber approaches the desired operating temperature. Electrical heating is then introduced and the flow of gas begun. Approximately 10-15 minutes is

typically required for an equilibrium situation to be obtained. The operating duration, assuming an inexhaustible gas supply, is primarily dependent upon the rate at which heat is input to the liquid helium. Inherent heat leaks are small and the significant sources of heat are the electrical heating introduced and that released in cooling and condensing the gas. With proper choice of gradient rod, this latter should be the primary source of heat. In the present system, whose main refrigerant capacity is 5 liters, operating times of from 4 1/2 - 8 hours are typical for neon; the variation being dependent upon the gas flow. In the prototype device, whose helium capacity was 1.9 liter, the refrigerant was usually exhausted in 2 hours during the argon measurements. When the refrigerant supply is exhausted, the device is allowed to warm up until the condensed gas boils and is removed by conventional pumping or recovery. The precooling process is then resumed and recycling begun.

For maintenance, such as changing or adjusting the position of a detector, changing a gradient rod or making repairs, the system must be warmed to room temperature to prevent condensation of water vapor when air is introduced into the system. By passing air through the main reservoir, about 6 hours is required to reach room temperature.

The total resolution available with this system is a function of several factors: incident beam spread, target thickness and Doppler broadening in the target. Normally, at low temperatures, the incident beam spread is the dominant component. From the yield in the measure-

ments reported here, the thickness of target through which the beam passes is estimated to have an upper limit of 70 eV at 1.1 MeV proton energy. The effect of the Doppler broadening, calculated for an ideal gas, should have a half-width of about 37 eV for neon at 20°K. Investigations at Oak Ridge National Laboratory have indicated that the initial incoherent energy spread as the beam leaves the rf ion source is approximately 80^{-10}_{+30} eV.[24] Since the homogenizer is incapable of removing this source of beam spread, the total resolution at this energy would be expected to be 113 ± 30 eV. A resonance measured in 25 eV steps during trials with ^{20}Ne indicates an actual resolution of 110 eV (Fig. 8). In this measurement, the natural width of the resonance was found, by fitting it with a single-level Breit-Wigner shape, to be 8 eV. The natural width would thus not contribute significantly to the observed width in this case. More commonly, resolutions of 200-250 eV are realized. This discrepancy is felt to be caused by fluctuations in the beam energy which are too fast to be cancelled by the homogenizer and, possibly, deterioration in the rf ion source resulting in increased beam spread.

The nearly total lack of background resulting from the pure gas target and well defined detector acceptance angle is illustrated by the detector spectrum (Fig. 9). However, it was discovered that, for a low-yield reaction whose particle energy is less than 1/3 that of the incident beam, such as inelastic scattering in these experiements, that part of the spectrum did contain significant background. This background was found

Figure 8. A Resonance in ^{21}Na Measured with the Cryogenic System. An actual resolution of 110 eV (fwhm) is indicated for this measurement of a resonance seen in $^{20}Ne(p,p)^{20}Ne$ and found to have a proton width of <8 eV.

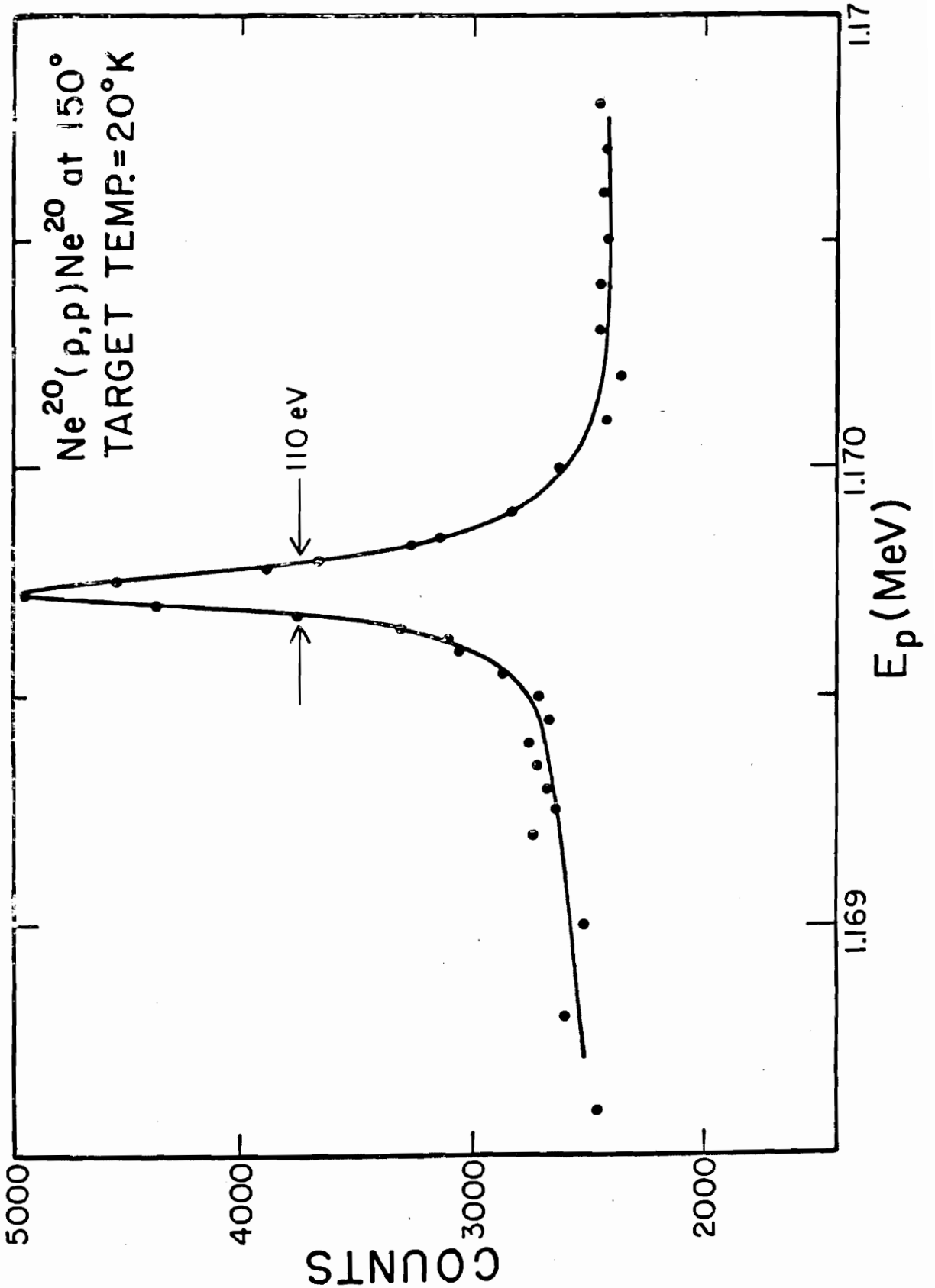
$Ne^{20}(p,p)Ne^{20}$ at 150°
TARGET TEMP.=20°K
110 eV
COUNTS
5000
4000
3000
2000
1.169
1.170
1.171
E_p (MeV)

Figure 9. A Typical Solid State Detector Spectrum in the ^{40}A Experiment. This spectrum was taken with a 100-channel pulse-height analyzer. The α-particle peak is expanded. This spectrum was accumulated over one entire data run during which the proton energy range was about 20 keV; the average incident proton energy was 2.35 MeV.

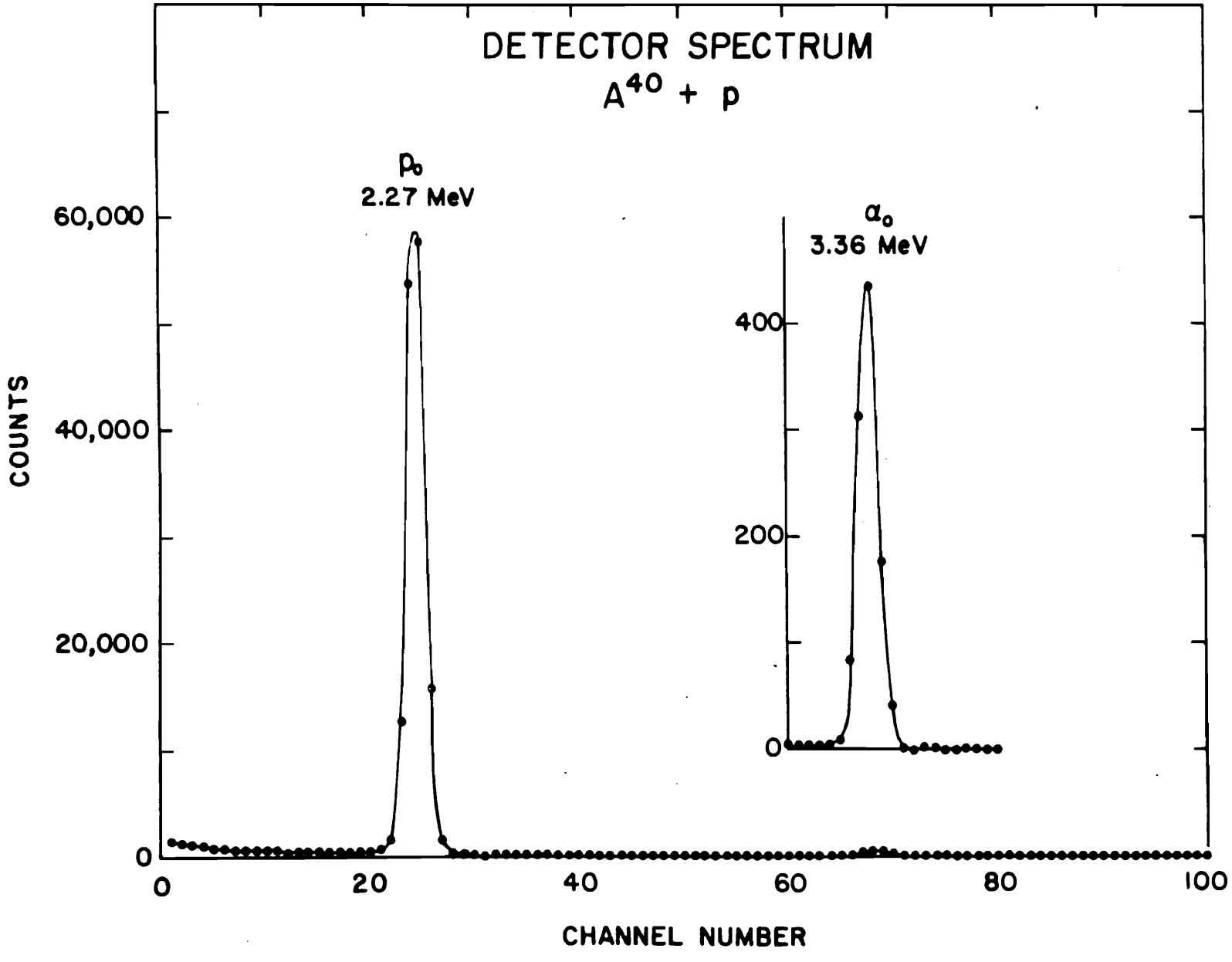
DETECTOR SPECTRUM
A^{40} + p
p_0
2.27 MeV
α_0
3.36 MeV
COUNTS
60,000
40,000
20,000
0
400
200
0
0
20
40
60
80
100
CHANNEL NUMBER

to come almost entirely from the last collimator which extends inside the base of the device. Adequately shielding this collimator effectively removed this background, permitting the inelastic measurements discussed in the later chapters to be made.

Chapter IV

RESULTS AND ANALYSIS

A. $^{41}K^{25)}$

Simultaneous excitation functions for $^{40}A(p,p)^{40}A$, $^{40}A(p,\alpha)^{37}Cl$ and $^{40}A(p,n)^{40}K$ were measured at incident proton energies of from 1.63 to 2.60 MeV with the elastic protons and α-particles detected at 135° and the neutrons (above threshold) at 20° (Figs. 10-13). The (p,n) data actually shown in Fig. 11 are those of Parks et al.,[4] which were taken with a target chamber similar to that used in the present experiment but specifically designed to allow 4π measurement; the (p,n) data obtained in the present experiment were used merely to align the 4π neutron data with the charged particle yield curves. Calibration of the charged particle data was obtained by overlapping each of the 70 separate data runs which comprise the total span and normalizing to the Rutherford cross section; absolute energy calibration was obtained by measurement of the $^{7}Li(p,n)^{7}Be$ threshold at E_p = 1880.4 keV.

Table 1 gives the results of the analysis of all resonances which were observable in the elastic cross section. The resonance

Figure 10. The $^{40}A(p,p)^{40}A$ and $^{40}A(p,\alpha)^{37}Cl$ data at 135° showing the beginning of the 1.87 MeV analogue resonance region.

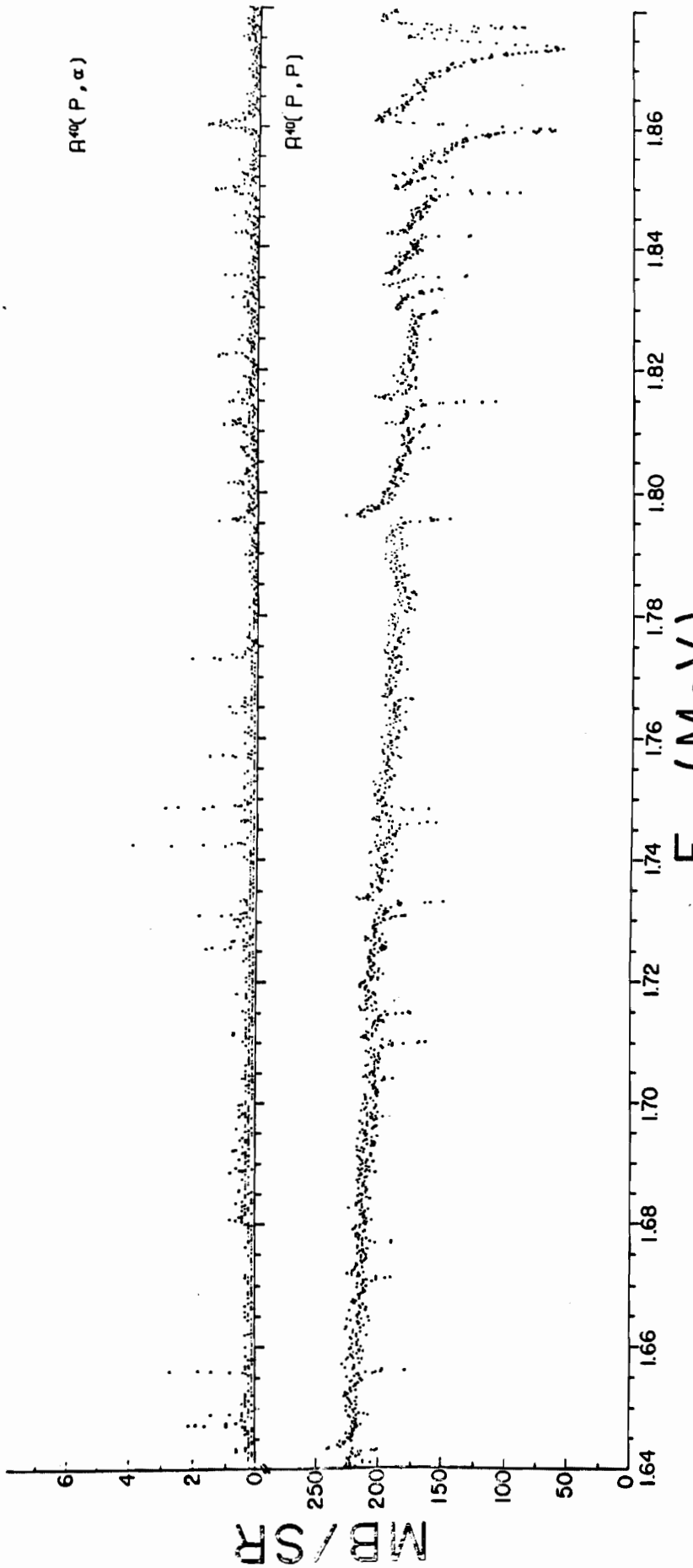
A40(P , α)
A40(P , P)
MB / SR
Ep (MeV)
6
4
2
0
250
200
150
100
50
0
1.64
1.66
1.68
1.70
1.72
1.74
1.76
1.78
1.80
1.82
1.84
1.86

Figure 11. Continuation of the (p, p) and (p, α) data showing the falling off of the analogue resonance structure near 1.87 MeV and the relatively smooth region following.

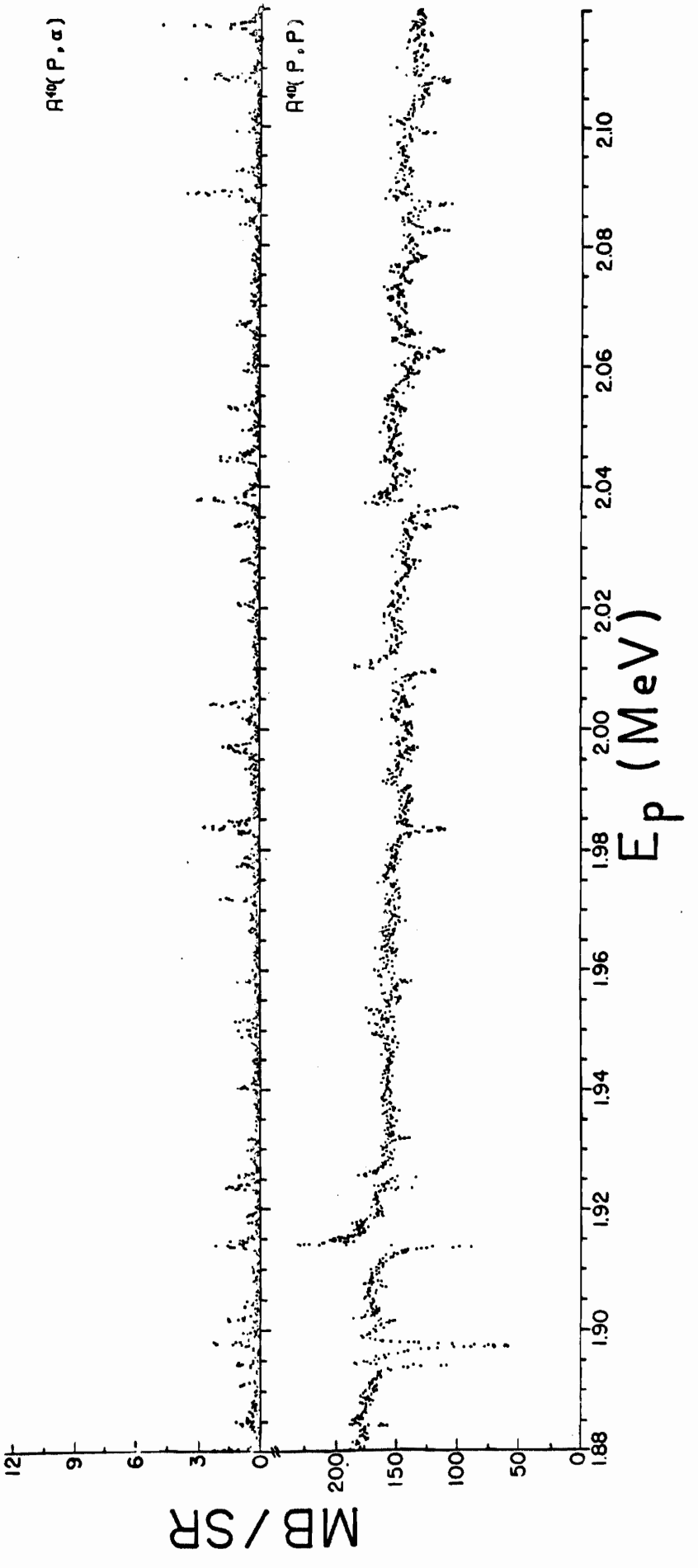
A40(P,α)
A40(P,P)
MB/SR
12
9
6
3
0
200
150
100
50
0
1.88
1.90
1.92
1.94
1.96
1.98
2.00
2.02
2.04
2.06
2.08
2.10
Ep (MeV)

Figure 12. Continuation of the data showing the relatively smooth region between the analogue resonances.

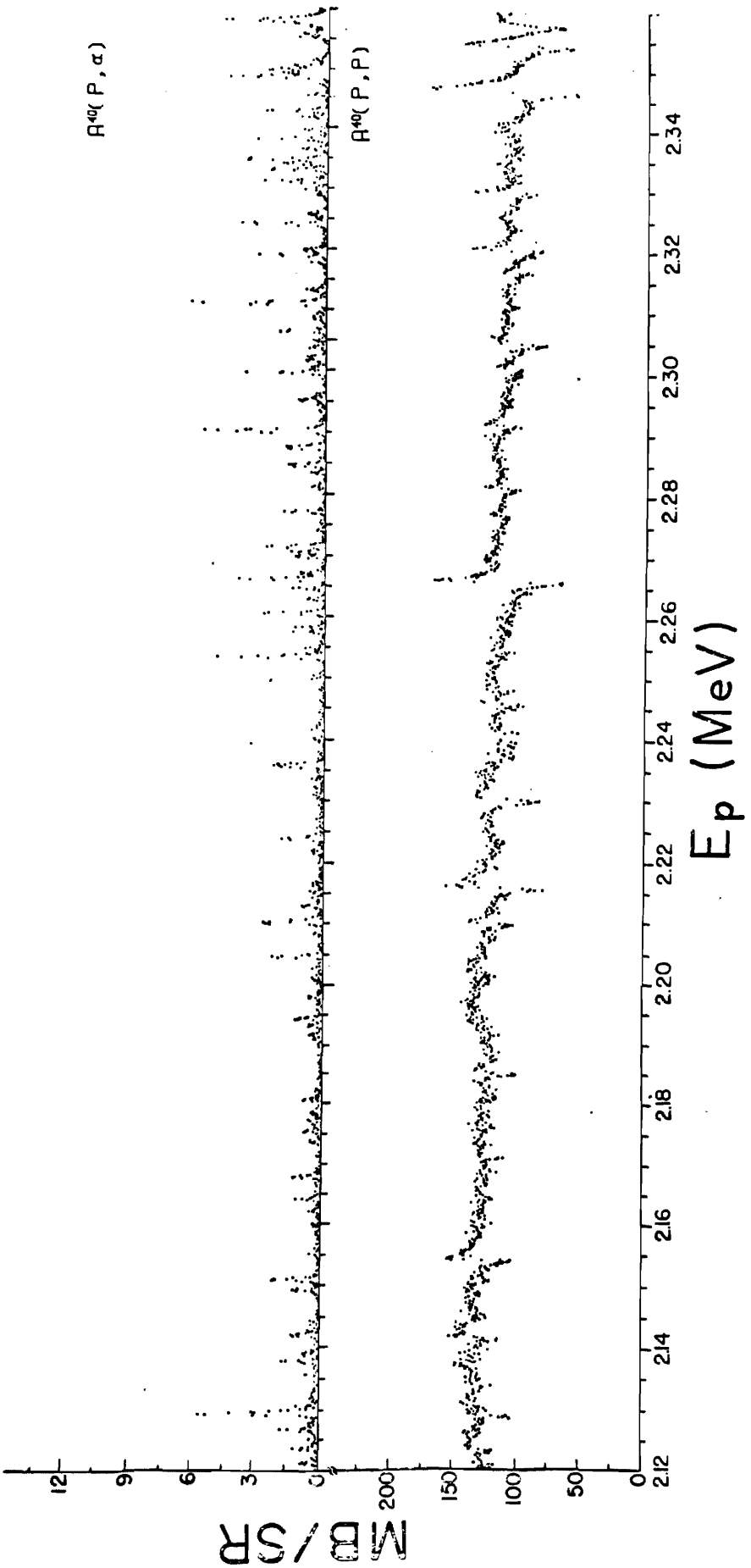
A40(P, α)
A40(P, P)
MB/SR
Ep (MeV)
12
9
6
3
0
200
150
100
50
0
2.12
2.14
2.16
2.18
2.20
2.22
2.24
2.26
2.28
2.30
2.32
2.34

Figure 13. Continuation of the data including $^{40}A(p,n)^{40}K$ total cross section data (mb) above neutron threshold. The 2.45 MeV analogue resonance is clearly visible as a region of increased structure near this energy.

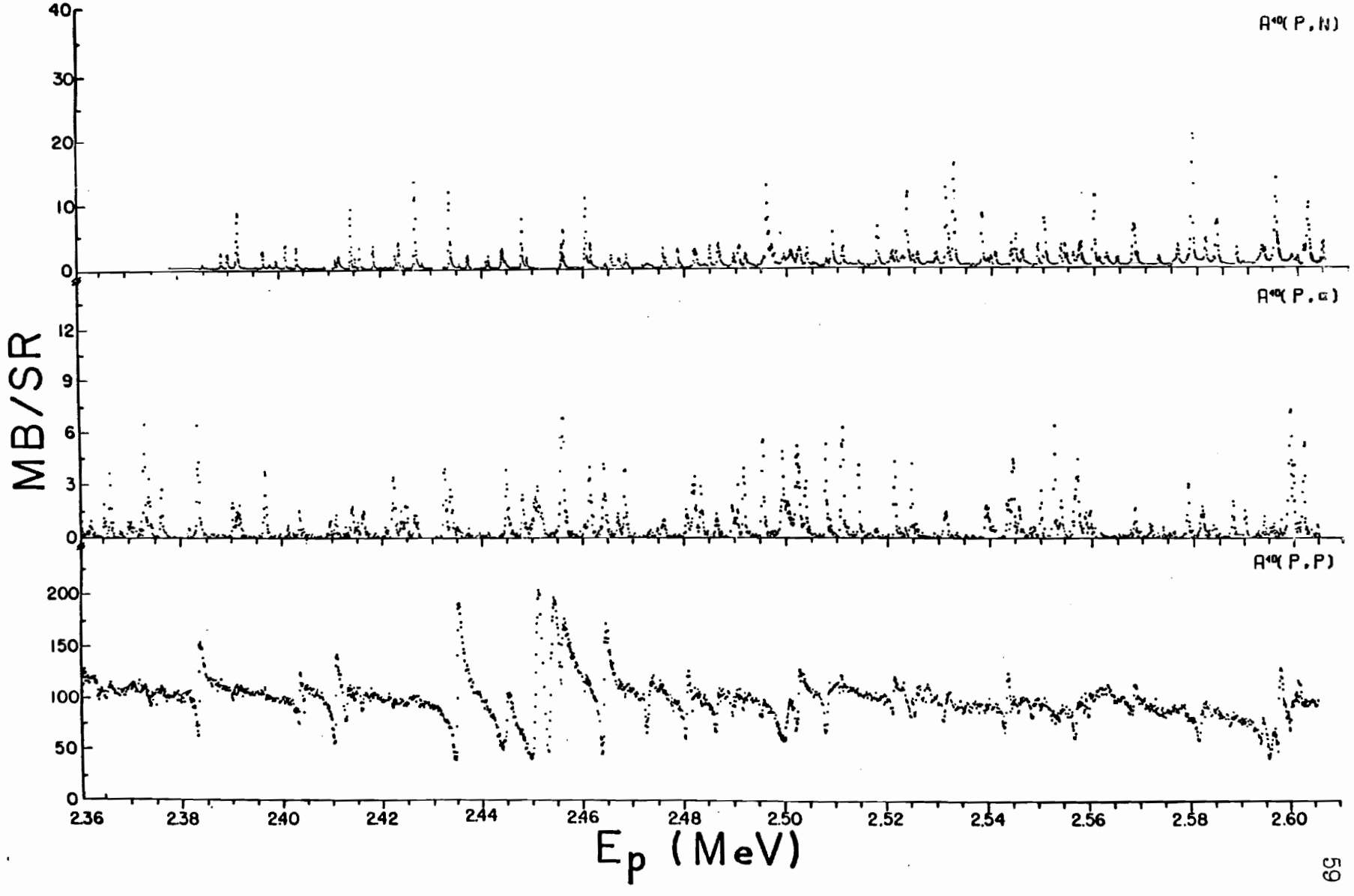
A40(P, N)
A40(P, α)
A40(P, P)
MB/SR
40
30
20
10
0
12
9
6
3
0
200
150
100
50
0
2.36
2.38
2.40
2.42
2.44
2.46
2.48
2.50
2.52
2.54
2.56
2.58
2.60
Ep (MeV)

KEYWORTH PhD 1968

& 40Ar + p

Table 1. Resonance Parameters

E_o (MeV)	J^π	Γ (eV)	Γ_p	Γ_α	Γ_n
1.6432	$1/2^+$	20	20	—	—
1.6489	$3/2^-$	6	5	1	—
1.6561	$3/2^-$	35	35	1	—
1.6711	$3/2^-$	25	25	—	—
1.6769	$1/2^-$	40	40	—	—
	$3/2^-$	20	20	—	—
1.7040	$1/2^-$	25	25	—	—
	$3/2^-$	15	15	—	—
1.7102	$1/2^-$	100	100	—	—
1.7150	$1/2^-$	50	50	—	—
	$3/2^-$	35	35	—	—
1.7310	$1/2^-$	32	30	2	—
	$3/2^-$	21	20	1	—
1.7332	$3/2^-$	60	60	—	—
1.7461	$1/2^-$	80	80	—	—
	$3/2^-$	50	50	—	—
1.7485	$1/2^-$	75	70	5	—
1.7664	$3/2^-$	20	20	—	—
1.7728	$1/2^-$	34	30	4	—

Table 1. (continued)

E_o (MeV)	J^π	(eV)	p	a	n
1.7956	$3/2^-$	100	100	1	—
1.8072	$1/2^-$	50	50	—	—
1.8108	$3/2^-$	40	40	1	—
1.8147	$3/2^-$	150	150	1	—
1.8219	$1/2^-$	23	18	5	—
	$3/2^-$	12	10	2	—
1.8294	$1/2^-$	60	60	—	—
	$3/2^-$	40	40	—	—
1.8330	$3/2^-$	46	45	1	—
1.8353	$3/2^-$	70	70	—	—
1.8419	$1/2^-$	100	100	—	—
	$3/2^-$	70	70	—	—
1.8491	$1/2^-$	357	350	7	—
1.8514	$3/2^-$	30	30	—	—
1.8597	$3/2^-$	800	800	4	—
1.8738	$3/2^-$	1250	1250	—	—
1.8762	$1/2^-$	60	60	—	—
	$3/2^-$	140	140	—	—
1.8770	$3/2^-$	450	450	1	—
1.8843	$3/2^-$	30	30	1	—

Table 1. (continued)

E_o (MeV)	J^π	(eV)	p	α	n
1.8941	$3/2^-$	70	70	1	—
1.8974	$3/2^-$	400	400	3	—
1.9017	$1/2^+$	20	15	5	—
1.9138	$1/2^+$	130	125	5	—
1.9149	$1/2^+$	19	15	4	—
1.9234	$1/2^-$	66	60	6	—
1.9252	$3/2^-$	52	50	2	—
1.9318	$1/2^-$	45	45	—	—
1.9581	$1/2^-$	62	60	2	—
1.9835	$1/2^-$	190	180	11	—
1.9906	$1/2^+$	12	12	—	—
	$3/2^-$	20	20	—	—
2.0069	$1/2^-$	50	50	—	—
2.0099	$1/2^+$	70	70	—	—
2.0338	$1/2^-$	53	50	3	—
2.0368	$1/2^+$	100	100	—	—
	$3/2^-$	175	175	—	—
2.0378	$3/2^-$	40	35	5	—
2.0450	$1/2^-$	23	20	3	—

Table 1. (continued)

E_o (MeV)	J^π	(eV)	p	α	n
2.0628	$1/2^-$	130	130	—	—
2.0826	$1/2^-$	150	150	2	—
2.0871	$3/2^-$	150	155	1	—
2.0990	$3/2^-$	70	70	1	—
2.1080	$1/2^-$	114	110	4	—
2.1211	$3/2^-$	21	20	1	—
2.1235	$1/2^+$	23	20	3	—
	$3/2^-$	36	35	1	—
2.1290	$3/2^-$	69	60	9	—
2.1456	$3/2^-$	70	70	—	—
2.1511	$1/2^-$	29	22	7	—
2.1543	$1/2^+$	60	60	—	—
2.1713	$1/2^-$	60	60	—	—
2.1762	$1/2^-$	50	50	—	—
2.1851	$1/2^-$	120	120	—	—
	$3/2^-$	70	70	—	—
2.2102	$1/2^+$	60	60	—	—
2.2160	$1/2^+$	110	110	—	—
2.2302	$1/2^-$	300	300	—	—
2.2462	$1/2^+$	50	50	—	—

Table 1. (continued)

E_o (MeV)	J^π	(eV)	p	a	n
2.2643	$3/2^-$	22	20	2	—
2.2662	$1/2^+$	210	210	—	—
2.2770	$1/2^+$	20	15	5	—
2.2815	$1/2^+$	42	40	2	—
2.2901	$3/2^+$	90	30	60	—
2.2914	$3/2^-$	30	30	—	—
2.3012	$1/2^+$	15	15	—	—
2.3048	$1/2^-$	220	220	1	—
2.3107	$3/2^+$	80	30	50	—
2.3166	$1/2^-$	70	70	—	—
2.3204	$1/2^+$	65	65	—	—
2.3258	$3/2^+$	31	30	1	—
2.3299	$1/2^+$	51	50	1	—
2.3466	$1/2^+$	275	275	—	—
2.3542	$1/2^+$	200	200	—	—
2.3575	$1/2^-$	830	830	—	—
2.3601	$1/2^-$	130	130	1	—
2.3739	$1/2^-$	65	55	10	—
2.3830	$1/2^+$	150	140	9	—

Table 1. (continued)

E_o (MeV)	J^π	(eV)	p	a	n
2.3901	$1/2^-$	40	35	5	—
2.4034	$1/2^+$	77	70	4	3
2.4042	$1/2^-$	100	100	1	—
2.4107	$1/2^+$	150	150	3	—
2.4127	$1/2^-$	250	250	1	—
2.4163	$1/2^-$	75	70	5	—
2.4349	$1/2^+$	600	600	—	—
2.4449	$3/2^-$	750	750	6	1
2.4507	$1/2^+$	1000	1000	13	—
2.4535	$1/2^+$	750	750	—	—
2.4558	$3/2^-$	150	140	9	2
2.4605	$1/2^-$	80	40	5	35
2.4642	$1/2^+$	360	340	18	—
2.4727	$1/2^-$	410	410	—	1
2.4804	$1/2^+$	175	170	6	—
	$3/2^-$	270	270	2	—
2.4818	$1/2^-$	100	90	11	—
2.4863	$3/2^-$	230	225	6	—
2.4918	$1/2^-$	80	40	25	15
2.4955	$3/2^-$	45	25	15	5

Table 1. (continued)

E_o (MeV)	J^π	(eV)	p	α	n
2.5000	$1/2^-$	1400	1400	9	—
2.5021	$3/2^-$	190	175	7	6
2.5111	$1/2^+$	200	45	125	30
2.5210	$1/2^+$	70	50	15	5
2.5314	$3/2^-$	35	25	4	6
2.5446	$1/2^-$	200	40	100	60
2.5446	$3/2^-$	70	20	30	20
2.5459	$1/2^-$	60	35	12	13
	$3/2^-$	35	25	5	5
2.5489	$1/2^-$	100	90	4	6
2.5570	$1/2^-$	250	180	53	15
2.5590	$1/2^+$	30	25	5	—
2.5599	$1/2^-$	170	55	15	100
2.5686	$1/2^+$	45	40	5	—
2.5816	$3/2^-$	270	250	13	4
2.5878	$1/2^-$	50	30	10	10
2.5938	$1/2^+$	43	40	3	—
2.5956	$1/2^-$	650	650	2	—
2.5975	$1/2^+$	175	175	1	—

Table 1. (continued)

E_o (MeV)	J^π	(eV)	p	α	n
2.5998	$1/2^-$	140	90	47	—
2.6020	$3/2^+$	125	75	35	15

energies cover the range 9.93 to 10.34 MeV excitation in the compound nucleus ^{41}K. Although the ^{7}Li calibration is potentially accurate to ±0.5 keV, the cumulative effect of joining many different data runs introduces an absolute energy uncertainty of up to ±2 keV. Relative energies of resonances are accurate to 0.3 keV or better, in a particular run. The proton widths Γ_p in Table 1, derived as discussed below, range in precision from about 10% on the widest resonances to about 40% on the very weakest ones; the reaction partial widths, estimated from area analysis, are probably accurate to about 30%. The partial width for proton capture has been neglected in this analysis.

Wherever the resonances were separated by a sufficient energy to permit their comparison with a single-level Breit-Wigner, a computer program based on eq. (A.1) was used, as discussed in Appendix A. The difference between correct non-resonant phase shifts and point-charge scattering phase shifts was neglected since, for ^{40}A at these energies, the differences were less than 2^{o}. The actual method employed was to compare the normalized data to a theoretical curve generated by an IBM-7072 computer using an on-line plotter. The shape fits usually gave unambiguous assignments of spin, parity and natural widths of the strong resonances. However, when the natural width of a resonance is much smaller than the experimental resolution, the distinction in shape tends to be lost, especially between a $1/2^{-}$ and $3/2^{-}$ level. Due to the minimal thickness of the target, a normalized Gaussian is expected to be a good

approximation to the resolution function and was included as a resolution smear in the fits. The accuracy with which isolated resonances are fit is illustrated in Fig. 14.

To treat the more complicated cases where the levels are too close together to be treated by the single-level formula, an approximate multi-level code, written by G. C. Kyker, Jr., based on eq. (A.10), was used. In this formula, consideration is restricted to zero-spin target nuclei, point charge non-resonant phase shifts and it was assumed that elastic scattering is the only open channel. Below neutron threshold (2.344 MeV) this is certainly a reasonable assumption. Above neutron threshold, most of the resonances seen in the elastic scattering cross section were apparently due to s-wave protons so that a coincident neutron must be f-wave. The penetrability for an f-wave neutron of this energy is sufficiently low ($\sim 1.5 \times 10^{-4}$ at $E_p = 2.5$ MeV) that we see few coincident neutron and proton resonances, in agreement with the assumption made for these cases.

The ability of this method to fit complex regions of the data is demonstrated in Fig. 15. Using these two programs, the absolute differential cross section for the proton data was determined and thus, also for the (p, α) data.

After assignment of spins and parities to the observed fine structure in the elastically scattered proton data, it was observed that the large majority of the resonances in the lower region at 1.87 MeV

Figure 14. Some Computer-Generated Single-Level Fits. The solid curves are theoretical fits using the indicated parameters.

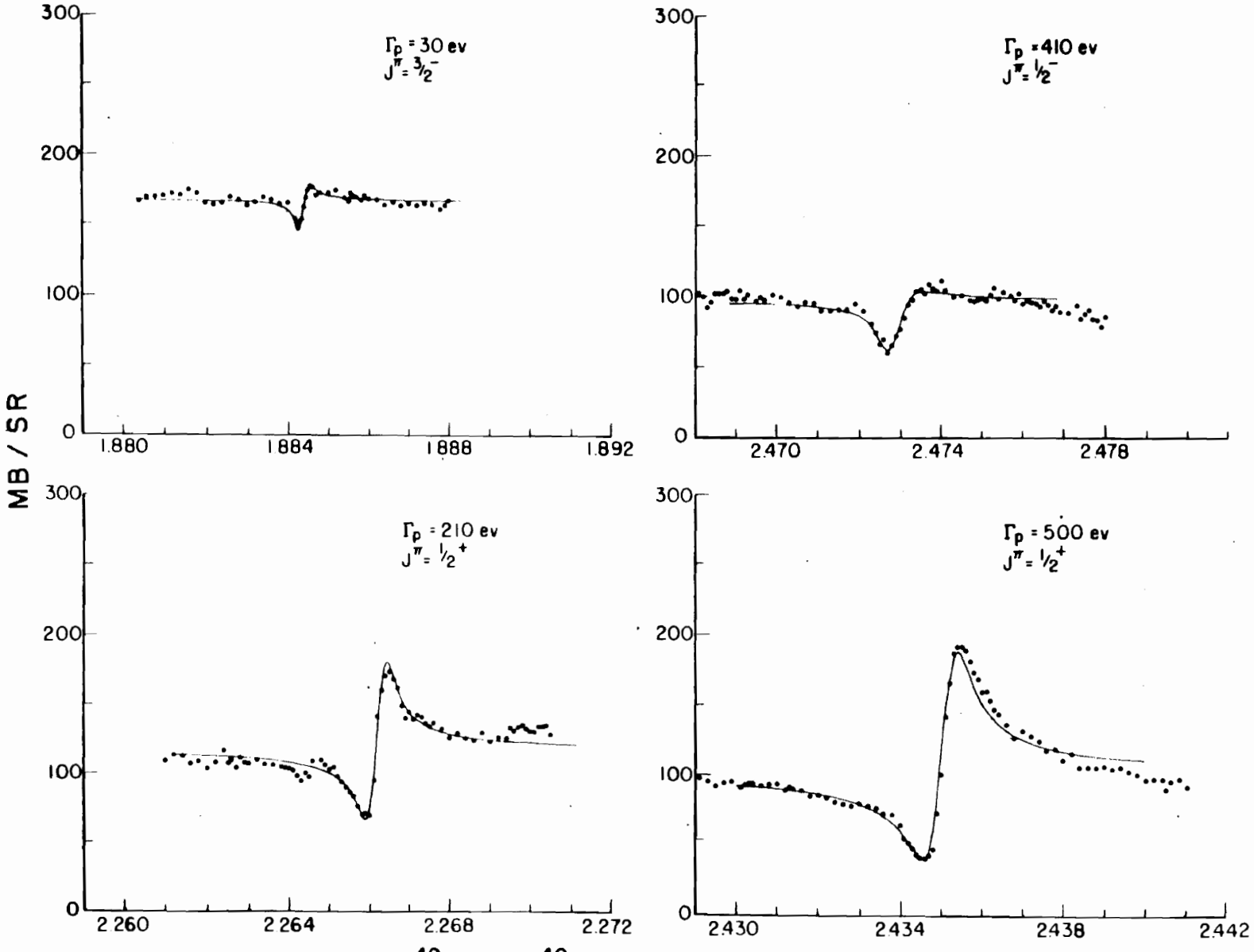

$A^{40}(p,p)A^{40}$ SINGLE LEVEL FITS

Figure 15. A Sample Multi-Level Fit to a Portion of the $^{40}A(p,p)$ Data Near the $3/2^-$ Analogue Resonance. Resonance parameters are determined by trial and error comparison with the data.

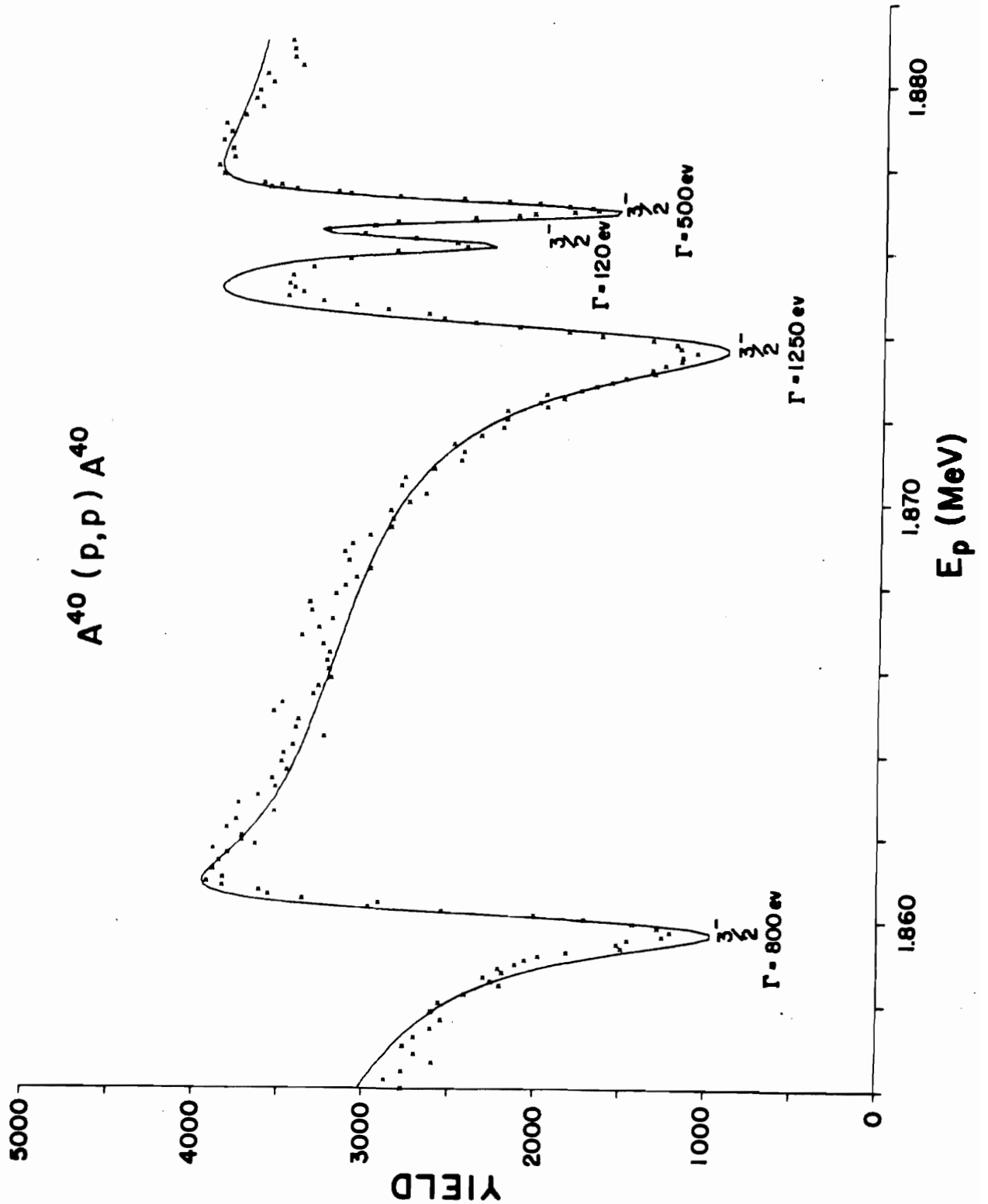
A40 (p,p) A40
YIELD
5000
4000
3000
2000
1000
0
1.860
1.870
1.880
Ep (MeV)
3/2-
Γ = 800 ev
3/2-
Γ = 1250 ev
3/2-
Γ = 120 ev
3/2-
Γ = 500 ev

were best fit with $J^{\pi} = 3/2^{-}$ and those in the upper region with $1/2^{+}$. This agrees with the assignments from (d, p) stripping[26] of $\ell = 1$ and $\ell = 0$, respectively, to the fourth and sixth excited states of ^{41}A. The reaction diagram (Fig. 16) shows that neutrons from the $1/2^{+}$ level would have a most probable ℓ-value of 3, whereas α-particles would have $\ell = 2$ for the $J^{\pi} = 1/2^{+}$ region and $\ell = 1$ for the lower region. Thus, through consideration of penetrabilities, the majority of the strength in these two regions would be expected to be in the elastic proton channel, as observed.

Recent measurements by Winkler et al.[27] of two narrow resonances in the $^{40}A(p, p)$ and $^{40}A(p, \alpha)$ cross sections near 1.1 MeV with very precise absolute energy determination (±300 eV) have suggested the use of these resonances as a check of our absolute energy calibration and as a possibility of seeing the analogue of the second excited state of ^{41}A. Between incident proton energies of 1.05 and 1.12 MeV, counting for about 12000 counts, only the two levels reported in Ref. 27 were seen (Fig. 17). Although the single angle measurement did not permit assignment of a definite J^{π}, the resonances have been fit using the spin and parities assigned in Ref. 27 with the aid of their measurements at 90°, 125° and 141°. These assignments were $J^{\pi} = 1/2^{-}$ or $3/2^{-}$ for the level at 1.086 MeV and $J^{\pi} = 3/2^{-}$ for the level at 1.102 MeV. In addition, Γ_p/Γ was determined as 0.7 in the previous measurements due to an unusually large γ-width. Using $J^{\pi} = 3/2^{-}$ for both cases, in accordance with the assignment[26] for the second excited state of ^{41}A, partial widths of

Figure 16. Energy Diagram for the System $^{40}A + p$. The (p, p') and (p, γ) channels were unobserved in the present experiment. The scale on the right shows excitation energy of the compound nucleus ^{41}K in MeV.

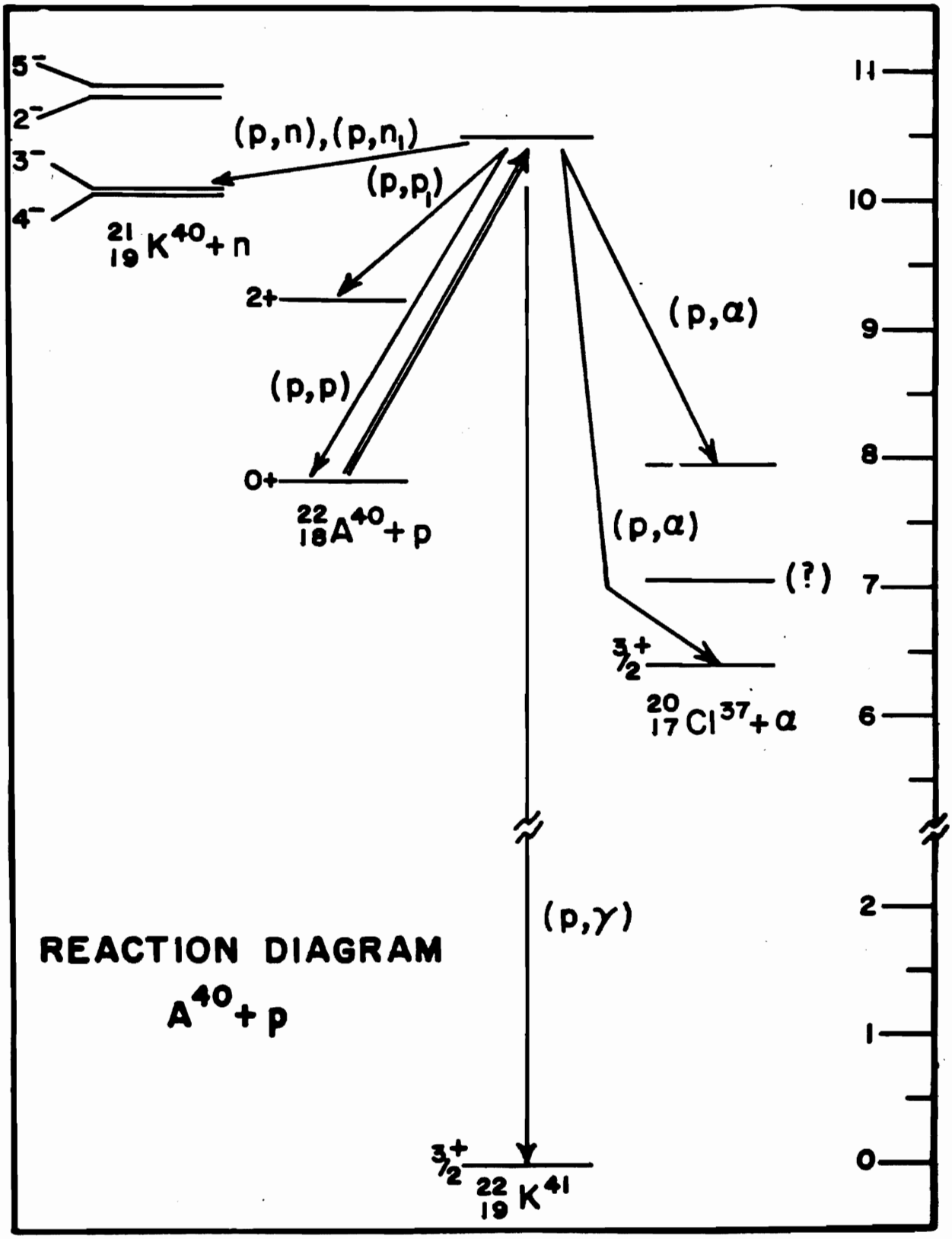
5⁻
2⁻
3⁻
4⁻
$^{21}_{19}K^{40}+n$
(p,n),(p,n₁)
(p,p₁)
2+
(p,p)
0+
$^{22}_{18}A^{40}+p$
(p,α)
(p,α)
(?)
$\frac{3}{2}^+$
$^{20}_{17}Cl^{37}+\alpha$
(p,γ)
$\frac{3}{2}^+$
$^{22}_{19}K^{41}$
REACTION DIAGRAM
$A^{40}+p$
11
10
9
8
7
6
2
1
0

Figure 17. The $^{40}A(p,p)^{40}A$ Data Near 1.1 MeV Showing a Possible Analogue Resonance Region. The $^{40}A(p,\gamma)^{41}K$ data of Ref. 27 show several other resonances in this region.

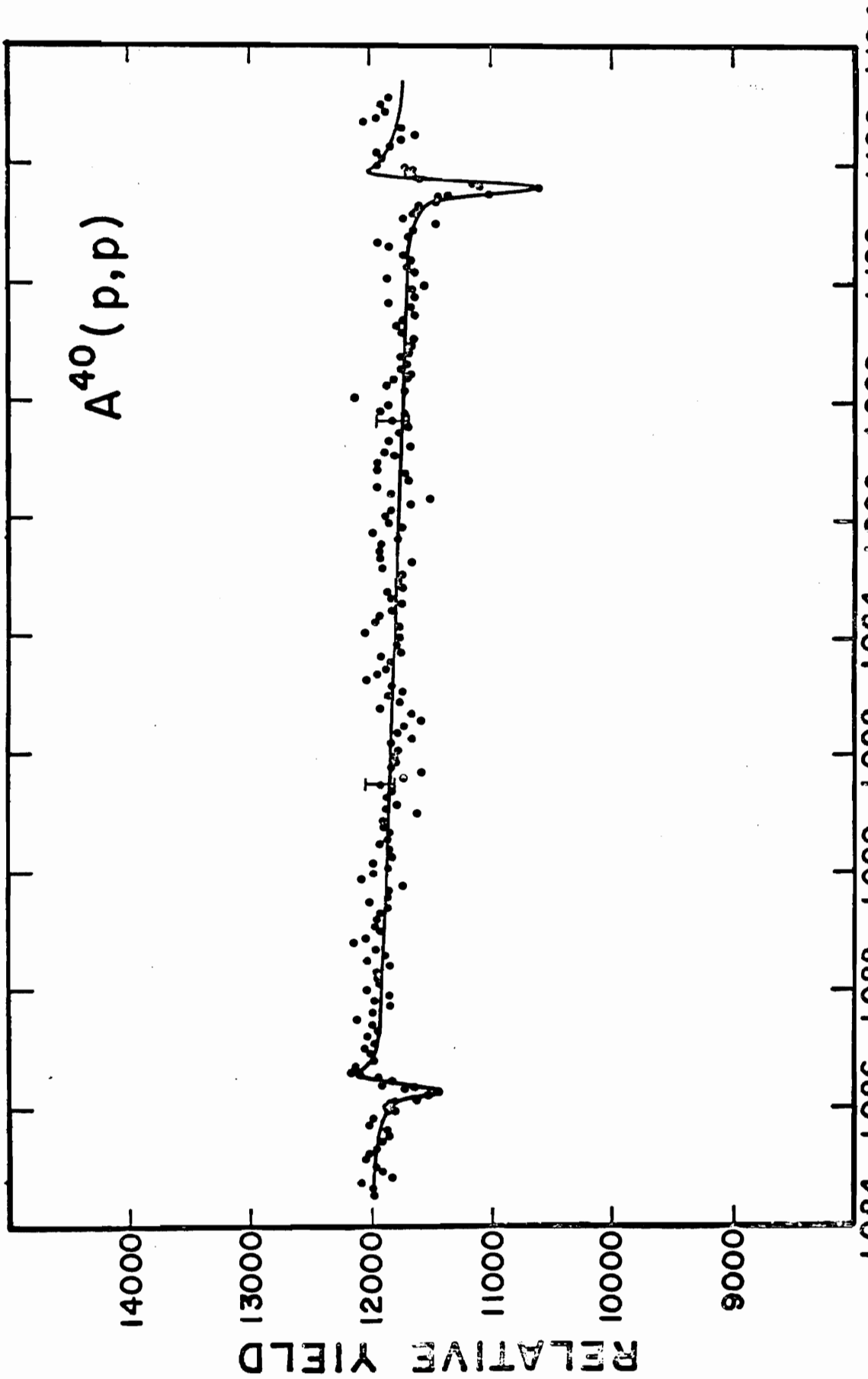
A40(p,p)
RELATIVE YIELD
14000
13000
12000
11000
10000
9000
1.084
1.086
1.088
1.090
1.092
1.094
1.096
1.098
1.100
1.102
1.104
Ep (MeV)
I
II
III

Γ_p = 8 eV for the lower level and Γ_p = 18 eV for the higher were obtained from fitting the present data. This gives a combined reduced width of 100 keV, in qualitative agreement with the reduced width of the second excited state of ^{41}A. However, since the (p, γ) measurements[27] indicated several other levels in this region, it is likely that there are levels whose widths are too narrow to be observed in elastic scattering with the available resolution or for which $\Gamma_p \ll \Gamma$.

After having corrected the energy to a previously measured ^{7}Li(p,n)^{7}Be threshold, the present work agrees within 300 eV of the absolute energy assignment of Ref. 27.

The α-particle and neutron partial widths presented in Table I were computed by area analysis. Since we know the spin of the proton entrance channel from the (p,p) analysis, the angular momentum of the outgoing neutron or α-particle can be determined from the reaction diagram (Fig. 16). Since the neutron data are from a 4π measurement, the area under a neutron resonance is simply

$$S_n = 2\pi^2 \lambda^2 g_J \frac{\Gamma_p \Gamma_n}{\Gamma} \qquad (4.1)$$

from integrating the Breit-Wigner formula. Similarly, for the α-particles, the area under a resonance is given by

$$S_\alpha = \frac{\pi \lambda^2 g_J}{A_J} \frac{\Gamma_p \Gamma_\alpha}{\Gamma} \qquad (4.2)$$

where A_J contains the angular dependence, since this is no longer a 4π measurement. Only 19 neutron resonances were found to have a measur-

able proton width, thus permitting this method of analysis, but 79 α-particle resonances were analysed. In agreement with the previously mentioned assumptions regarding the fitting procedure for (p,p) resonances, very few of the neutron and α-particle widths are appreciable as compared to the proton width. However, this is not necessarily true of the reduced widths.

The absolute cross sections for the (p,n) data were determined by integrating the data shown here and comparing with absolute measurements made with a much thicker target at the University of Kentucky.[28]

B. ^{23}Na

The ^{22}Ne experiment was conducted in two separate stages. Initially, the excitation function for elastic scattering was measured at 135° in the prototype target chamber over the entire range of energy readily obtainable with the 3 MeV accelerator, 0.8 to 3.1 MeV. Whereas this first measurement was useful for indicating the locations of resonances, it was immediately evident that more spectroscopic information, such as spins, parities and widths, could not be obtained from a measurement at one angle. There appeared to be two major reasons why observation at only one angle, sufficient in the ^{40}A experiment, was inadequate here. Resonances with $\ell = 2$, which predominate in the compound system ^{23}Na but which do not appear in ^{41}K in the regions measured,

interfere with potential scattering less markedly than do resonances with lower ℓ. Similarly, it is more difficult to distinguish between $J = \ell + 1/2$ and $J = \ell - 1/2$ for $\ell = 2$. Secondly, the average width of the resonances above a bombarding energy of 2 MeV is quite large compared to that in ^{41}K and the resulting structure is much more complex.

Accordingly, the measurement was repeated, using the improved target chamber, with detectors at 90, 105, 120, 135, 150 and 160°. Due to limitations imposed by lack of available electronic equipment, a maximum of four particles could be counted at one time. Therefore, the continuous excitation function for elastically scattered protons was measured simultaneously at 90, 120 and 160° and then repeated in the vicinity of resonances at the three remaining angles. Finally, inelastically scattered protons were observed at 150, 120 and 90° simultaneously with elastic protons at 150°. The elastic proton measurement was repeated to ensure precise energy alignment between the two excitation functions for elastic and inelastic protons. Although the inelastic proton measurements extend from 1.8 to 3.1 MeV, penetration effects for scattering to the first excited state of ^{22}Ne at 1.27 MeV made observation of these particles below 2.0 MeV essentially useless.

Selected portions of the data are shown in Figs. 18-22. Although the energy steps taken during the measurements were usually 200 eV away from resonances and 50 eV on resonances, the data in Figs. 19-22 show only points at intervals of 1 keV, except where the resonances

Figure 18. The $^{22}Ne(p,p)^{22}Ne$ Data Below 2.1 MeV. Only the resonances are included. The energy scale is the same for all resonances shown except for the wide anomaly at $E_p = 1.967$ MeV, for which only every tenth data point is indicated. Although only the 160° data is included here, these resonances were measured at six angles. The solid lines do not represent a fit, but serve as visual aids.

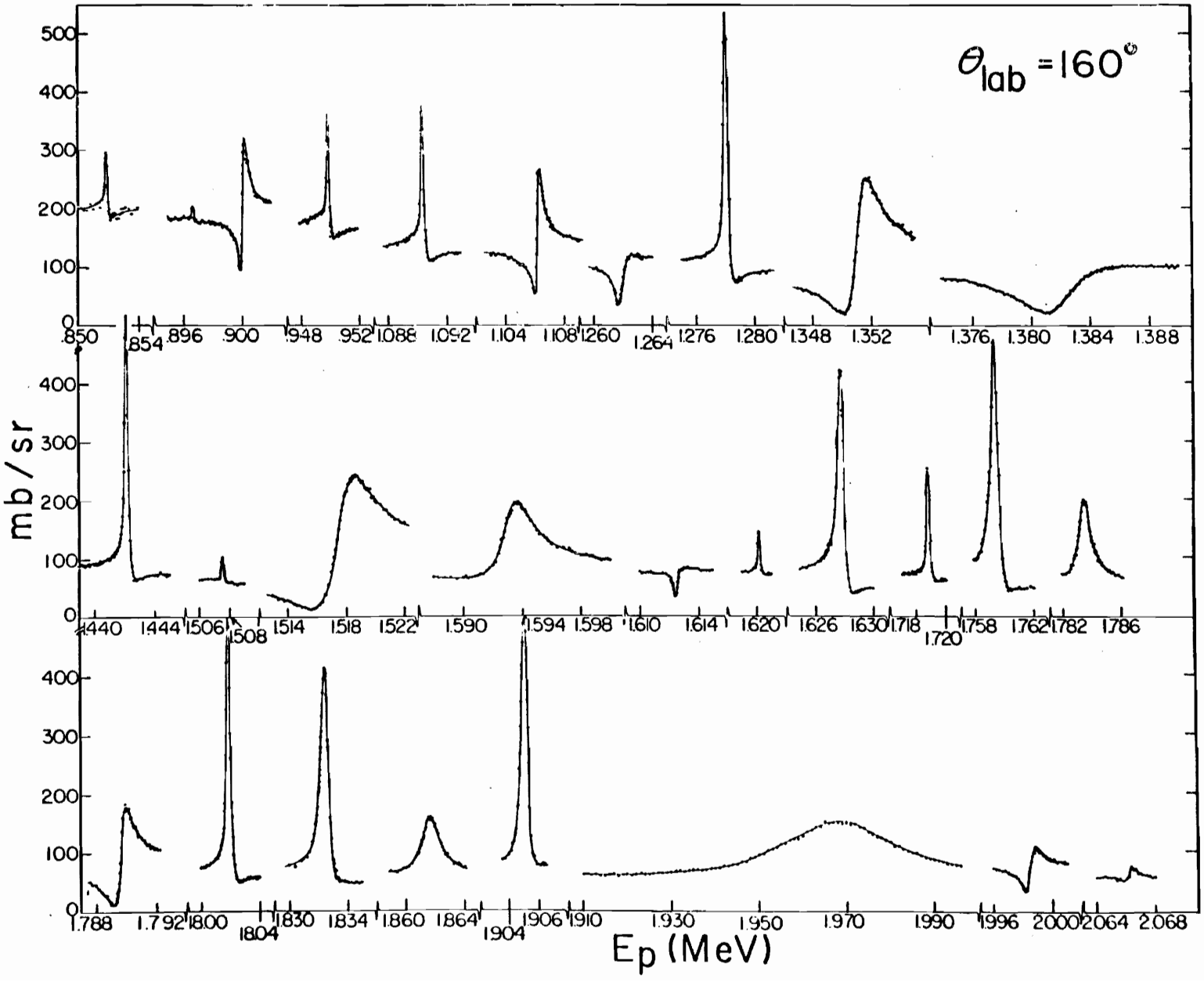
$\theta_{lab} = 160°$
mb / sr
Ep (MeV)

Figure 19. Continuation of the (p, p) Data. Except on narrow resonances, only every fifth data point is indicated. The data immediately preceding those in the figure are included in the multilevel fit of Fig. 24. A portion of the $3/2^+$ analogue state is included here. The complexity of the region above 2.1 MeV is in marked contrast to that shown in Fig. 18.

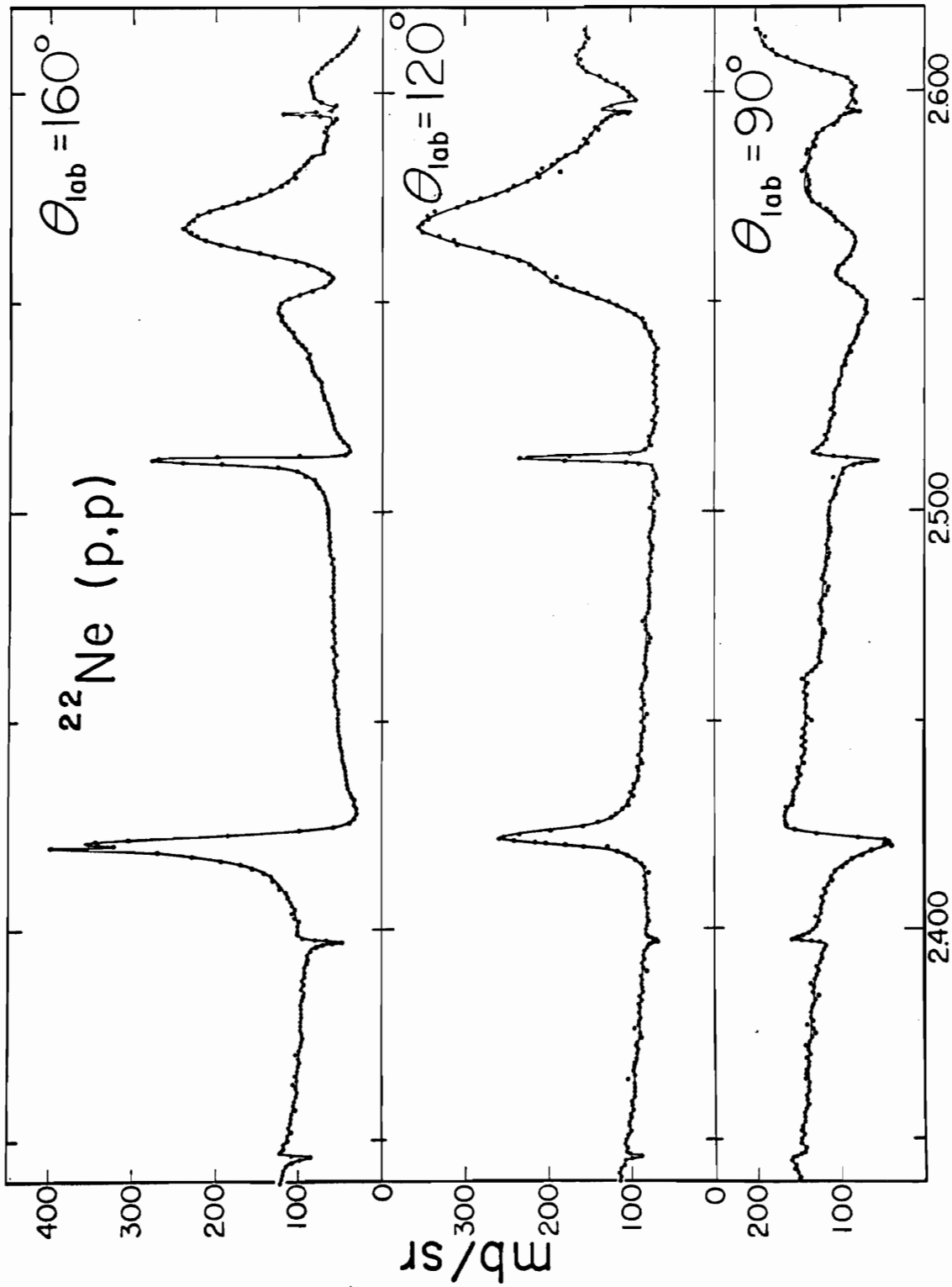
^{22}Ne (p,p)
θ_{lab}=160°
θ_{lab}=120°
θ_{lab}=90°
mb/sr
400
300
200
100
0
200
100
2.400
2.500
2.600
Ep (MeV)

Figure 20. Continuation of the (p, p) Data.

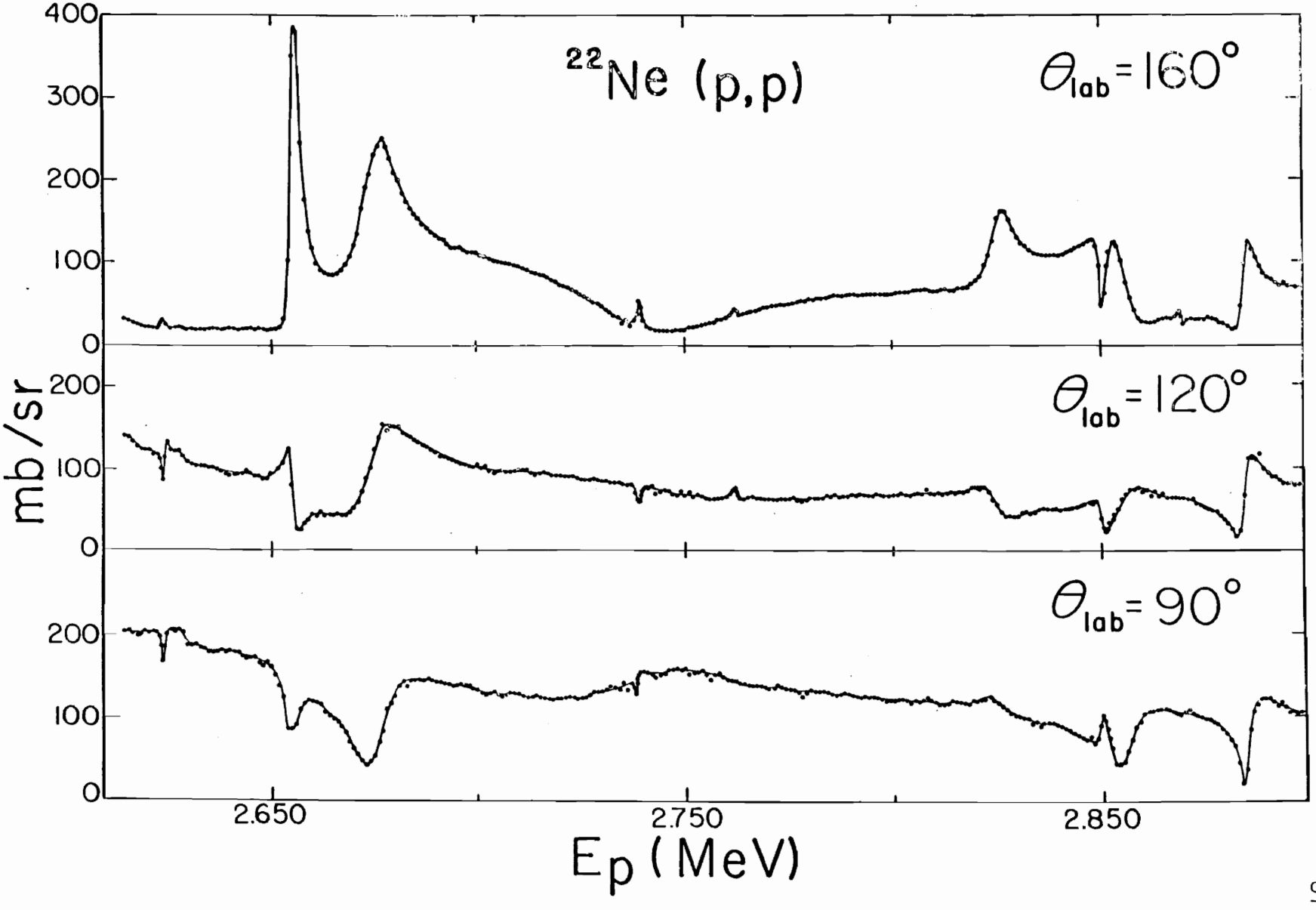
^{22}Ne (p,p)
θ_{lab} = 160°
θ_{lab} = 120°
θ_{lab} = 90°
400
300
200
100
0
200
100
0
200
100
0
mb/sr
2.650
2.750
2.850
Ep (MeV)

Figure 21. Continuation of the (p, p) Data.

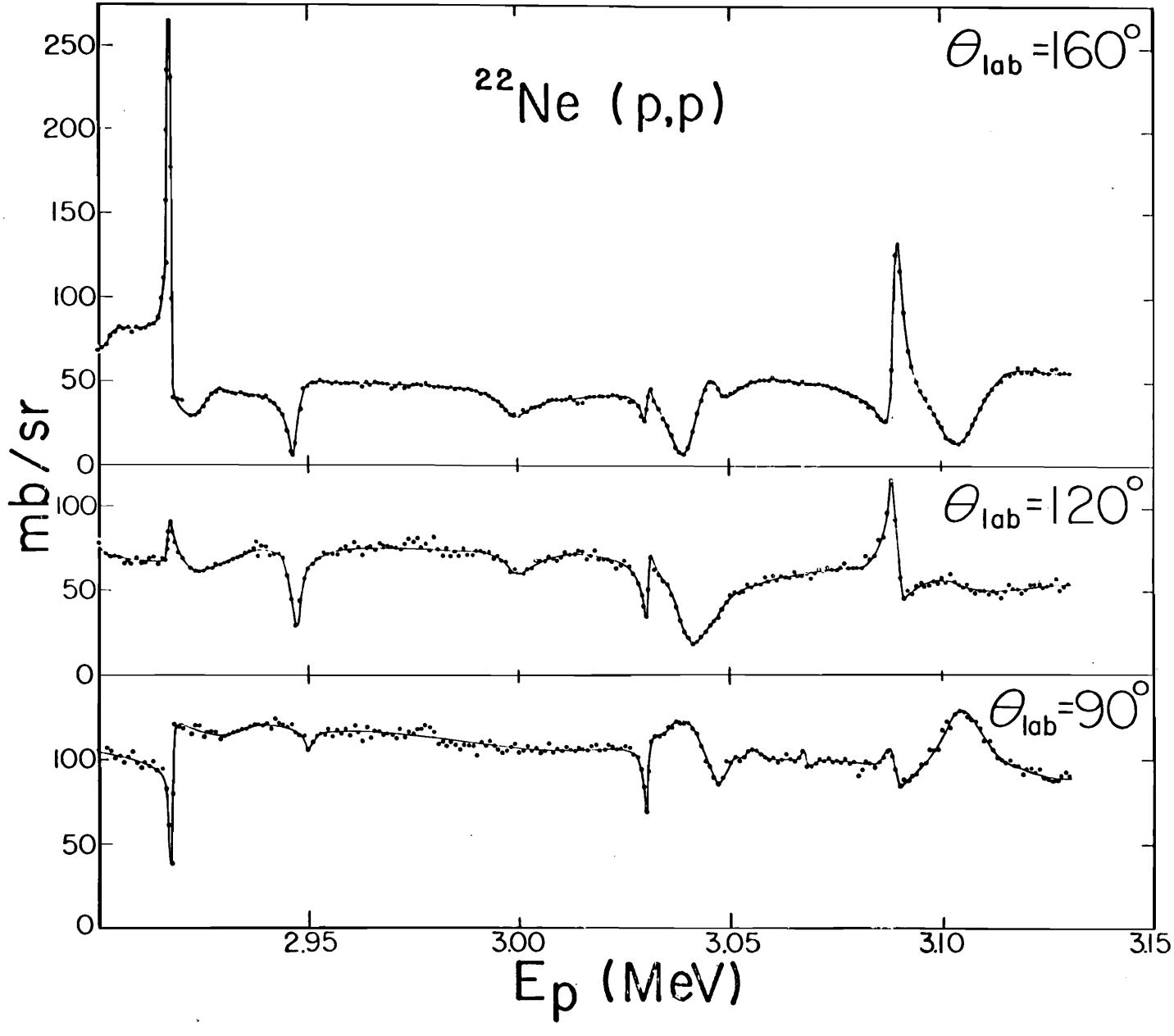
^{22}Ne (p,p)
θ_{lab}=160°
θ_{lab}=120°
θ_{lab}=90°
mb/sr
250
200
150
100
50
0
100
50
0
100
50
0
2.95
3.00
3.05
3.10
3.15
Ep (MeV)

Figure 22. The $^{22}Ne(p,p')^{22}Ne^*$ Data at 120°. The data shown here include only every fifth data point, except on narrow resonances. These data were also measured at 150 and 90°.

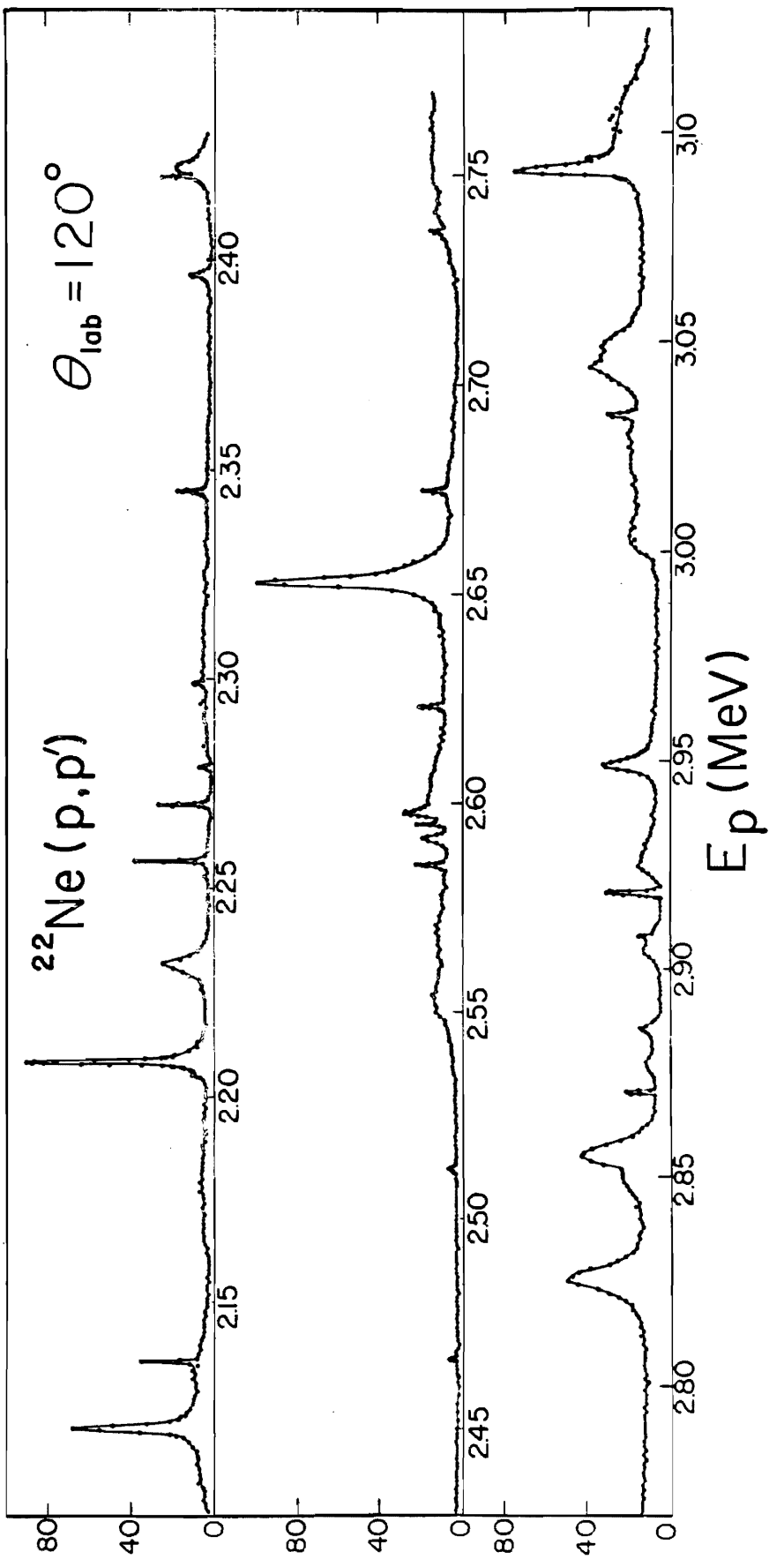
^{22}Ne(p,p')
$\theta_{lab} = 120°$
mb/sr
E_p (MeV)
80
40
0
2.15
2.20
2.25
2.30
2.35
2.40
2.45
2.50
2.55
2.60
2.65
2.70
2.75
2.80
2.85
2.90
2.95
3.00
3.05
3.10

are so narrow as to require more detail. The necessity for this simplification is evident in the fact that the actual measurements from 2.1 to 3.1 MeV contain about 10000 data points at each angle of observation. The lines through the data are not theoretical fits, but are simply drawn as a visual aid.

Due to the large beam intensities used and the increased running time realized with the improved target chamber, only 40 runs were required to complete the measurements. In addition, because yield changes between successive runs were usually negligible, little time was spent overlapping. As in the ^{40}A experiment, absolute energy calibration was obtained by measurement of the $^{7}Li(p,n)^{7}Be$ threshold.

Table 2 gives the results of the analysis of all resonances observed and covers the range of excitation in the compound nucleus ^{23}Na of 9.56 to 11.78 MeV. Because resonances were frequently not within suitable range for overlapping of successive runs or because the overlapped resonances were too wide for precise relative energy calibration, an absolute energy uncertainty of up to ± 4 keV results from joining the separate data runs. This energy uncertainty could have been greatly reduced by taking a $Li(p,n)^{7}Be$ threshold each day, but this was impractical.

The difficulties encountered in generating the fits required to give the contents of Table 2 were manifold, and their brief description will perhaps enhance interpretation of those quantities. As discussed in

KEYWORTH PhD 1968

$^{22}Ne + p$

Table 2. Resonance Parameters

E_o (MeV)	J^π	Γ (eV)	Γ_p	$\Gamma_{p'}$
0.8519	$3/2^+$	6	6	
	$5/2^+$	4	4	
0.9001	$1/2^+$	105	105	
0.9500	$5/2^+$	18	18	
	$3/2^+$	29	29	
1.0905	$3/2^+$	47	47	
1.1063	$1/2^+$	150	150	
1.2619	$1/2^-$	475	475	
1.2782	$5/2^+$	69	69	
1.3513	$1/2^+$	1270	1270	
1.3809	$1/2^-$	4200	4200	
1.4422	$5/2^+$	65	65	
1.5080	$3/2^+$	6	6	
	$5/2^+$	4	4	
1.5178	$1/2^+$	2450	2450	
1.5930	$3/2^-$	2000	2000	
1.6125	$1/2^-$	190	190	
1.6202	$3/2^+$	14	14	
	$5/2^+$	8	8	

Table 2 (continued)

E_o (MeV)	J^π	Γ (eV)	Γ_p	$\Gamma_{p'}$
1.6279	$3/2^+$	210	210	
1.7189	$5/2^+$	25	25	
1.7595	$3/2^+$	470	400	70
1.7834	$3/2^-$	920	880	40
1.7898	$1/2^+$	560	560	
1.8019	$5/2^+$	100	100	
1.8325	$5/2^+$	540	380	160
1.8615	$3/2^-$	1100	1010	90
1.9051	$5/2^+$	425	275	150
	$3/2^+$	425	360	65
1.9670	$3/2^-$	23000	22000	1000
1.99845	$3/2^-$	400	340	60
2.0662	$3/2^+$	< 5		
	$5/2^+$	< 5		
2.1212	$3/2^+$	1700	1000	700
2.1220	$3/2^-$	26000	25000	1000
2.1366	$3/2^+$	100	30	70
	$5/2^+$	100	20	80
2.1740	$3/2^-$	21000	20000	1000

Table 2 (continued)

E_o (MeV)	J^π	Γ (eV)	Γ_p	$\Gamma_{p'}$
2.2060	$1/2^-$	53	3	50
2.2092	$1/2^-$	2850	2500	350
2.2095	$5/2^+$	900	200	700
2.2196	$1/2^+$	55	5	50
2.2334	$3/2^+$	3500	3000	500
2.2536	$1/2^+$	5200	5000	200
2.2578	$7/2^-$	65	15	50
2.2771	$5/2^+$	400	150	250
	$3/2^+$	400	250	150
2.2800	$3/2^+$	18	3	15
2.2850	$3/2^-$	6000	5800	200
2.2990	$1/2^+$	20600	20000	600
2.3000	$3/2^+$	60	10	50
2.3462	$1/2^+$	500	200	300
2.3974	$1/2^-$	800	500	300
2.4201	$5/2^+$	135	25	110
2.4218	$3/2^+$	4100	2450	650
2.5128	$3/2^+$	800	700	100
2.5550	$3/2^-$	12200	12000	200

Table 2 (continued)

E_o (MeV)	J^π	Γ (eV)	Γ_p	$\Gamma_{p'}$
2.5670	$3/2^+$	20000	19500	500
2.5852	$3/2^-$	600	120	480
2.5920	$3/2^+$	1750	250	1500
2.5954	$3/2^+$	500	150	350
2.5986	$3/2^+$	4000	2000	2000
2.6047	$1/2^+$	11000	10000	1000
2.6230	$3/2^+$	300	50	250
2.6500	$1/2^-$	80000	75000	5000
2.6555	$5/2^+$	4000	2000	2000
2.6560	$3/2^-$	2000	1500	500
2.6573	$3/2^+$	750	150	600
2.6730	$1/2^-$	4000	3980	20
2.6770	$1/2^+$	13500	13000	500
2.7510	$1/2^-$	35000	27000	8000
2.8250	$7/2^-$	5500	900	4600
2.8500	$5/2^+$	3050	550	2500
2.8555	$5/2^+$	6900	1700	5200
2.8695	$5/2^+$	130	40	90
2.8850	$1/2^+$	3100	2300	800

Table 2 (continued)

E_o (MeV)	J^π	Γ (eV)	Γ_p	$\Gamma_{p'}$
2.9176	$5/2^+$	600	350	250
2.9465	$3/2^-$	3200	1000	2200
3.0010	$1/2^-$	14000	2000	12000
	$3/2^-$	9800	800	9000
3.0300	$1/2^+$	1900	500	1400
3.0395	$3/2^-$	7000	3000	4000
3.0474	$5/2^+$	3200	200	3000
3.0885	$7/2^-$	2300	700	1600
3.1060	$1/2^-$	15000	13000	2000

the Appendix, hard sphere phase shifts up to $\ell = 4$ were included in the fitting programs used in the ^{22}Ne experiment to give a reasonable approximation to nuclear potential scattering. This, however, introduces a strong dependence, both in the resonance shapes and in the magnitude of the cross section generated, upon the choice of nuclear radius. To minimize this uncertainty, fits were made to several isolated resonances with $J^{\pi} = 1/2^{+}$ for many different values of R_o. In this manner, the value $R_o = 1.25$ f. was selected. Below 2.1 MeV, the resonances are generally well isolated and a single level formula was utilized. The computer code (GALAHAD) was allowed to search over E_o, Γ, Γ_p/Γ and Δ, the width of the resolution function, to arrive at the best fit, in the least squares sense. The program was run independently for each of the six angles measured and the results checked for consistency. The calculation was also done for each value of J^{π} which was not immediately excluded by visual examination. An example of this method is shown in the fits in Fig. 23. Here, $\Gamma_p/\Gamma = 1$ and the resoance obviously has $\ell = 2$. Evidently, either value of $J^{\pi} = 5/2^{+}$ or $3/2^{+}$ would be suitable with a measurement at only one angle since all the fits are good. However, as the figure shows, the values of the parameters which the program selected are consistent at all three angles only for $J^{\pi} = 5/2^{+}$.

For such isolated resonances, the precision of the value for Γ_p given in Table 2 is about 10%, except for those few anomalies whose widths are very small compared to the width of the resolution function, where the

Figure 23. Single Level Fits at Three Angles to a $^{22}Ne(p,p)^{22}Ne$ Resonance for J^{π} Value of Both $3/2^{+}$ and $5/2^{+}$. Although each fit is reasonably good, the parameters required to produce the fits are consistent only for $J^{\pi} = 5/2^{+}$.

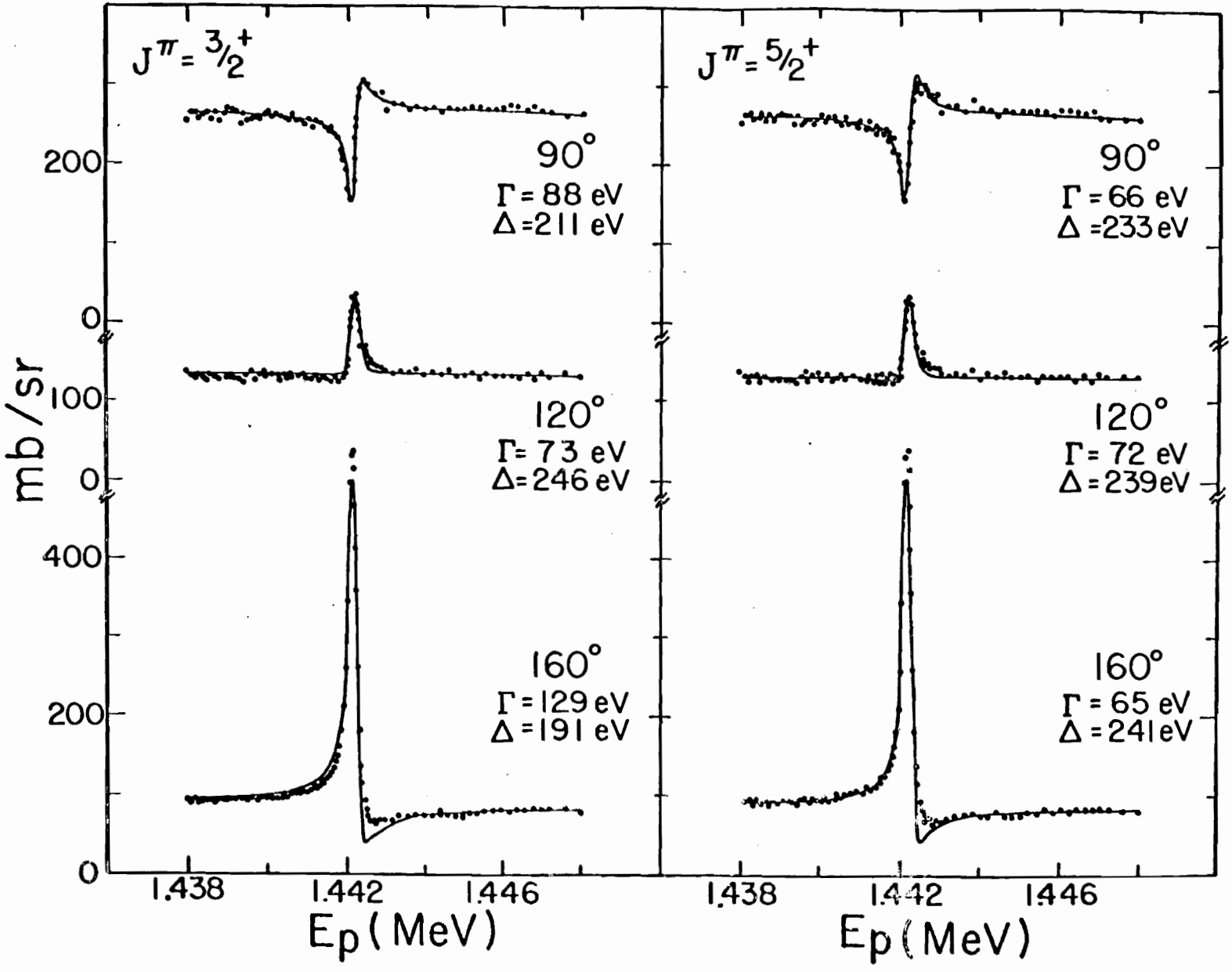
$J^\pi = 3/2^+$
90°
Γ = 88 eV
Δ = 211 eV
120°
Γ = 73 eV
Δ = 246 eV
160°
Γ = 129 eV
Δ = 191 eV
$J^\pi = 5/2^+$
90°
Γ = 66 eV
Δ = 233 eV
120°
Γ = 72 eV
Δ = 239 eV
160°
Γ = 65 eV
Δ = 241 eV
mb/sr
200
0
100
0
400
200
0
1.438
1.442
1.446
Ep (MeV)
1.438
1.442
1.446
Ep (MeV)

error in the proton partial width may be as great as 50%. This uncertainty is introduced because the effect of varying Γ_p/Γ, for very narrow resonances, is similar to that produced by changing the resolution by a small amount. Spin assignments are considered unique except where two values are given in the table.

Above 2.1 MeV, however, there are few isolated resonances and a multi-level, multi-channel program (MULTI), written by D. L. Sellin, was used to fit the data. The region from 2.1 to 3.1 MeV was divided into five separate overlapping spans, each of which could be treated by the program. Since as many as twenty resonances were included in each fit and because the ℓ-dependence of the resonance shape, which is so characteristic for an isolated resonance, is destroyed by level-level interference in this region, as many as 150 attempts were required to fit a given span. Since each parameter change is made manually, each fit represents an extensive effort. In this more complicated region, good fits were first obtained for the elastic cross section and the same parameters were then used to generate the inelastically scattered proton cross section, as an additional check. The fact that the resonance parameters thus derived also resulted in good fits to the inelastic cross section substantiates their uniqueness.

In those regions where multi-level analysis was applied, we were surprised to discover that the uniqueness of the spin assignment resulting from a fit was at least as definite as in the cases of isolated

resonances. The precision of the partial widths is, however, less than in the single level cases, particularly for the inelastic proton widths. At higher energies, attempts to fit the inelastic proton cross section were hampered by a rather large off-resonance background. Very little of this background was experimentally introduced; that is, the spectrum from the solid state detector showed the inelastic proton peak to be well isolated. It was assumed that this background was largely the effect of far away levels and perhaps, to a much lesser degree, from Coulomb excitation.

A typical multi-level fit is shown for a region of particular interest, to be discussed later, in Fig. 24. Except where particular doubts arose, multi-level fits were made to the elastic cross section at only the three angles indicated, 160, 120 and 90°. The only significant restriction imposed by the multi-level code is a limit of 400 calculated fit points and 600 data points for each of up to three angles. Since the data, as measured, contain about 1000 points in each 100 keV wide span, careful selection of the optimum energy increment and of the range of the calculation was required.

In the actual fitting procedure, both GALAHAD and MULTI were placed in disc storage at a central IBM system 360/75 terminal (Triangle Universities Computing Center) and were called from a local tele-processing terminal. Crude plots were generated on a line printer for comparison of the fit to the data.

Although the detailed interpretation of these data will be treated

Figure 24. A Sample Multilevel Fit to the $^{22}Ne(p,p)^{22}Ne$ Data at Three Angles. This data includes the region of the $3/2^-$ analogue state. The data points indicated are in 1 keV steps, except over very narrow resonances, where more of the actual data points are included. The complexity of the data, due to overlapping levels, is evident here.

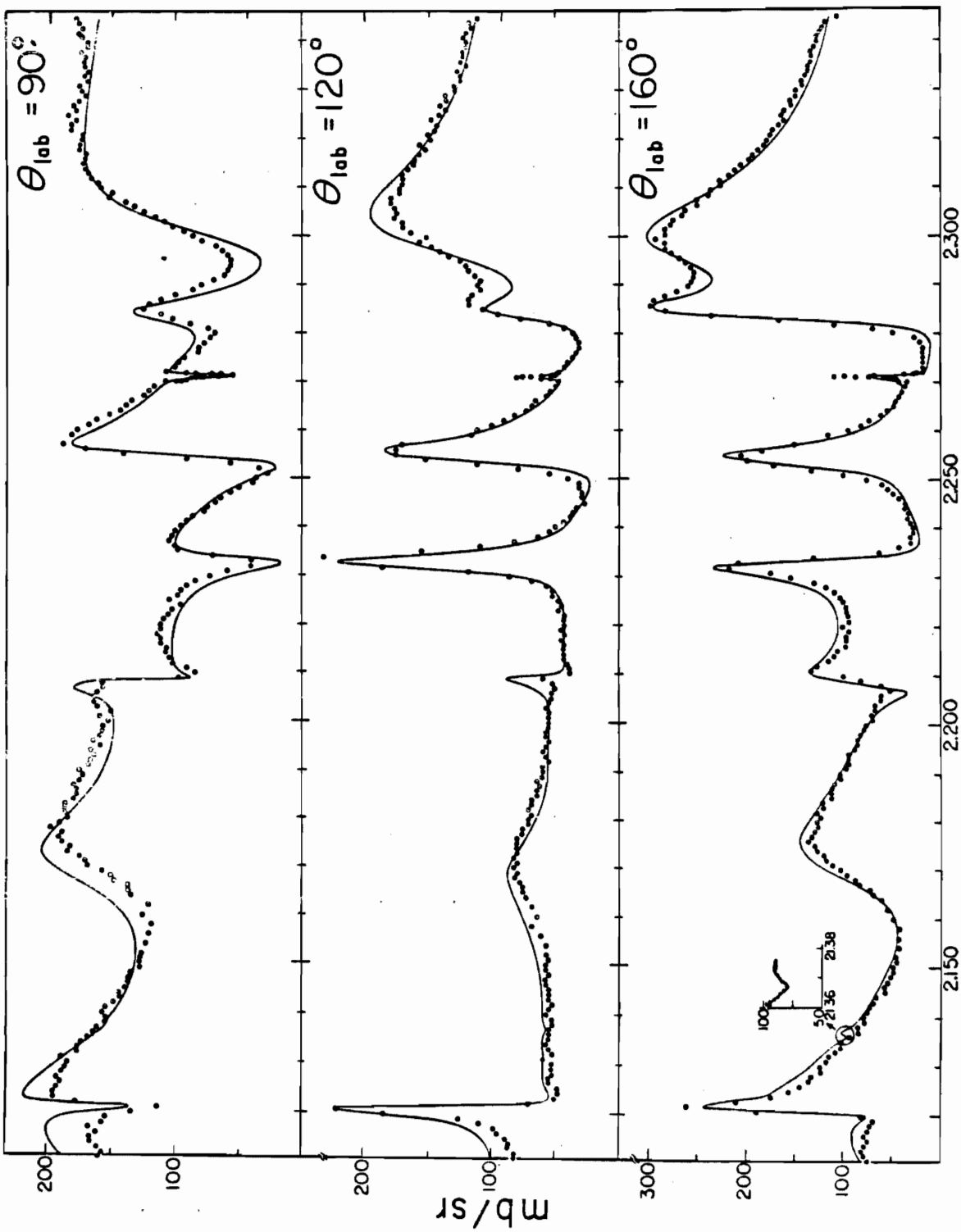
θlab = 90°
θlab = 120°
θlab = 160°
mb/sr
Ep (MeV)
2.150
2.200
2.250
2.300
100
200
300
2.136
2.138

in the next chapter, one particular feature of these data is in marked contrast to the ^{40}A data. That is the apparent lack of any clustering of particularly strong states representing a region of an analogue state. Two strong bound states in ^{23}Ne should have their analogues in ^{23}Na at incident proton energies of between 2.0 and 2.6 MeV and separated by about 210 keV. However, due to masking by the normal $T_<$ states, none of the expected structure is evident before detailed analysis.

Chapter V

DISCUSSION

A. ^{41}K

Reduced widths for the proton resonances analyzed were computed from the widths listed in Table 1. An integral plot of the reduced widths for each of the important spin states is presented in Fig. 25; the slope of each curve gives the local value of the corresponding strength function $\langle \gamma_p^2/D \rangle$. The effects of the two isobaric analogue resonances in this energy region are visible in the very sharp increase of the $3/2^-$ plot near 1.87 MeV and the similar sharp increase of the $1/2^+$ plot at 2.45 MeV. As is to be expected, the enhancement of the fine structure at each analogue resonance is confined to a single value of spin and parity; the $1/2^-$ reduced width plot shows an essentially constant strength function throughout the energy range studied, and no sign of an analogue resonance is evident here. These data definitely assign spin and parity $3/2^-$ to the 1.87 MeV analogue resonance and $1/2^+$ to the 2.45 MeV resonance, and of course imply the same spin and parity assignments for the corresponding

Figure 25. Integral Histogram of Reduced Widths γ_p^2 of Resonances in $^{40}A(p,p)^{40}A$. The effects of the two analogue resonances are visible as anomalous rises in the $3/2^-$ plot at 1.87 MeV and in the $1/2^+$ plot near 2.45 MeV. The sum of reduced widths of individual resonances involved in each analogue is estimated by correcting the height of the anomalous rise for the small off-resonance strength function.

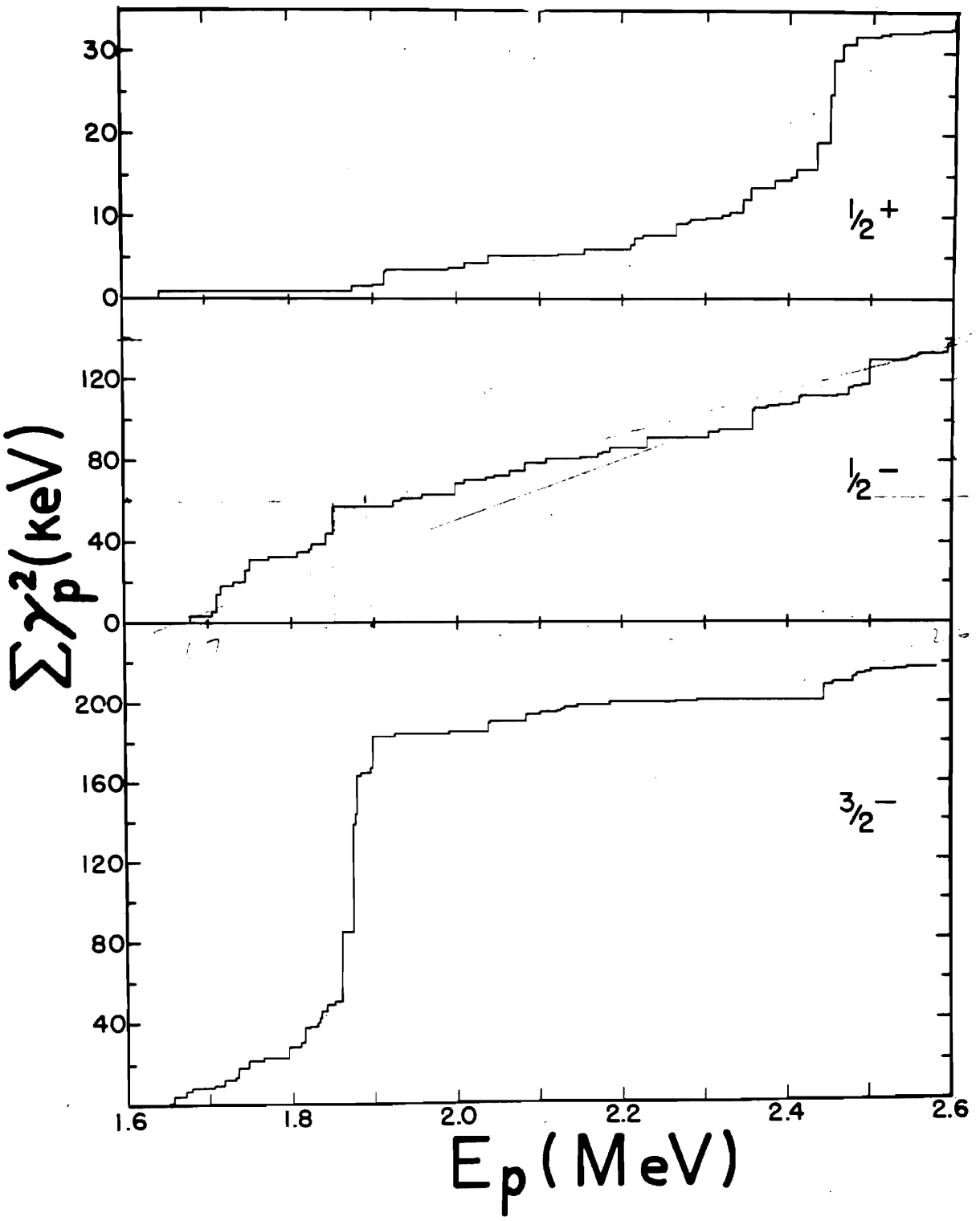
30
20
10
0
1/2+
120
80
40
0
1/2−
200
160
120
80
40
3/2−
1.6
1.8
2.0
2.2
2.4
2.6
Σγp²(keV)
Ep(MeV)

states in ^{41}A (at 1.354 and 1.871 MeV excitation energy, respectively). The 1.354 level in ^{41}A in direct observation by means of the ^{40}A(d, p)^{41}A reaction could[26] be assigned as either $1/2^-$ or $3/2^-$. The Coulomb energy difference implied by these measurements is 6.56 MeV or $1.26Z/A^{1/3}$ for the $3/2^-$ analogue and 6.61 MeV or $1.27Z/A^{1/3}$ for the $1/2^+$ state. These values are in fair agreement with the empirical formula of Long et al.[29] which predicts $\Delta E_c = 6.52$ MeV.

In chapter II, it was pointed out that an asymmetry of the fine structure enhancement is a characteristic feature of isobaric analogue resonances. The integral plots of Fig. 25 clearly indicate an asymmetry; the slopes of the $1/2^+$ and $3/2^-$ curves increase slowly over a considerable energy range below the analogue resonance and cut off sharply above. Fig. 26 shows differential strength function plots made by calculating $\langle \gamma_p^2/D \rangle$ from all resonances within ±20 keV of E_p. The smooth curves in Fig. 26 are attempted fits to eq. (2.3) with the indicated parameters. Although the histograms of Fig. 26 necessarily involve rather poor statistics, it is plain that quite good agreement can be obtained with the form of eq. (2.3). The values of Γ (16 and 20 keV in the $1/2^+$ and $3/2^-$ plots, which are of the order of the Wigner limit) which must be used in eq. (2.3) in order to match the observed asymmetry are, however, in gross disagreement with the values of Γ_p for the analogue resonances (±3 keV in both cases) obtained, as discussed below. It has been suggested[21] that the discrepancy is due to the fact that the states involved are not pure single-

Figure 26. Differential Strength Function Plots of the $3/2^-$ and $1/2^+$ Analogue Resonances. The curves are calculated from eq. (2.3) with Γ=20 keV, Δ= -74 keV, E_A = 1.878 MeV for the $3/2^-$ plot and Γ = 16 keV, Δ= -45 keV, E_A = 2.455 MeV for the $1/2^+$ plot. The curves are averaged over ± 20 keV to match the data.

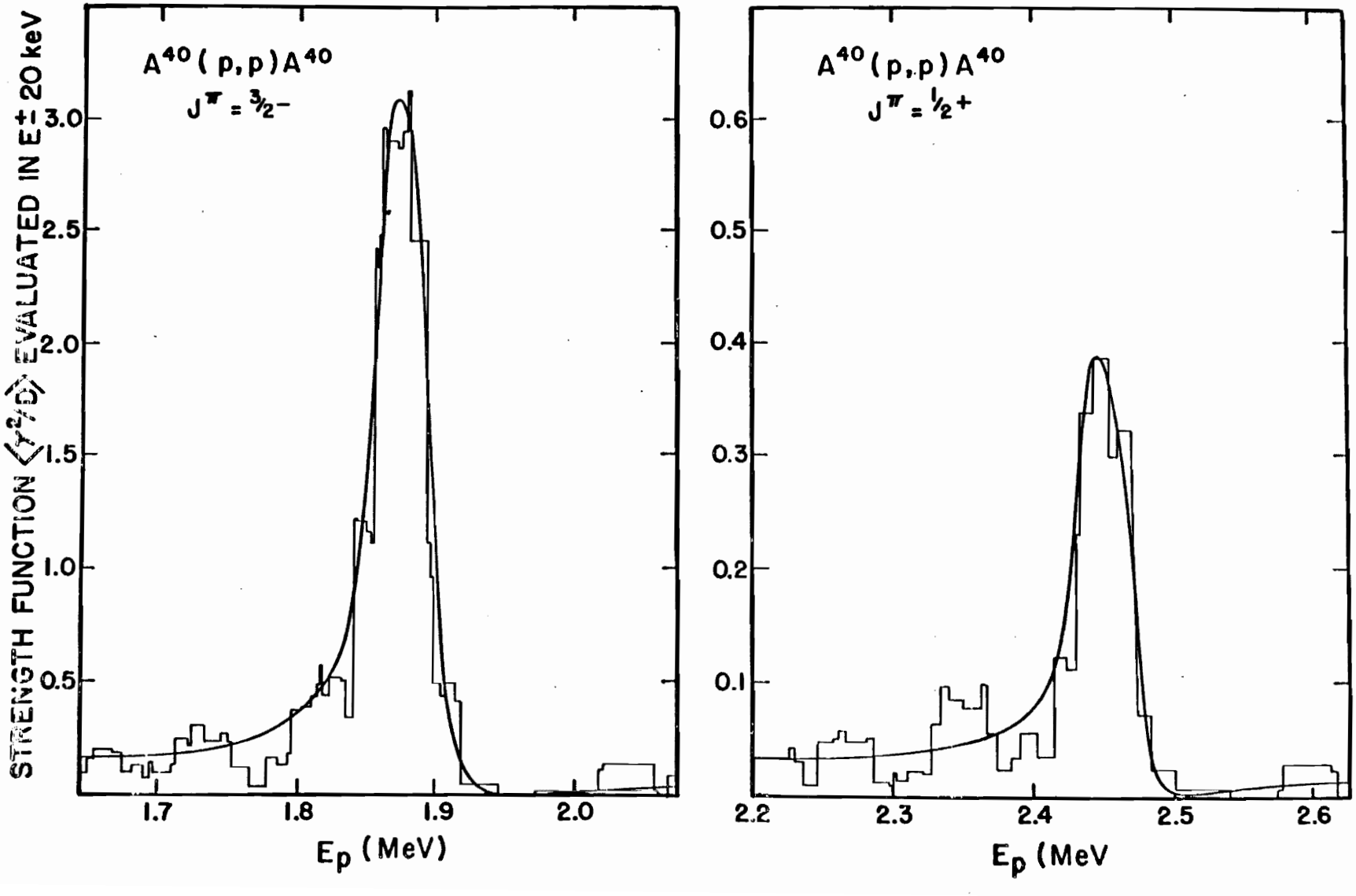
A40 (p, p) A40
Jπ = 3/2−
STRENGTH FUNCTION ⟨γ²/D⟩ EVALUATED IN E± 20 keV
3.0
2.5
2.0
1.5
1.0
0.5
1.7
1.8
1.9
2.0
Ep (MeV)
A40 (p, p) A40
Jπ = 1/2+
0.6
0.5
0.4
0.3
0.2
0.1
2.2
2.3
2.4
2.5
2.6
Ep (MeV

particle states, and the value of Γ in eq. (2.3) is no longer equal to Γ_p. Mekjian et al.[14] have obtained a good fit with more reasonable parameters within their "K-matrix" theory of fine structure in nuclear reactions.[15]

It is also evident from the plots in Fig. 25 that there is an apparent increase in the level density in the neighborhood of the analogue resonance. This may be due to a real increase in the level density at the analogue resonance or merely to a large fraction of the resonances far away from the analogue state enhancement having been missed because of the finite energy resolution. Any evidence for a real increase in the level density at the energy of the isobaric analogue would be of considerable interest; as the following analysis will show, however, the observed results are entirely consistent with the assumption that the true level density is constant throughout the range of measurement.

If the true level density is assumed to be that near an analogue resonance, such as the region at 2.45 MeV, then the spacing observed far from this region determines the fraction of resonances missed, in this case 58%. Assuming a Porter-Thomas[30] distribution for the reduced widths γ_p^2 and given the average reduced width observed, one can then calculate that 58% of the levels will be missed if all $1/2^+$ resonances with a width of less than 15 eV are unobserved. The corresponding figure for the $3/2^-$ resonances is 25 eV. The values are in reasonable agreement with the smallest widths listed in Table 1. Within the accuracy of the calculation, therefore, these data are consistent with the assumption that

the true level density is a constant.

An estimate of the spreading width for these two analogue resonances has been obtained by smearing out the fine structure with a 30 keV running average and fitting the result with a single level shape. The best fits give proton widths of 1.3 and 2.4 keV, respectively, for the 1.87 and 2.45 MeV resonances. The total widths of these two states, however, are much less definitely determined by the single level fits. For both states, the total widths are between 4 and 15 keV.

If the sum rule (eq. (2.6) is applied to these two analogue regions, values for the reduced width of the analogue state, γ_p^2, before isospin mixing is introduced, of 140 and 18 keV for the 1.87 and 2.45 MeV analogues, respectively, are obtained. Here the assumption is made that $\sum_\mu \gamma_{\mu p}^2$ is negligible. The gross-structure reduced widths obtained above are 60 and 18 keV. Thus, agreement is obtained for the $1/2^+$ level and not for the $3/2^-$ case. Robson[21] points out, however, that γ_p^2 is not necessarily determined by averaging over energy and fitting the result with a single level formula.

Estimating Γ_p, as discussed above, from the sum of the individual widths of the same J^π in the neighborhood of the analogue resonance, gives about 3 keV for both the 1.87 and 2.45 states. We can then apply eq. (2.5) where the neutron capture width is determined from the spectroscopic factor for (d,p) stripping:

$$S(d,p) = \frac{\gamma_n^2}{\gamma_{sp}^2} \qquad (5.1)$$

Estimating γ_{sp}^2 simply as $\hbar^2/ma^2 = 1.3$ MeV predicts (d, p) spectroscopic factors of 0.52 for the 1.354 level of ^{41}A and 0.06 for the 1.871 level.

No spectroscopic factors were extracted by Kashy et al.,[26] but their data together with tabulated systematics of plane-wave stripping widths[31] suggest $S(3/2^-) \approx 0.7$ for the lower level. Approximate spectroscopic factors have been extracted from the data of Ref. 25 by making a DWBA fit, yielding $S \approx 0.59$ for the lower $(3/2^-)$ level and $S \approx 0.03$ for the higher $(1/2^+)$ level. The agreement with the values derived from the analogue states in ^{41}K is quite satisfactory, and in assigning $J^\pi = 3/2^-$ to the 1.354 MeV level in ^{41}A, the analogue resonance experiment even provides information not available in the (d, p) experiment.

Up to this point little attention has been devoted to the (p, α) and (p, n) measurements, primarily because these data can only be analyzed where resonances are observed in the elastic cross section. In the (p, n) data the structure is complex and many resonances are observed as one gets well above threshold, but the strength of these resonances seems merely to follow the trend of the penetrabilities. There is no increase in the (p, n) strength near the 2.45 $(1/2^+)$ analogue resonance, presumably because of the low penetrability for the required $\ell = 3$ neutrons near threshold.

The ^{40}A(p, α)^{37}Cl reaction, on the other hand, does show some participation in the 1.87 MeV $(3/2^-)$ analogue resonance, as Fig. 27 illustrates. The histogram was obtained by summing the areas of all (p, α)

Figure 27. Plot of the Relative Strength of the $^{40}A(p,\alpha)^{37}Cl$ Resonances against Energy. All (p,α) resonances observed are included.

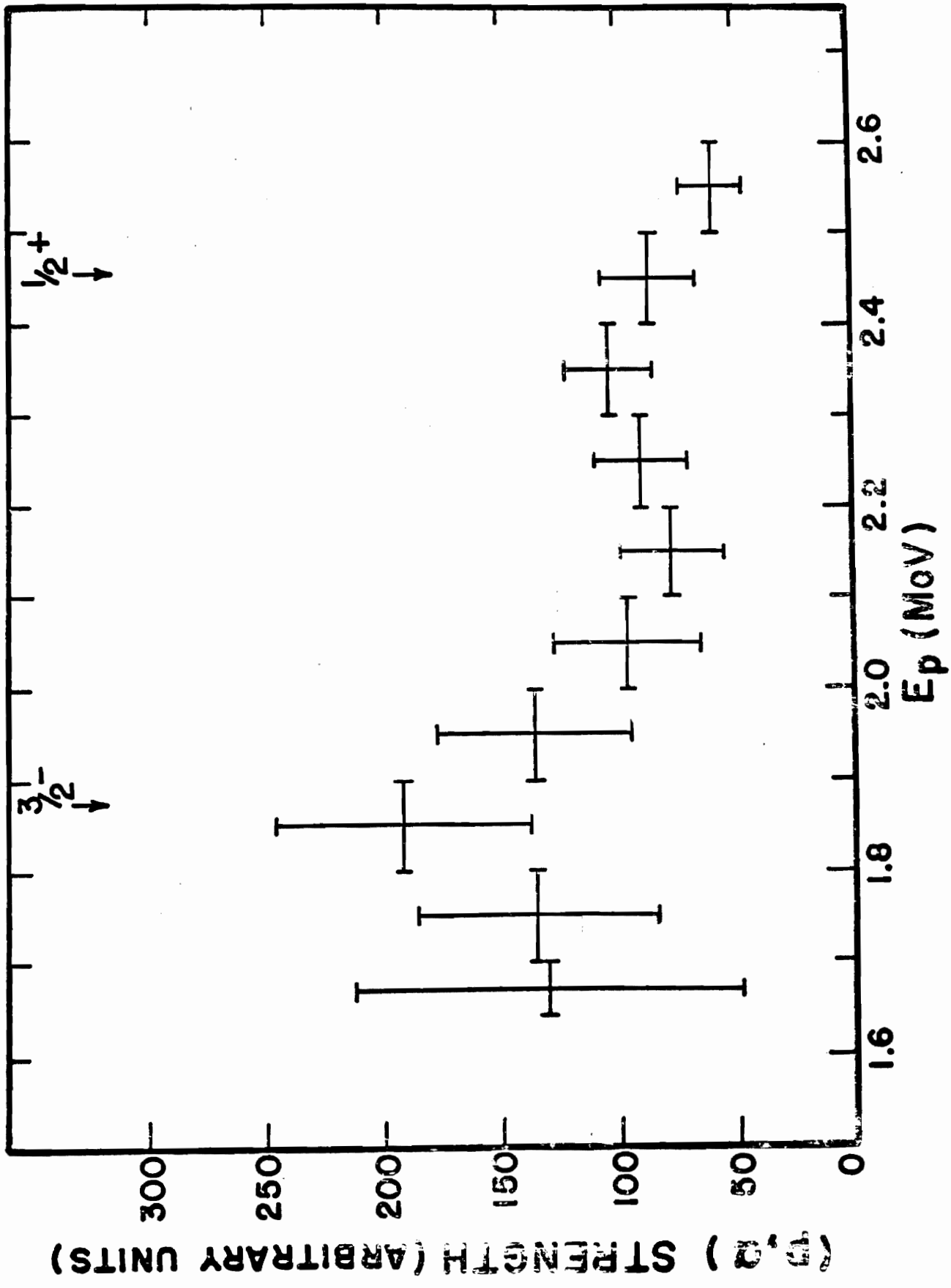
(p,α) STRENGTH (ARBITRARY UNITS)
300
250
200
150
100
50
0
1.6
1.8
2.0
2.2
2.4
2.6
Ep (MeV)
3/2-
1/2+

resonances in each 100 keV interval and removing the energy dependence due to λ^2 and the α-particle penetrability (eq. (4.2)); a maximum is seen in the neighborhood of the 1.87 MeV analogue resonance. No corresponding effect of the 2.45 MeV resonance is visible in Fig. 27, both because of the less favorable α-particle penetrability and because of the decreased (p,α) strength above (p,n) threshold due to the competition of neutron decay. In principle, decay of the $T_>$ analogue states by neutron or α-particle emission is isospin forbidden. The rather complete fragmentation of the analogue levels observed in this experiment, however, implies a considerable degree of isospin mixing, so that this argument does not explain the absence of the 2.45 MeV analogue resonance from the (p,n) and (p,α) data. However, as mentioned above, penetration effects for the required $\ell = 3$ neutrons would probably prohibit a visible enhancement in the (p,n) channel.

B. ^{23}Na

It was pointed out in the conclusion of Chapter IV that there are no striking regions of particularly strong resonances in the cross sections of either the elastic or inelastic scattering of protons from ^{22}Ne. Yet the effects of at least two analogue states are to be expected if one could examine resonances of each spin state without the obscuring background. As in the previous discussion of ^{41}K, reduced widths for the proton resonances, calculated in the fitting procedure, were used to produce the

integral plots of Fig. 28 for each spin state which is prevalent in the data.

Perhaps, before interpreting these plots, it would be worthwhile to examine the bound levels in ^{23}Ne which are the parent states of the analogues expected to be found in the range of measurement in ^{23}Na discussed here. These levels are shown in Fig. 29 with J^{π} values indicated as derived from (d,p) stripping measurements[32,33] on ^{22}Ne in conjunction with (d,pγ) proton-gamma angular correlation measurements.[34] As a first guess, if 1.2 fermis is taken as a reasonable estimate for R_c in calculating the Coulomb energy difference between ^{23}Ne and ^{23}Na, then a proton with zero bombarding energy would hypothetically be able to excite the isobaric analogue state in ^{23}Na of the first excited state in ^{23}Ne. Thus the remaining eight excited states in Fig. 29 should also have their analogues within the range of measurement in ^{23}Na. However, Lutz et al.[32] have determined spectroscopic factors for most of these states, which indicate that only the sixth, seventh and ninth excited states in ^{23}Ne, with spectroscopic factors of 0.42, 0.37 and 0.31, respectively, are strong enough to have visible analogue states in ^{23}Na.

One source of confusion here is the J^{π} assigned to the sixth excited state in ^{23}Ne. Refs. 33 and 34 have indicated $\ell = 1$ and $J \geq 3/2$ for this state. Ref. 32, however, assignes $J^{\pi} = 1/2^{+}$. This latter assignment was made on rather general considerations based on the level sequence expected for negative parity states, since the difference between $\ell = 0$ and $\ell = 1$ DWBA curves was not sufficient to distinguish a definite ℓ-value. The mea-

Figure 28. Integral Histogram of Reduced Widths γ_p^2 of Resonances in $^{22}Ne(p,p)^{22}Ne$. The effects of the two analogue resonances are visible as anomalous rises in the $3/2^-$ plot at 2.15 MeV and in the $3/2^+$ plot near 2.5 MeV. The small anomaly in the $1/2^+$ plot at 2.3 MeV is not attributed to an analogue state.

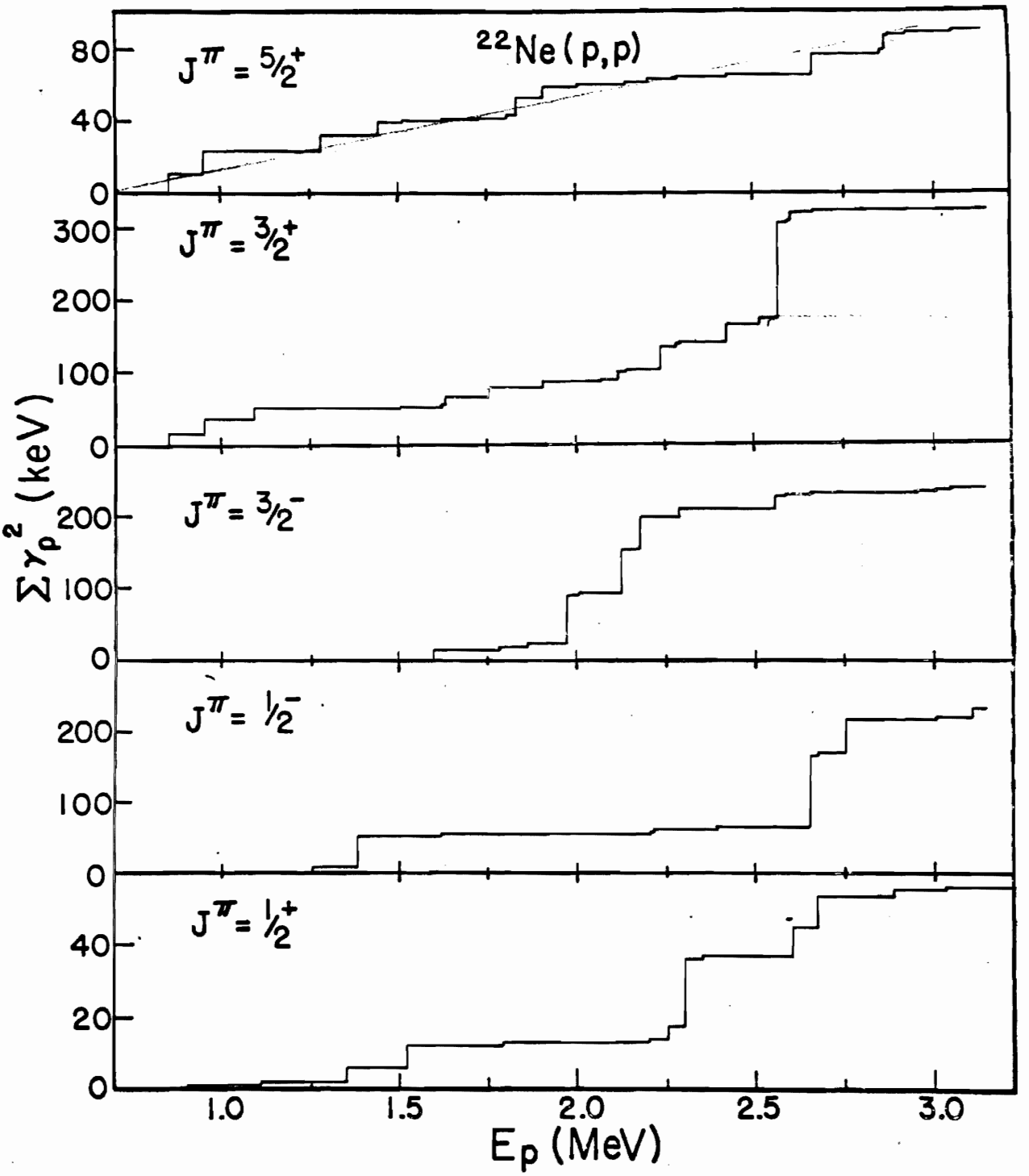
^{22}Ne (p,p)
$J^\pi = 5/2^+$
$J^\pi = 3/2^+$
$J^\pi = 3/2^-$
$J^\pi = 1/2^-$
$J^\pi = 1/2^+$
$\Sigma \gamma_p^2$ (keV)
E_p (MeV)
0
40
80
100
200
300
20
1.0
1.5
2.0
2.5
3.0

Figure 29. Energy Level Diagram of ^{23}Ne. The sixth and seventh excited states at 3.218 and 3.433 MeV, respectively, are the parent states of the two analogue states seen in ^{23}Na.

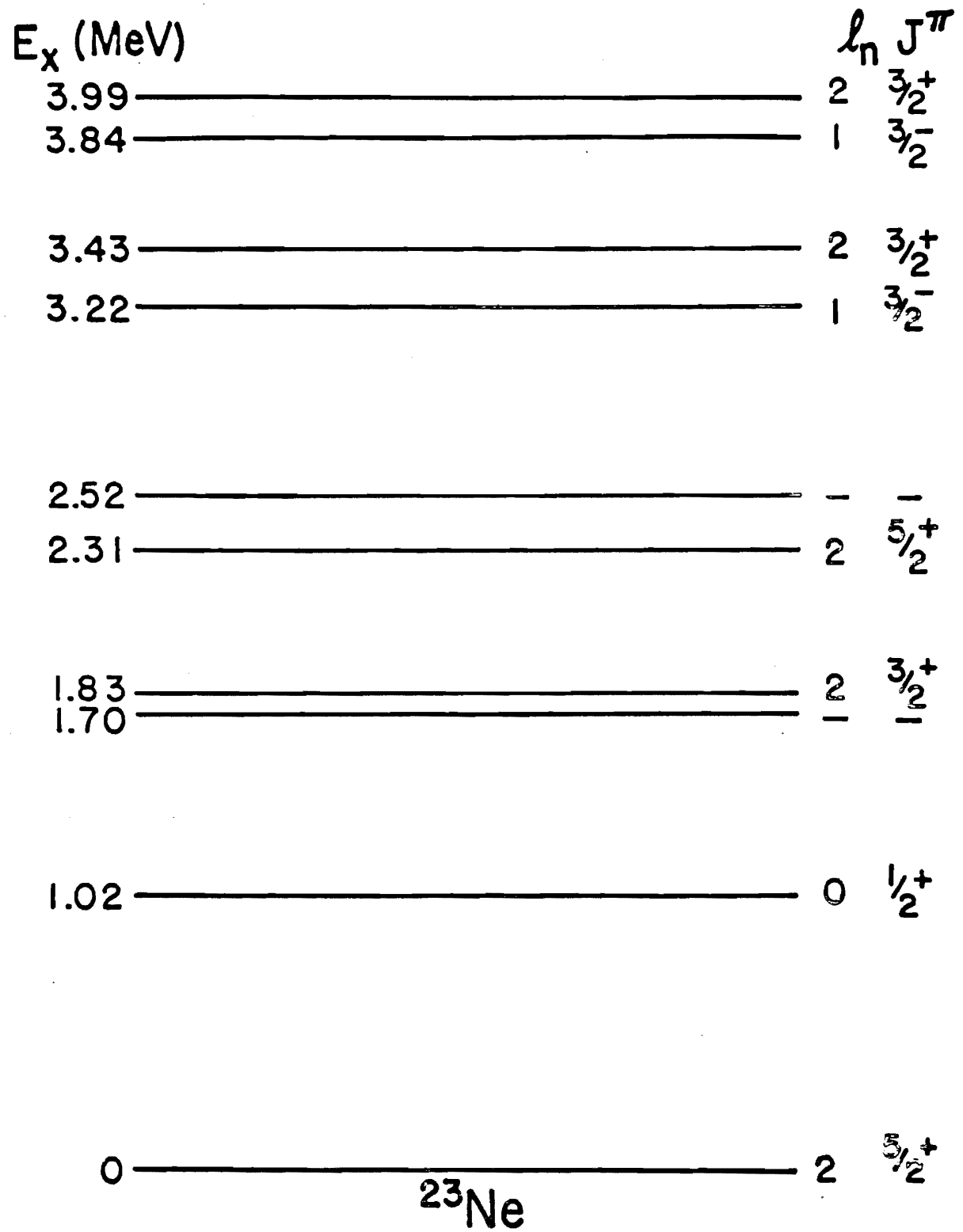
E_x (MeV)
l_n J^π
3.99
2
$3/2^+$
3.84
1
$3/2^-$
3.43
2
$3/2^+$
3.22
1
$3/2^-$
2.52
—
—
2.31
2
$5/2^+$
1.83
2
$3/2^+$
1.70
—
—
1.02
0
$1/2^+$
0
2
$5/2^+$
^{23}Ne

surements and the analyses in the latter two references seem more definitely to indicate that this level has $J^{\pi} = 3/2^{-}$. Fortunately, Ref. 32 does give a spectroscopic factor for this level with $J^{\pi} = 3/2^{-}$, in addition to that derived from assuming their preferred $J^{\pi} = 1/2^{+}$ assignment.

Having at least determined the relative positions of the three parent states which might be expected to have their analogues observable in ^{23}Na, interpretation of the integral plots in Fig. 28 may be undertaken. The effect of the analogue of the sixth excited state in ^{23}Ne is clearly in evidence in the neighborhood of 2.15 MeV, while the analogue of the next excited state is visible in the $3/2^{+}$ plot near 2.5 MeV. Of the three other plots, only that for the $1/2^{+}$ states shows any indication of a local increase in slope. However, this relatively weak indication is primarily caused by a single strong state at 2.299 MeV and not, as in the two other cases, by a rather broad enhancement. Nevertheless, if this particular increase in slope did correspond to an analogue state, it would imply a spectroscopic factor for the parent state in ^{23}Ne of about 0.07. This is strong enough to be visible in the (d, p) data, and there is no indication that such a level exists in the range of excitation 2.0 - 4.0 MeV in ^{23}Ne. With resolution, in the (d, p) experiment, capable of distinguishing doublets separated by more than 20 keV, it would seem unlikely that this hypothetical state would not be resolved. However, this anomaly demonstrates the difficulty of identifying weak analogue states in a compound system with such strong background $T_{<}$ states as ^{23}Na.

Although the resonance energy of the two analogue states is not precisely determined (±30 keV for the $3/2^-$ state and ±50 keV for the $3/2^+$), due to the large widths of the regions of enhancement, it is clear that the separation between these two analogue states is somewhat larger ($\sim$0.35 MeV) than that between the parent states (0.21 MeV). These measurements imply a Coulomb energy difference for ^{23}Ne, determined from the $3/2^-$ state, of 4.03 ± 0.03 MeV or 1.15 $Z/A^{1/3}$ and 4.15 ± 0.05 MeV or 1.18 $Z/A^{1/3}$ from the $3/2^+$ state. This difference in ΔE_c, as separately derived for the two analogue states, is large but is no greater than has been observed elsewhere[35] for analogues within one nucleus but of different ℓ-value. With these assumptions, the analogue of the 3.99 MeV $3/2^+$ excited state in ^{23}Ne should appear, using the value for ΔE_c determined for the other $3/2^+$ analogue, at about 3.06 MeV in these data. Although this level, the ninth excited state in ^{23}Ne, appears to be strong in the (d,p) measurements, there is no evidence of any strong $3/2^+$ resonances within the range 2.8 to 3.1 MeV. Since there is no particularly strong behavior indicated in this energy range in the integral plots of Fig. 28 for any other spin and parity state, the failure of this state to appear in the $3/2^+$ plot cannot be due to a J^π misassignment. It is possible, however, that this state is just outside the present range of measurement or that it is weaker than predicted.

The asymmetry of the form of the resonance enhancement in the regions of the analogue states is less clear for the $3/2^-$ analogue at 2.15 MeV than for the $3/2^+$. The enhancement resulting from the lower state

is nearly symmetric whereas, in the latter case, there are many $3/2^+$ resonances below the energy of the analogue state but, above 2.62 MeV, no $3/2^+$ resonances are observed. In Fig. 30, differential strength function plots made by calculating $\langle \gamma_p^2/D \rangle$ from all resonances within ±100 keV of E_p are shown. The smooth curves are, as in the ^{41}K discussion, attempts to fit the distribution with eq. (2.3). It is perhaps evident from the figure, however, that a number of other curves calculated from eq. (2.3) would be nearly as suitable as those indicated; thus, the indicated parameters are hardly unique. Nevertheless, the values of Γ and Δ used in calculating the curves may be checked for consistency in a straightforward manner. A simple relation which must be satisfied by these parameters is[14]

$$\left(\frac{\Gamma}{2\Delta}\right)^2 = \frac{\gamma_\mu^2}{\gamma_{p_{max}}^2} \qquad (5.2)$$

where Γ is approximately the width at half maximum of the distribution in Fig. 30, $\Delta = E_s - E_a$ where E_s is the energy at which the reduced widths go to zero and E_a is the position of the maximum reduced width $\gamma_{p_{max}}^2$, and γ_μ^2 is the average value of γ_p^2 far from E_a. The values for γ_μ^2 derived from this relation are given in Table 3 for the two analogue states under discussion. Particularly in the $3/2^+$ case, the γ_μ^2 thus estimated are quite large, implying a strong background of $T_<$ states which is certainly consistent with the data.

Also given in Table 3 are the results of the two sums $\sum_J \gamma_J^2$

Figure 30. Differential Strength Function Plots of the $3/2^-$ and $3/2^+$ Analogue Resonances. The solid curves are calculated from eq. (2.3).

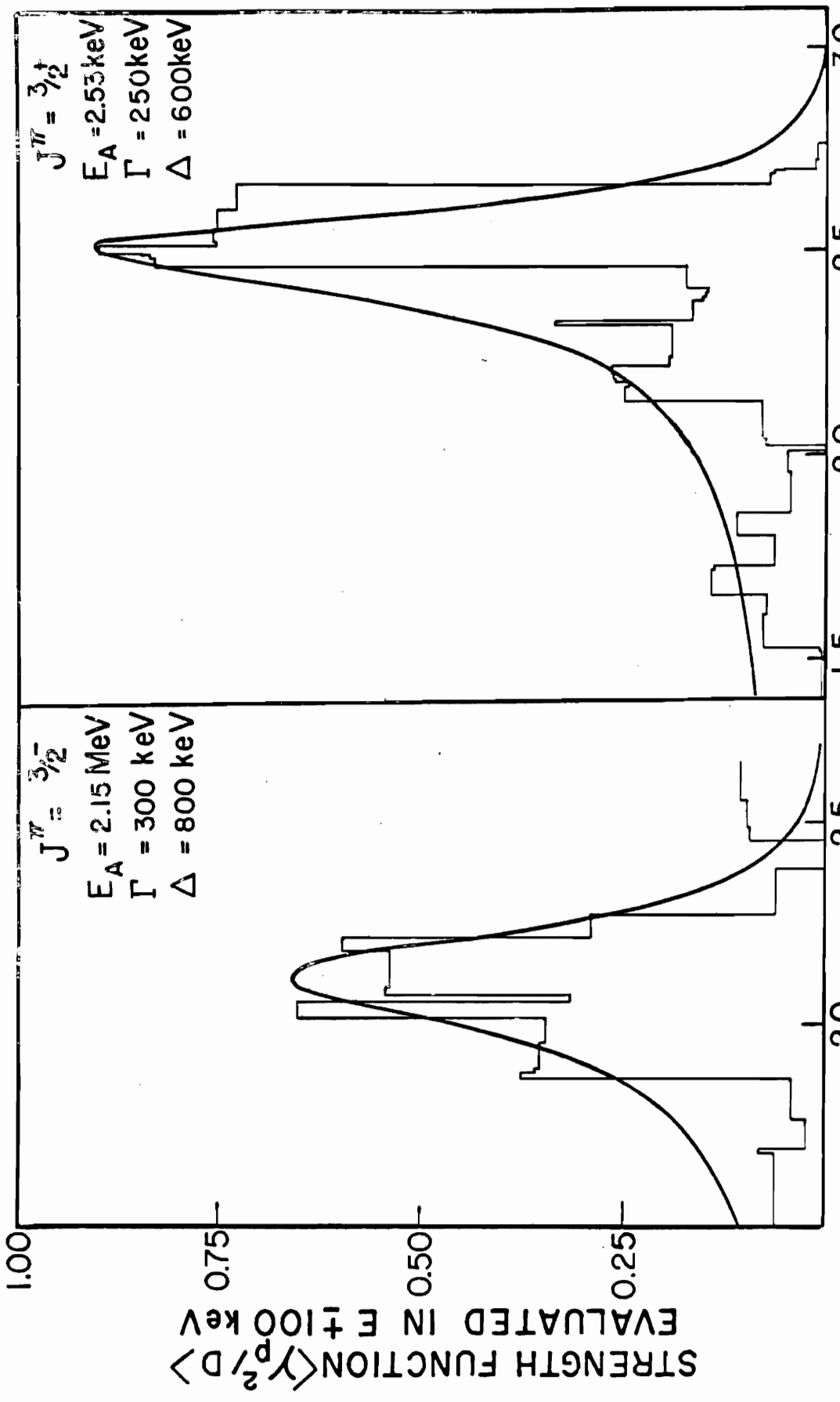
$J^\pi = 3/2^+$
E_A = 2.53keV
Γ = 250keV
Δ = 600keV
$J^\pi = 3/2^-$
E_A = 2.15 MeV
Γ = 300 keV
Δ = 800 keV
STRENGTH FUNCTION $\langle \gamma_p^2 / D \rangle$
EVALUATED IN E ± 100 keV
1.00
0.75
0.50
0.25
2.0
2.5
1.5
2.0
2.5
3.0
E_p (MeV)

Table 3. Analogue State Parameters

	Γ (MeV)	Δ (MeV)	γ_μ^2 (keV)	$\langle D \rangle^{-1}$ (MeV)$^{-1}$	$\sum \gamma_\mu^2$ (keV)
^{41}K ($3/2^-$)	0.02	-0.074	0.97	150	22
^{41}K ($1/2^+$)	0.016	-0.045	0.18	65	1.8
^{23}Na ($3/2^-$)	0.3	-0.8	2.4	10	14
^{23}Na ($3/2^+$)	0.25	-0.6	5.7	18	61

and $\sum_{\mu} \gamma_{\mu}^{2}$. The former is simply the sum of reduced widths for all resonances whose spin and parity are those of the analogue state taken over the apparent range of enhancement. The latter sum was estimated by assuming γ_{μ}^{2}, as derived above, to be the average background reduced width and multiplying this average width by the number of levels expected to be within the region of enhancement. The average level densities thus used and indicated in Table 3, are estimated from the level densities for states with suitable J^{π} observed in the region of enhancement. Using the sum rule of eq. (2.6), the reduced widths for the two analogue states are then ~220 and ~195 keV for the $3/2^{-}$ and $3/2^{+}$ states, respectively.

Spectroscopic factors for the sixth and seventh excited states in ^{23}Ne are calculated in Ref. 32 from their (d,p) stripping results and are given as 0.42 for the $3/2^{-}$ state and 0.37 for the other. Assuming γ_{sp}^{2} to be equal to the Wigner limit (1.9 MeV for R = 4.75 f.), eq. (5.1) predicts values for γ_{p}^{2} of 266 and 234 keV for the $3/2^{-}$ and $3/2^{+}$ analogues in ^{23}Na, respectively. The agreement with the values derived from the sum rule applied to the elastic scattering measurements discussed here is quite good, being well within the experimental errors associated with the reduced width determinations.

It is interesting to note that, in the case of the $3/2^{+}$ analogue, one resonance in ^{23}Na, at a proton energy of 2.5675 MeV, has a width which is more than two-thirds that of Γ_{a}, the analogue state width. No such dominant state is found in the $3/2^{-}$ analogue. It is surprising that

one level, whose width is small compared to the spreading width, should contain such a large portion of the total width of the analogue state. One immediate explanation is that the state was exceptionally strong before enhancement. However, this interpretation would necessitate such a large reduction in γ_p^2, derived from the sum rule, that this quantity would strongly disagree with the analogue width derived from the stripping measurements. Thus, another explanation must be sought.

Another interpretation, although a tenuous one, is that this one particular $3/2^+$ state has been preferentially enhanced over the other $T_<$ states. For example, this exceptionally large $3/2^+$ level and the large $5/2^+$ level at $E_p = 2.655$ MeV could be formed through coupling an $\ell = 0$ incident proton to the target nucleus excited to a 2^+ state, in the framework of the weak-coupling picture of core excitation,[36] resulting in a $3/2^+$ and $5/2^+$ state. The $5/2^+$ resonance observed has both the largest reduced width of all $5/2^+$ resonances measured and also an exceptionally large inelastic proton width. Thus, these states may perhaps be of different composition than the other $\ell = 2$ resonances. However, too little of the microscopic detail of the composition of the individual levels and of the enhancement mechanism is known to permit substantiation of these surmises.

At the outset of this experiment, it was hoped that the behavior of the cross section for inelastically scattered protons in the region of the analogue states would be of substantial interest. It was expected

that the inelastic protons would appear to share strongly in the enhancement in these regions, particularly for an $\ell = 2$ analogue state, where the outgoing inelastic protons have $\ell = 0$. In the region of each analogue, a few fairly strong states were seen, but these serve mainly to corroborate the existence of the analogues. The fraction of inelastic width, $\Gamma_{p'}/\Gamma$, appears to be essentially the same in the region of enhancement as far away. As seen in the integral histograms of Fig. 31, the behavior of any enhancement is not definite. This lack of clarity is partially induced, perhaps, by the lack of low-energy measurements. The few resonances observed in the inelastic cross section below 2.0 MeV did not have reduced widths sufficiently well determined to permit their inclusion in the plots of Fig. 31. Nevertheless, it does appear that the inelastic protons do, to some extent, partake in the analogue state enhancement. It is interesting to note that the enhancement in each of the two proton channels is not level by level; that is, one particular level may be strongly enhanced in the elastic channel and remain weak in the inelastic channel whereas another level may appear more strongly in the inelastic channel. Thus, it is the overall enhancement that must be considered.

One feature of the ^{22}Ne experiment that differs from the ^{40}A measurements is that the levels which are enhanced in the region of the analogue state are of sufficient strength to be visible without the enhancement. This observation is substantiated by the fact that the level density in the region of the analogues is approximately the same as that far away

Figure 31. Integral Histogram of Reduced Widths $\gamma^2_{p'}$ of Resonances in the Reaction $^{22}Ne(p,p')^{22}Ne^*$ with $J^\pi = 3/2^-$ and $3/2^+$. Here, as in Fig. 28, the effects of the two analogue resonances are visible as rises in the $3/2^-$ plot at 2.15 MeV and in the $3/2^+$ plot near 2.5 MeV.

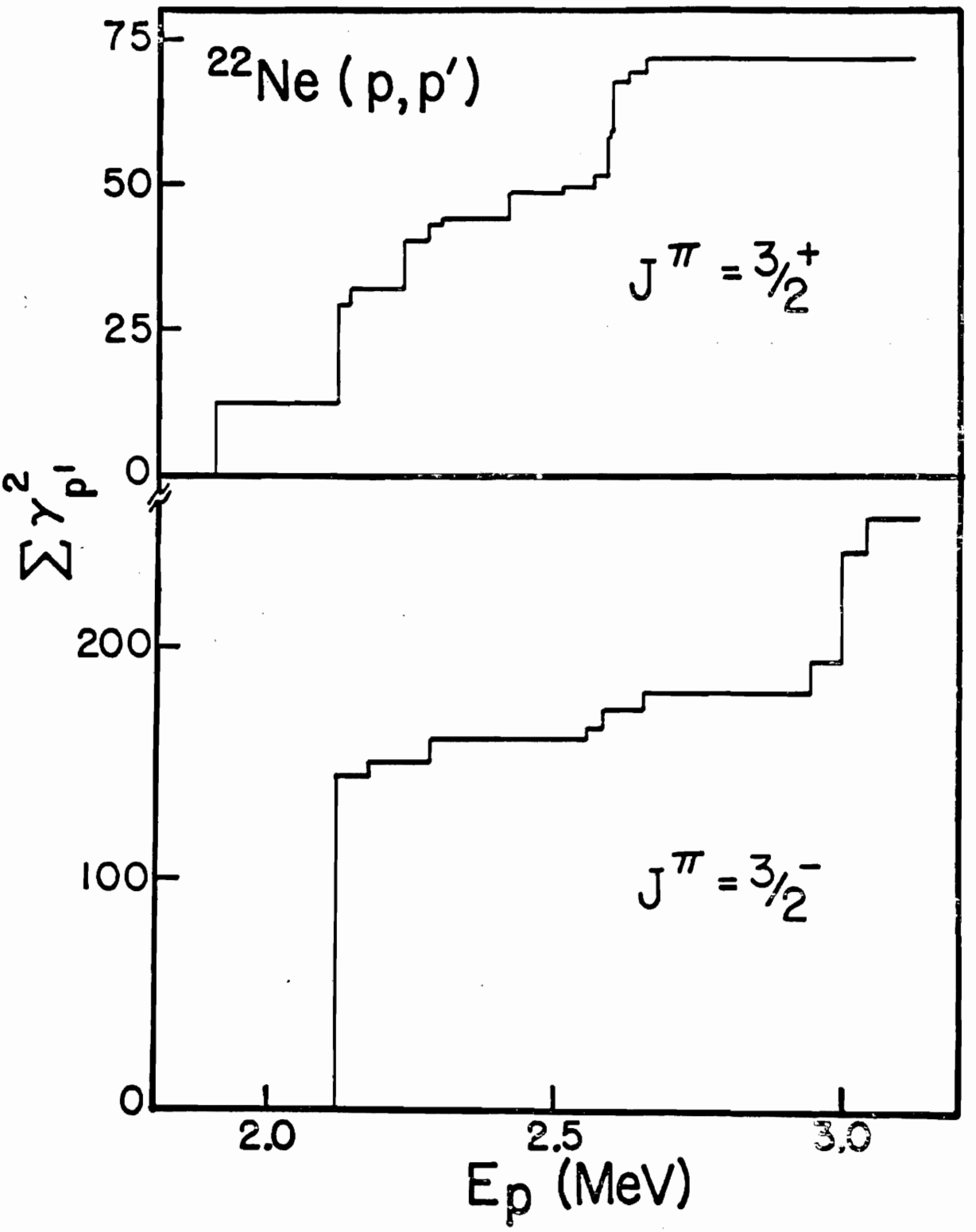
^{22}Ne (p, p′)
$J^\pi = 3/2^+$
$J^\pi = 3/2^-$
$\sum Y^2_{p'}$
75
50
25
0
200
100
0
2.0
2.5
3.0
E_p (MeV)

from the analogue state. In Fig. 28, the integral plot of $5/2^+$ resonances shows no increase in slope with energy; if levels were missed due to their narrow widths, however, the increase in energy of the incident proton of about 2 MeV would imply that more levels would become visible and one would expect an increase in the slope of the plot.

Further substantiation is suggested by the fact that few resonances are not well resolved. In the ^{41}K measurements, the majority of resonances had widths narrower than the resolution function, whereas the inverse is true here. For resonances with $\Gamma_p = \Gamma$, a reasonable estimate for a minimum observable reduced width for states with $J^\pi = 1/2^+$ is ~15 eV (corresponding to $\Gamma_p \sim 10$ eV at $E_p = 2$ MeV). The average observed reduced width is, however, 4300 eV. Thus it would seem unlikely that many levels are unobserved in the ^{22}Ne measurements.

In conclusion, the results of these two experiments clearly demonstrate the fragmentation of the analogue state into an enhancement of the background $T_<$ states in the compound system. The analysis of these data demonstrates the successful application of this method of nuclear spectroscopy, along with some of the difficulties encountered, but also points out the need for a more microscopic understanding of the actual mechanisms involved.

Appendix A

R-MATRIX FITTING PROGRAMS

I. Single Level Analysis

In applying R-matrix theory to a reaction proceeding through an isolated resonance, all terms in the R-matrix sums over λ, where λ labels the members of a complete set of states in the compound system, are dropped except one. This leads to the Breit-Wigner single level formula. In the argon work, a relatively simple form of the single level formula given by Blatt and Biedenharn[37] was used with nuclear potential scattering ignored. In this case, the differential scattering for elastic protons is given by the expression:

$$\left(\frac{d\sigma}{d\Omega}\right)_{pp} = \frac{\lambda^2 \Gamma_p}{8\left[(E-E_o)^2+(\Gamma/2)^2\right]} \sum_{L=0}^{2J-1} \left[Z(\ell J \ell J; 1/2 L)\right]^2 P_L(\cos\theta) + \left[f_{coul}\right]^2$$

$$+ \frac{(J+1/2)\lambda f_{coul} \Gamma_p P_\ell(\cos\theta)}{\left[(E-E_o)^2+(\Gamma/2)^2\right]^{1/2}} \sin(2\eta \ln \sin\theta/2 + 2\psi_\ell + \beta) \qquad \text{(A.1)}$$

where

$$f_{coul} = \frac{\eta}{2k\sin^2\theta/2} \quad , \quad \beta = \arctan (E-E_o)/1/2\,\Gamma$$

for protons on even-even target nuclei. The notation used here and throughout is that of Ref. 37.

This expression was incorporated into a computer program which calculates the resonance shape for a given E_o, Z, A, J^{π}, θ, , and Γ_p, normalizes the data to the fit and simultaneously plots the two curves for direct comparison. A normalized Gaussian whose width corresponds to the width of the resolution function was used to effectively "smear" the predicted shape to correspond with experimental conditions.

In the case of elastic scattering from ^{22}Ne, however, nuclear potential scattering could not be neglected. Inclusion of nuclear potential phase shifts results in a somewhat more complicated expression:

$$\left(\frac{d\sigma}{d\Omega}\right)_{pp} = \left[f_{coul}\right]^2 - \frac{\eta}{k^2}\,\frac{1}{2\sin^2\theta/2}\sum_{\ell=0}^{\ell_{max}}\sum_{J=|\ell-1/2|}^{\ell+1/2}\Big[(2J+1)\sin(-\varphi_\ell)$$

$$\times\cos\left(2(\psi_\ell + \eta \ln\sin\theta/2\right)$$

$$-\varphi_\ell)\,P_\ell(\cos\theta)\Big] + \frac{1}{2k^2}\sum_{\ell_1=0}^{\ell_{max}}\sum_{J_1=|\ell_1-1/2|}^{\ell_1+1/2}\sum_{\ell_2=0}^{\ell_{max}}\sum_{J_2=|\ell_2-1/2|}^{\ell_2+1/2}\Big[\sin(-\varphi_{\ell_1})\sin(-\varphi_{\ell_2}) \qquad \text{(A.2)}$$

$$\times\cos\left(2(\psi_{\ell_1}-\psi_{\ell_2}\right)$$

$$-\varphi_{\ell_1}+\varphi_{\ell_2}\Big)\sum_{L=|\ell_1-\ell_2|}^{\ell_1+\ell_2}\left\{\left[\bar{Z}(\ell_1 J_1 \ell_2 J_2; 1/2\, L)\right]\right\}^2 P_L(\cos\theta)\Big] + \frac{1}{k^2\left[(E_0+\Delta-E)^2+(\Gamma/2)^2\right]}$$

$$\times \frac{\Gamma^2 J_0 \pi_0 \ell_0}{8}$$

$$\times \sum_{L=0,\,2\ldots}^{2J_0-1}\left[\bar{Z}(\ell_0 J_0 \ell_0 J_0; 1/2\, L)\right]^2 P_L(\cos\theta) + \frac{\eta}{k^2}\,\frac{\sin(\beta+2(\eta \ln\sin\theta/2 + \psi_{\ell_0}-\varphi_{\ell_0}))}{\left[(E_0+\Delta-E)^2+(\Gamma/2)^2\right]^{1/2}}$$

$$\times \frac{(2J_0+1)\,\Gamma_{J_0\pi_0\ell_0}\,P_{\ell_0}(\cos\theta)}{4\sin^2\theta/2} - \frac{\sin\beta}{k^2\left[(E_0+\Delta-E)^2+(\Gamma/2)^2\right]^{1/2}}$$

$$\times \frac{\Gamma_{J_0\pi_0\ell_0}}{2}\sum_{\ell=0}^{\ell_{max}}\sum_{J=|\ell-1/2|}^{\ell+1/2}$$

$$\left[\sin(-\varphi_\ell)\cos(2(\psi_{\ell_0}-\varphi_{\ell_0}-\psi_\ell)+\varphi_\ell)\sum_{L=|\ell_0-\ell|}^{\ell_0+\ell}\left[\bar{Z}(\ell_0 J_0 \ell J; 1/2 L)\right]^2 P_L(\cos\theta)\right]$$

$$-\frac{\cos\beta}{k^2\left[(E_0+\Delta-E)^2+(\Gamma/2)^2\right]^{1/2}}\,\frac{\Gamma_{J_0\pi_0\ell_0}}{2}\sum_{\ell=0}^{\ell_{max}}\sum_{J=|\ell-1/2|}^{\ell+1/2}\Big[\sin(-\varphi_\ell)$$

$$\times\sin(2(\psi_{\ell_0}-\varphi_{\ell_0}-\psi_\ell)+\varphi_\ell)$$

$$\times\sum_{L=|\ell_0-\ell|}^{\ell_0+\ell}\left[\bar{Z}(\ell_0 J_0 \ell J; 1/2\, L)\right]^2 P_L(\cos\theta)\Big]$$

As in eq. (A.1), the assumption of spin 1/2 projectile on spin zero target nuclei is made here. The notation is again that of Ref. 37 with the exception that the sign of φ_ℓ is reversed. The first three terms contain the potential scattering, the fourth is the resonance scattering while the fifth term contains the interference between resonance scattering and Rutherford scattering. The final two terms contain the corrections, due to finite nuclear size, to the previous interference term.

A FORTRAN subroutine (EXTFN), borrowed from M. L. Gursky of the Los Alamos Scientific Laboratory, was used to calculate Coulomb wave functions, from which hard-sphere phase shifts and penetration factors were computed.

A computer code (GALAHAD) was written in which an approximate linear regression technique, first applied by G. C. Kyker, Jr., to the case of eq. (A.1), was incorporated to give the best fit, in the least squares sense, for the variable parameters E_o, Γ, Γ_p and Δ, the half-width of the resolution function.

In general, given a function

$$y = f(x; a_1, a_2, \ldots a_m) \qquad (A.3)$$

and a set of data pairs (x_1, y_1), $x_2, y_2)$, $\ldots$ (x_N, y_N), we wish to find the set of values of a_k such that $y(x_i)$ is the best fit to y_i in the least squares sense. Since eq. (A.2) cannot be rigorously put into a linear form, we must use approximate methods. We take a first approximation $\{a_k^{(o)}\}$ to the best fit parameters $\{a_k\}$ and take the first term of a Taylor

expansion of eq. (A.3) about $\{a_k^{(o)}\}$:

$$y \equiv f(x;\{a_k\}) \cong f(x;\{a_k^{(o)}\}) + \sum_k (a_k - a_k^{(o)}) \left(\frac{\partial f}{\partial a_k}\right)_{\{a_k^{(o)}\},x}$$

$$y \equiv y_o(x) + \sum_k \alpha_k g_k(x) \qquad (A.4)$$

where

$$y_o(x) \equiv f(x;\{a_k^{(o)}\})$$

$$\alpha_k \equiv (a_k - a_k^{(o)})$$

$$g_k \equiv \left(\frac{\partial f}{\partial a_k}\right)_{\{a_k^{(o)}\},x}$$

Eq. (A.4) is now linear in the α_k and we may apply the usual methods of finding the best fit values of the α_k.

We then set

$$q_i \equiv y_i - y(x_i) = y_i - y_o(x_i) - \sum_k \alpha_k g_k(x_i) \equiv r_i - \sum_k \alpha_k g_k(x_i) \qquad (A.5)$$

and take

$$Q \equiv \sum_i q_i^2 = \sum_i \left[r_i - \sum_k \alpha_k g_k(x_i)\right]^2 \qquad (A.6)$$

Since we want the $\{\alpha_k\}$ such that Q is a minimum, we let

$$\frac{\partial Q}{\partial \alpha_k} = \sum_i 2\left[r_i - \sum_j \alpha_j g_j(x_i)\right]\left[-g_k(x_i)\right] \qquad (A.7)$$

be equal to zero for all k. This gives m equations of the form

$$\sum_i r_i\, g_k(x_i) = \sum_j \alpha_j \sum_i g_j(x_i)\, g_k(x_i) \qquad (A.8)$$

or

$$\sum_j A_{jk}\, a_j = C_k \qquad (A.9)$$

where

$$C_k \equiv \sum_i (y_i - y_o(x_i))\, g_k(x_i)$$

$$A_{jk} = A_{kj} \equiv \sum_i g_j(x_i)\, g_k(x_i)$$

in the m unknowns a_k. The solution to these equations can be obtained on a digital computer using the method of Gaussian elimination.

Since the linear regression problem always has a unique solution, the procedure will rapidly converge to the true best fit if the first approximation $\{a_k^{(o)}\}$ is sufficiently good.

II. Multilevel Analysis

Throughout the data discussed here are found regions where the resonances are not isolated and where, frequently, the shape of the resonance is largely determined by its interference with neighboring resonances. Normally, in the application of R-matrix theory to this problem, approximations are made which result in a diagonal scattering matrix, thereby circumventing the usual difficulties of matrix inversion. This can be achieved by considering a single isolated resonance, as in the preceding section, or by assuming that elastic scattering is the only

participating channel. This latter assumption, quite reasonable in the argon measurements, results in the expression:

$$\left(\frac{d\sigma}{d\Omega}\right)_{pp} = \left[f_{coul}\right]^2 - \frac{\eta}{2k^2\sin^2(\theta/2)} \sum_c (2J_c+1)\sin\beta_c \cos(2\eta \ln\sin\theta/2 + 2\psi_{\ell_c} + \beta_c)$$

$$\times P_{\ell_c}(\cos\theta) + \frac{1}{2k^2}\sum_c \sin^2\beta_c \sum_L \left[Z(\ell_c J_c \ell_c J_c; 1/2L)\right]^2 P_L(\cos\theta) +$$

$$\frac{1}{k^2}\sum_c \sum_{c'<c} \sin\beta_c \qquad (A.10)$$

$$\times \sin\beta_{c'} \cos(2\psi_{\ell_{c'}} + \beta_{c'} - 2\psi_{\ell_c} - \beta_c) \sum_L \left[Z(\ell_c J_c \ell_{c'} J_{c'}; 1/2L)\right]^2 P_L(\cos\theta)$$

The notation here is the same as in eqs. (A.1) and (A.2), except that here c is a spin state index and β_c, the nuclear phase shifts, are summed over all resonances in spin state c. In the above expression, the first term gives Rutherford scattering, the second the interference between resonance and potential scattering, whereas the last two terms represent the resonance scattering. The simplicity of this multilevel expression relative to (A.2) is the result of neglecting the φ_ℓ; that is, ignoring the correction for finite nuclear size.

In the neon data, however, the assumptions that only one particle channel is open and that the φ_ℓ can be neglected are no longer valid. Fortunately, this difficulty coincided with the advent of a large computer installation at Duke University (IBM system 360/75). Accordingly, a

general multilevel, multi-channel R-matrix computer code (MULTI)[38] was written by D. L. Sellin. In this code, up to 20 resonances may be simultaneously treated. In addition, reaction cross sections are included in the calculation. The formulae upon which this calculation is based are well known and are given detailed treatment in refs. 37 and 39. Detailed discussion of this code will be relegated to ref. 38.

LIST OF REFERENCES

LIST OF REFERENCES

1. J. D. Anderson and C. Wong, Phys. Rev. Lett. 7, 250 (1961); 8, 442 (1962). J. D. Anderson, C. Wong and J. W. McClure, Phys. Rev. 126, 2170 (1962); 129, 2718 (1963).

2. P. Richard, C. F. Moore, J. D. Fox and D. Robson, Phys. Rev. Lett. 13, 343 (1964).

3. A. M. Lane and J. M. Soper, Nuclear Physics 37, 663 (1962).

4. P. B. Parks, P. M. Beard, E. G. Bilpuch and H. W. Newson, Rev. Sci. Instr. 35, 549 (1964).

5. N. Bohr, Nature 137, 344 (1936).

6. E. P. Wigner and L. Eisenbud, Phys. Rev. 72, 29 (1947).

7. D. Robson, Phys. Rev. 137, B535 (1965).

8. A. C. L. Barnard and C. C. Kim, Nuclear Physics 28, 428 (1961).

9. J. D. Fox, C. F. Moore and D. Robson, Phys. Rev. Lett. 12, 198 (1961).

10. H. Feshbach, Ann. of Phys. 5, 357 (1958); 19, 287 (1962).

11. R. Lemmer and C. Shakin, Ann. of Phys. 27, 13 (1964).

12. B. Block and H. Feshbach, Ann. of Phys. 23, 47 (1963).

13. H. Feshbach, A. K. Kerman and R. H. Lemmer, Ann. of Phys. 41, 230 (1967).

14. A. Mekjian and W. MacDonald, Phys. Rev. Lett. 18, 706 (1967).

15. W. MacDonald and A. Mekjian, Univ. of Maryland Technical Report 653 (January, 1967).

16. H. A. Weidenmuller, Nuclear Physics 75, 189 (1966).

17. H. A. Weidenmuller and K. Dietrich, Nuclear Physics 83, 332 (1966).

18. C. Mahaux and H. A. Weidenmuller, Nuclear Physics A97, 378 (1967).

19. W. P. Beres and M. Divadeenam, to be published.

20. P. A. Mello, Ann. of Phys. 45, 240 (1967).

21. D. Robson, private communication.

22. P. B. Parks, H. W. Newson and R. M. Williamson, Rev. Sci. Instr. 29, 834 (1958).

23. A. L. Toller, "Neutron Resonances in Sodium, Potassium and Aluminum," unpublished Ph.D. dissertation, Duke University (1954).

24. S. Datz, private communication (1963).

25. G. A. Keyworth, G. C. Kyker, Jr., E. G. Bilpuch and H. W. Newson, Nuclear Physics 89, 590 (1966).

26. E. Kashy, A. M. Hoogenboom and W. W. Buechner, Phys. Rev. 124, 1917 (1961).

27. H. Winkler, R. E. Pixley and R. Bloch, Bull. Am. Phys. Soc. 10, 1204 (1965). R. Bloch, R. E. Pixley, H. Staub, F. Waldner and H. Winkler, Helv. Phys. Acta 37, 722 (1964).

28. T. Young, private communication.

29. D. D. Long, P. Richard, C. F. Moore and J. D. Fox, Phys. Rev. 149, 906 (1966).

30. C. E. Porter and R. G. Thomas, Phys. Rev. 104, 483 (1956).

31. M. H. MacFarlane and J. B. French, Revs. Mod. Phys. 32, 567 (1960).

32. H. F. Lutz, J. J. Wesolowski, L. F. Hansen and S. F. Eccles, Nuclear Physics A95, 591 (1967).

33. D. J. Pullen, A. Sperduto and E. Kashy, Bull. Am. Phys. Soc. 10, 38 (1965).

34. A. J. Howard, J. P. Allen, D. A. Bromley, J. W. Olness and E. K. Warburton, Phys. Rev. 154, 1067 (1967).

35. J. A. Nolen, Jr., J. P. Schiffer, N. Williams and D. von Ehrenstein, Phys. Rev. Lett. 18, 1140 (1967).

36. A. de-Shalit, Phys. Rev. 122, 1530 (1961).

37. J. M. Blatt and L. C. Biedenharn, Revs. Mod. Phys. 24, 258 (1952).

38. D. L. Sellin, private communication.

39. A. M. Lane and R. G. Thomas, Revs. Mod. Phys. 30, 257 (1958).

40. P. M. Beard, "A High Resolution Study of the $^{18}O(p,n)^{18}F$ Reaction," unpublished Ph.D. dissertation, Duke University (1964).

BIOGRAPHY

George Albert Keyworth II

Personal: Born 30 November 1939, Boston, Massachusetts
Married 28 July 1962

Education: B.S. in Physics, Yale University, 1963

Positions: N.S.F. Summer Fellow, Yale University, 1963
Teaching Assistant, Duke University, 1963-1964
Research Assistant, Duke University, 1964-present

Memberships:
American Physical Society
Sigma Xi

Pulbications:

1. Fine Structure of Isobaric Analogue Resonances in ^{41}K (with G. C. Kyker, Jr., E. G. Bilpuch and H. W. Newson) Physics Letters 20, 281 (1966).

2. A High Resolution Study of Isobaric Analogue Resonances in ^{41}K (with G. C. Kyker, Jr., E. G. Bilpuch and H. W. Newson) Nuclear Physics 89, 590 (1966).

3. $^{40}A(d, p)$ Excitation Functions over the Ground-State Isobaric Analog Energy Region (with P. Wilhjelm, G. C. Kyker, Jr., D. L. Sellin, N. R. Roberson and E. G. Bilpuch) Physical Review Letters 18, 130(1967).

4. High Resolution Study of the Isobaric Analogue of the ^{49}Ca Ground State (with P. Wilhjelm, J. C. Browne and E. G. Bilpuch) To be published.

Abstracts:

1. Keyworth, Kyker, Bilpuch and Newson, High Resolution Observation of Elastic Scattering and Reactions of Protons on ^{40}A, Bull. Am. Phys. Soc. 11, 509 (1966).

2. Keyworth, Kyker, Bilpuch, Sellin and Newson, Fine Structure of Isobaric Analogue Resonances in ^{41}K, Bull. Am. Phys. Soc. 11, 82 (1966).

3. Kyker, Keyworth, Sellin, Newson and Bilpuch, $^{40}A + p$ Scattering and Reaction Cross Sections from 2.6 to 3.2 MeV, Bull. Am. Phys. Soc. 12, 585 (1967).

4. Keyworth, Kyker, Newson and Bilpuch, Search for Fine Structure of Analog States in ^{23}Na, Bull. Am. Phys. Soc. 12, 585 (1967).